

Center for Mass Spectrometry and Optical Spectroscopy (CeMOS)
at Mannheim University of Applied Sciences
Institute Director: Prof. Dr. rer. nat. Matthias Rädle

Design and Evaluation of a Multimodal Imaging System for Medical
Tissue Analysis

Inauguraldissertation
zur Erlangung des akademischen Grades
Doctor scientiarum humanarum (Dr. sc. hum.)
der
Medizinischen Fakultät Mannheim
der Ruprecht-Karls-Universität
zu
Heidelberg

vorgelegt von
Annabell Heintz

aus
Speyer
2022

Dekan: Prof. Dr. med. Sergij Goerd
Referent: Prof. Dr. rer. nat. Matthias Rädle

TABLE OF CONTENT

	Page
1 INTRODUCTION	1
1.1 Fundamentals of optical spectroscopy	2
1.2 Imaging techniques for biomedical applications	8
1.3 Aim of the study.....	10
2 MATERIALS AND METHODS	12
2.1 Sample preparation	12
2.2 Light microscope	13
2.3 Data acquisition.....	18
2.4 Image creation and spectra processing.....	19
3 RESULTS.....	23
3.1 Setup and specification of the multimodal imaging system	23
3.1.1 Diameter of pinhole fibre	32
3.1.2 Characteristics of the light sources	55
3.1.3 Determination of the photograph's field of view.....	64
3.1.4 Accuracy of the microscope stage	66
3.1.5 Signal stability of the multimodal imaging system	67
3.1.6 Workflow and setup parameters during scanning experiments.....	69
3.2 Scanning experiments for tissue analysis	74
3.2.1 Distinction between grey and white matter of brain tissue	74
3.2.2 Detection of haemorrhage in a brain section.....	86
3.2.3 Proof-of-concept study: NIR path	89

4 DISCUSSION	94
4.1 Evaluation of the multimodal imaging system, especially the design of the adapted spectroscopic modalities	94
4.2 Information content of the different modalities obtained from tissue analysis	97
4.3 Outlook.....	102
4.4 Conclusion	104
5 SUMMARY	106
6 REFERENCES	107
7 CURRICULUM VITAE AND PUBLICATIONS.....	118
8 ACKNOWLEDGEMENTS.....	121

1 INTRODUCTION^a

To emphasise the importance of light as a fundamental element of daily life and as a key factor for cross-cutting disciplines like medicine, the United Nations (UN) General Assembly announced 2015 as the *International Year of Light and Light-based Technologies*. The *International Day of Light* is annually celebrated on May 16th. On that date in 1960, Theodore Maiman, a physicist and engineer, successfully put a laser (light amplification by stimulated emission of radiation) into operation. In medicine, lasers are used for therapy, surgery, and diagnostics.² One well-established optical technique for medical diagnostics is Raman spectroscopy.³

Raman spectroscopy (see chapter 1.1) is a label-free measuring technique that provides qualitative and quantitative biochemical information at a molecular level. Raman active biomolecules of tissue are lipids and proteins (collagen, elastin) but also deoxyribonucleic acid (DNA), ribonucleic acid (RNA), glucose, lactic acid, carotenoids, and haemoglobin.⁴

A further label-free spectroscopic technique that detects haemoglobin in blood and blood-perfused tissue is visible (VIS) absorption spectroscopy (see chapter 1.1). While haemoglobin is visibly recognisable by its red colour, the spectral characteristics in the VIS region facilitate the separation between oxyhaemoglobin and deoxyhaemoglobin. The signal ratio of both haemoglobin states, chosen as an indicator for the oxygen saturation, was used by Braun⁵ to classify tumorous (Lewis lung carcinoma) tissue, healthy tissue, and the tumour's margins in mice models. Other parameters of endogenous markers in these tissue types, which were identified as different, were water content, fat content, scattering characteristics, and the reduced nicotinamide adenine dinucleotide (NADH) concentration.⁶ Due to the spectral characteristics of these markers, the application of various optical spectroscopic techniques (VIS and near-infrared (NIR) absorption spectroscopy, fluorescence spectroscopy (see chapter 1.1)) was required. This led Braun et al. to design an MRI (magnetic resonance imaging) compatible multispectral Nitinol probe for in-vivo measurements (patent number: DE102014107342A1). In this context, Braun et al.^{7,8} developed

^a Parts of this chapter have been published in ¹.

mathematical algorithms to compensate for the tissue's matrix effects on fluorescence spectroscopy to determine absolute NADH concentrations using the fibre-probe.

This is just one example that demonstrated the detection of tissue changes based on biomolecular information obtained from label-free spectroscopic techniques. Fibre-probe Raman spectroscopy was also successfully applied for tissue diagnostics, such as cancer research.⁹ However, fibre-optic probes acquire a single spectrum at each sample position, while an entire image enables accurate localisation of tissue abnormalities and its margins.

Regarding image-guided surgery and disease diagnosis, hyperspectral imaging of three-dimensional datasets (two spatial dimensions and one spectral dimension), a hybrid modality of spectroscopy and imaging, provides spatially resolved spectral images of the tissue's morphology, physiology, and composition.¹⁰ Although Raman spectroscopy is applicable for diagnostic, prognostics, and as a tool for evaluating new therapies,³ image creation based on the sequential acquisition of Raman spectra is time-consuming because of the exposure time for one spectrum that is in the range of seconds.¹¹

One possibility to reduce the acquisition time is the increase in step or pixel size. However, this causes undersampling of the Raman images, which might result in loss of information. A second possibility is combining Raman imaging with further sensitive and rapid label-free optical techniques.¹¹ The combination of various optical imaging techniques is known as multimodal imaging.¹² In medicine, the significant advantage of multimodal imaging is the improved diagnostic reliability due to the complementary nature of the obtained information.¹²

1.1 Fundamentals of optical spectroscopy

Optical spectroscopy refers to the entirety of qualitative and quantitative analytical methods based on light-matter interactions. Light in terms of optical spectroscopy covers the ultraviolet (UV), the visible (VIS), the near-infrared (NIR), and the mid-infrared (MIR) spectral region. These spectral regions are segments of the electromagnetic spectrum ranging from gamma rays to radio waves. Due to the wave-particle duality, some properties of electromagnetic radiation can be described as a stream of corpuscles (photons), others as a sinusoidal electromagnetic wave.

The length of one sine wave period is known as the wavelength λ (unit: nm or μm). Lambda (λ) is one characteristic parameter of electromagnetic radiation. The second parameter characterising the sinusoidal wave is the frequency ν (unit: s^{-1}). The relationship between ν and λ is the propagation speed of electromagnetic waves, the light velocity c (in vacuum: $c = 2.998 \cdot 10^8 \text{ m/s}$).

$$\nu = \frac{c}{\lambda} \quad (1)$$

A third parameter, commonly used in infrared (IR) spectroscopy, is the wavenumber $\tilde{\nu}$ (unit: cm^{-1}).

Nu tilde ($\tilde{\nu}$) is the reciprocal of λ but also the quotient of ν (frequency) divided by c (light velocity).

$$\tilde{\nu} = \frac{1}{\lambda} = \frac{\nu}{c} \quad (2)$$

The corpuscular theory of light is used to describe electromagnetic radiation based on energy. Each photon has a characteristic energy E that is proportional to ν and the reciprocal value of λ .

$$E = h\nu = h \frac{c}{\lambda} \quad (3)$$

The proportionality constant h is the so-called Planck's constant ($h = 6.626 \cdot 10^{-34} \text{ Js}$). Based on equation 3, the energy of a photon increases the higher the frequency, and vice versa, the higher the wavelength, the lower is the photon's energy.

The energy of a photon plays an important role in the interaction between electromagnetic radiation and matter since only photons of certain energy are emitted or absorbed.

In optical spectroscopy, Schmidt¹³ clusters these interactions in absorption, reflection, scattering, and luminescence spectroscopy. In general, spectroscopy is the separation of electromagnetic radiation according to the energy of a photon. Therefore, a monochromator is used. Additionally, a light source and a detector are required to perform spectroscopic measurements of a sample. To quantify these measurements, the average energy on the detector's area per time interval is recorded. Dividing these values by the size of the detector's area results in an area-independent measuring

value. This measuring value is often referred to as the intensity (unit: counts). The intensity as a function of the wavelength or the wavenumber is known as a spectrum. This introduction of optical spectroscopy focuses on electronic excitation and vibrational spectroscopy because the absorption and emission of light by molecules is the fundament of molecular diagnostic in life science and medicine.¹⁴

An energy level diagram (Jablonski diagram) is used to visualise the various interactions of molecules with light (Figure 1).

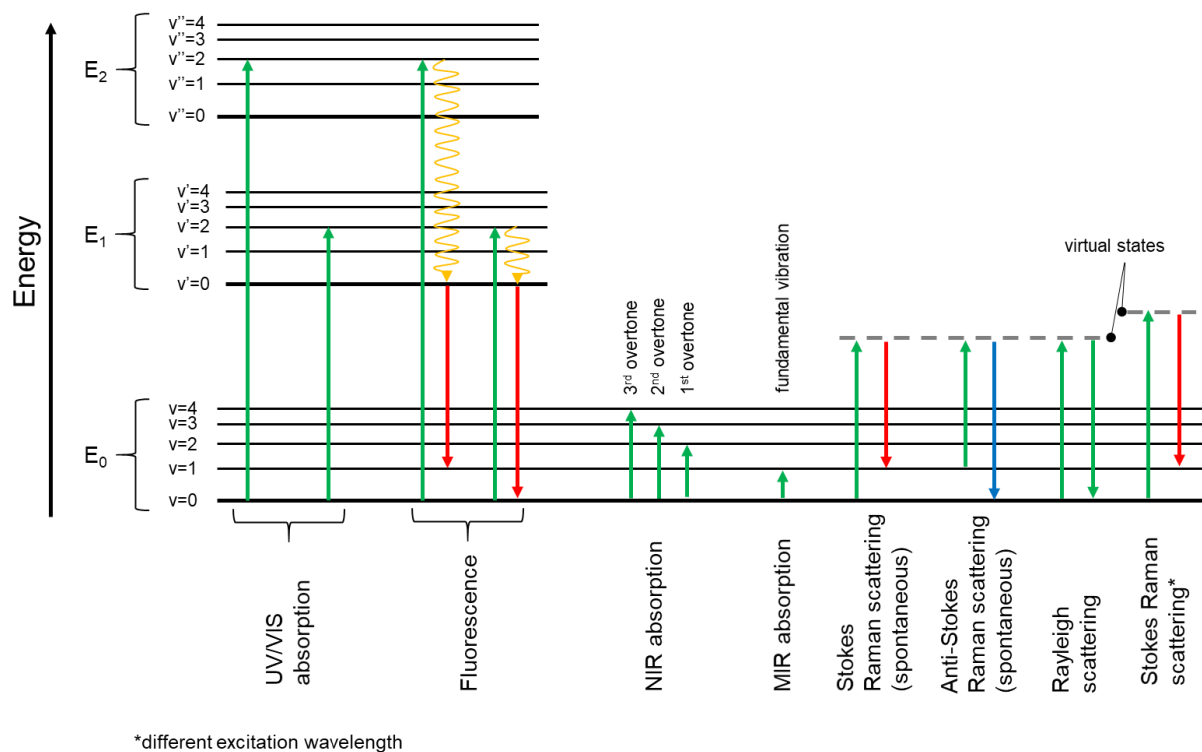


Figure 1 Energy level diagram illustrating various electronic and vibrational transitions in optical spectroscopy; upwards arrow: excitation (absorption), downwards arrow: emission, scattering, orange curved arrow: vibrational relaxation, see text for details (own figure).

For the description of microscopic systems such as molecules, quantum physical effects have to be taken into account. This includes the quantisation of energy in discrete energy levels (Figure 1, black horizontal lines). The smallest units in Figure 1 are the molecule's vibrational states (v , v' , v'') that are fractions of the various electronic states (E_0 , E_1 , E_2). According to the Boltzmann distribution, most molecules are in the electronic ground state and the lowest vibration quantum number (E_0 , $v=0$) at room temperature.

To excite molecules to another energy level (Figure 1, green upwards arrows), the energy of the excitation light (length of arrow) has to be equal to the energy difference

of both energy levels. The energy in the ground state is unequal to zero because of Heisenberg's uncertainty principle.

UV/VIS absorption spectroscopy is one of the first instrumental methods used to study molecular structures in organic chemistry.¹⁵ The light source for the respective range is a deuterium lamp for the UV and a halogen lamp for the VIS spectral region.¹³ Although the light sources differ from each other, the light absorption of both spectroscopic methods causes electronic and vibrational excitations. A molecule's excitation to another electronic state is possible due to the photons' high energy, a result of the low wavelengths in the UV (180-400 nm) and VIS (400-780 nm) region. A prominent absorber of visible light between 415 nm and 580 nm is haemoglobin, present in blood and blood-perfused tissue.¹⁶

Another spectroscopic method based on electronic transitions is fluorescence spectroscopy, a subcategory of luminescence spectroscopy. In fluorescence spectroscopy, the excited molecules usually relax non-radiative (Figure 1, orange curved arrows) within 10^{-12} s into the lowest excited electronic state ($E_1, v'=0$).¹⁷ After that, a photon is emitted (Figure 1, red arrows) to any vibrational state of the ground state (E_0). The energy of the emitted photon, indicated by the length of the arrow, is lower (except for the transition $E_1, v=0 \rightarrow E_0, v=0$) than the energy of the absorbed light. Because of the lower energy, the detected emission band is long-wave (Stokes) shifted compared to the excitation light. The wavelength to excite fluorescence is chosen regarding the fluorophore's (molecule's) individual excitation spectrum, which is proportional to the absorption spectrum of the fluorophore. Light-emitting diodes (LEDs) and laser light sources offer high emission stability. Alternatively, a broadband light source in combination with an appropriate excitation filter (bandpass filter) to narrow the spectral bandwidth of the excitation light is suitable. Commonly used light sources for fluorescence microscopy are mercury arc and Xenon lamps. Compared to a halogen lamp, the emission spectra cover the UV and the VIS spectral range.¹⁸ Endogenous tissue fluorophores with absorption maxima in the UV/VIS spectral region are, amongst others, NADH, collagen, and porphyrins.¹⁹ However, the biological molecule's intrinsic fluorescence is weak and not specific. Due to their limited use, a wide array of fluorescent labels were developed to investigate biochemical processes at molecular levels.²⁰

Other absorption-based spectroscopic techniques are NIR and MIR spectroscopy. In contrast to UV/VIS spectroscopy, the excitation is restricted to vibrations within the

electronic ground state (E_0). The reason is the photons' lower energy, a consequence of the high-wavelength region.

As illustrated in Figure 1, excitations from $v=0$ to $v=2, 3$, or 4 of the ground state are possible for NIR absorption. These transitions are referred to as overtones. Besides vibrational overtones, combination bands of molecular vibrations occur in the NIR spectral region between 780 nm and 2500 nm. These combination bands result from the simultaneous excitation of the same functional group to various vibrational states. A prominent absorber in the NIR spectral region is water with absorption bands around 1450 nm and 1950 nm.²¹ Weaker absorption bands in the NIR range originate from biomolecules like lipids, collagen, and proteins.²² As a light source, a halogen lamp with a tungsten filament is needed.²³

MIR radiation between 2.5 μm and 25 μm was initially induced via a Nernst lamp (ZrO_2) or a globalar (SiC).²⁴ The use of lasers with excitation wavelengths in the MIR spectral region have revolutionised MIR spectroscopy.²⁵ A recently published study performed fast multi-photometric MIR scanning of healthy and tumorous mouse tissue applying a novel MIR scanner based on four lasers.²⁶ Independent of the light source, molecules are excited to fundamental vibrations by light absorption from $E_0, v=0$ to $E_0, v=1$. Different vibrational modes for chemical bonds are possible. The modes are subdivided into stretching (symmetric and asymmetric) and bending (scissoring, rocking, wagging, and twisting), depending on whether the length or the angle of the bond changes.⁴ However, a vibration is only MIR active if the fundamental vibration modulates the molecular dipole moment. Strong MIR absorption bands of biomolecules originate from vibrational modes of proteins (amide I, II, and II), water, and nucleic acids.²⁷

If the vibration modulates the molecular polarisability, the molecule is Raman active. Consequently, MIR (henceforth: infrared (IR)) and Raman spectroscopy are complementary methods. In contrast to IR absorption spectroscopy, Raman spectroscopy is based on inelastic scattering. Currently, more than 25 different types of known Raman techniques, such as coherent anti-Stokes Raman scattering (CARS), surface- (SERS), or tip-enhanced (TERS) Raman scattering, have been established.²⁸ The principle of Raman scattering is subsequently described for the so-called spontaneous Raman effect since the construction and implementation of such a technique is part of this study. The Raman effect was predicted by Adolf Smekal²⁹ in 1923 and experimentally confirmed by Raman and Krishnan³⁰ in 1928.

First, the incident photon excites a molecule to a virtual state (Figure 1, grey dashed lines). Since this state is a quantum mechanical non-stationary state, the molecule immediately relaxes back to the ground state while emitting a photon, the so-called Raman scattered photon. If the energy of the scattered photon is lower than the energy of the excitation photon, one vibrational quantum of energy is left in the molecule. This phenomenon is referred to as Stokes Raman scattering. Anti-Stokes Raman scattering exists if the Raman scattered photon's energy is higher than the energy of the excitation photon. In this case, a vibrational quantum of energy is taken from the molecule. For this purpose, the molecule has to be located in the first vibrational quantum of the ground state ($E_0, v=1$) before interacting with the incident photon. Due to the Boltzmann distribution, the probability that a molecule is already excited at room temperature is in the order of 0.1%.¹³

In general, the Raman effect is a weak measuring effect with an occurrence probability of approximately 1 in 10^8 incident photons.³¹ Much more likely is the elastic (Rayleigh) scattering where the light frequency stays constant. Consequently, intensive monochromatic light sources like lasers are required of Raman spectroscopy. The laser's wavelength and power are key factors in Raman spectroscopy because Raman intensity is linear to the laser power and proportional to the fourth power of the laser's frequency. On the one hand, this results in higher Raman signals the shorter the laser wavelengths. On the other hand, short excitation wavelengths cause a fluorescence background signal that interferes with the Raman spectrum. The fluorescence signal can be six orders of magnitude higher than the Raman signal.³² To minimise fluorescence signal, an excitation wavelength in the red (620-780 nm) or NIR spectral region is recommended for Raman spectroscopy of fluorescent biological samples.³³ Although the energy of the Raman scattered photon changes with the energy of the excitation light (laser wavelength) (see Figure 1), the difference in energy (Raman shift) between the incident photon (Figure 1, green arrow) and scattered photon (Figure 1, red arrow) remains constant for a certain Raman-active vibrational mode in the molecule. Because of this, Raman spectra are plotted as the scattered intensity versus the Raman shift (energy difference).

The Raman shift (unit: cm^{-1}) of a certain Raman peak is identical to the wavenumber of the IR absorbance spectrum since Raman and IR bands reflect the structure-dependent frequency associated with a molecule's fundamental vibration.

The majority of Raman peaks present in tissue samples are located between 700 cm^{-1} and 1800 cm^{-1} .⁴ This spectral range is referred to as the fingerprint region.³⁴ Raman peaks of biomolecules arise predominantly from CH, CC, and CO vibrations of lipids and proteins.²⁷ CH-stretching vibrations are also detected in the high-wavenumber region from 2800 cm^{-1} to 3050 cm^{-1} .³⁵ The region between 1800 cm^{-1} and 2800 cm^{-1} is known as the silent region since biological molecules do not produce any Raman signal in this range.³⁶

Despite this silent region, more tissue characteristics (bands) are observed in vibrational spectra in contrast to other optical spectra.³⁷ Compared to IR spectroscopy, the Raman scattering signal of the water molecule is very weak.³⁸ Consequently, water in biological samples interferes slightly with Raman spectra. Therefore, sample preparation, such as drying for IR spectroscopy, is not mandatory to detect biomolecules.

1.2 Imaging techniques for biomedical applications

The gold standard for tissue diagnostics is histology,³⁹ which is known as histopathology in connection with disease.³⁷ The most important technique for clinical and pathological diagnostics is bright-field microscopy in the transmitted light mode.⁴⁰ Thereby, morphological information is obtained from processed, stained tissue slides.³⁹ The largely used dye is haematoxylin and eosin (H&E),³⁹ where haematoxylin stains basophilic components of cell structure like RNA and DNA blue. In contrast, acidophilic components such as cell cytoplasm, stromal material, and fibre structures appear deep pink due to the eosin staining.^{40,41}

Further morphological imaging techniques for biomedical applications are optical coherence (OC) tomography, photoacoustic (PA) imaging, laser scanning (LS) microscopy, second-harmonic generation (SHG) microscopy, and two-photon excited fluorescence (TPEF) microscopy.¹²

Besides morphological imaging techniques, Vogler et al.¹² differentiate functional imaging techniques that visualise functional parameters like the local chemical composition. One of these imaging techniques is Raman-based microscopy, a combination of Raman spectroscopy and microscopy. The Raman microscope was first proposed by Delhaye and Dhamelincourt in 1975.⁴² Since the 1990s, companies

have been commercially selling the combination of a Raman spectrometer and an optical microscope.³²

The advantage of these setups is the microscope's objective with a high numerical aperture (NA). With the aid of the objective, the excitation (laser) light is focused on a small spot with a few micrometres in diameter. This enables a high collection efficiency of the Raman signal from a microscopic area.³²

A further approach is the confocal detection principle that reduces the detection volume in order to increase the spatial resolution and suppress stray light with the aid of a circular pinhole in front of the detector.⁴³ The pinhole is located in the image plane of the microscope so that it is confocal with the illumination spot.⁴³ In practice, a glass fibre instead of a pinhole can be alternatively used where the fibre entrance acts as the confocal opening.⁴⁴ This fibre is subsequently connected to the spectrometer's entrance slit. To illuminate the slit entirely, it is beneficial to couple the pinhole fibre to a fibre with a bigger diameter.

Raman-based microscopy for research and diagnostic purposes of tissue was demonstrated multitudinously. Ex-vivo examinations of pathological changes comprise different tissue types such as breast,⁴⁵ brain,^{46–48} colon,⁴⁹ skin,^{50–52} and spinal cord.^{53,54} The preparation of an (H&E) stain of the previously chemically analysed sample or a serial section is an essential step in the workflow since it is useful to accompany the chemical composition of a sample with morphological information.⁵⁵

Comparing Raman images with images of stained (usually H&E) tissue sections is preferred to develop and validate Raman-based classification models.¹¹

On the one hand, the video capability for taking bright-field photographs is an established method to visualise and analyse the sample's morphology. On the other hand, video images in real-time facilitate the lateral orientation on the measurement sample and confirm whether the sample is placed in the focus.

Depending on the optical microscope, Raman microscopes can be expanded by conventional microscopic modalities. While bright-field microscopy records a sample's contrast based on the attenuation of the illumination light, dark-field microscopy highlights structures based on the light that is scattered by the sample.⁵⁶ Polarisation microscopy enables the localisation and analysis of birefringent biological structures such as microtubules, thin filaments, and myofibrils.⁵⁷

For biomedical applications, Raman spectroscopy was combined with several optical and non-optical methods.⁵⁸

One commonly used multimodal imaging approach is the combination of Raman and IR spectroscopy. Kochan et al.⁵⁹ studied alterations in murine brain tissue based on data obtained from Raman and IR imaging. IR and/or Raman spectroscopy was used by Gajjar et al.⁶⁰ for diagnostic segregation of brain tumours. Reviews of tissue classification based on vibrational (IR and Raman) spectroscopy were provided, among others, by Lin et al.,³⁸ Diem et al.,³⁴ and Bunaciu et al.⁶¹

Lasch and Noda⁶² analysed hamster brain tissue by complementing Raman and IR spectroscopy with MALDI-TOF mass spectrometry. An overview of multimodal imaging, based on vibrational spectroscopies and mass spectrometry, for tissue studies was recently given by Tuck et al.⁵⁵ Combinations of Raman images with images obtained from the above-mentioned morphological imaging techniques were also developed. Modular devices that combine OC tomography and Raman spectroscopy for tissue characterisation were developed by the research groups of Mahadevan-Jansen⁶³ and Popp.⁶⁴ Bocklitz et al.⁶⁵ presents a multimodal microscope that combines CARS, TPEF, and SHG for rapid characterisation of a tissue section's architecture and biochemical composition. Based on these results, a pseudo-H&E-stained image was computationally calculated. With the aid of this image, a region of interest (ROI) was designated for subsequent analysis of the molecular selective Raman spectroscopy.

1.3 Aim of the study

Multimodal imaging is widely used for biomedical applications. This study aims to develop a novel multimodal imaging system that combines three modalities (bright-field, dark-field, polarised light) of a light microscope with VIS and NIR reflectance spectroscopy as well as Raman spectroscopy to analyse unstained tissue sections. The imaging system should also be able to record images of stained tissue sections for reference. This requirement might be challenging because bright-field images of stained tissue sections are recorded in the transmitted light mode,⁴⁰ whereas Raman spectra are typically collected in the reflection mode.⁶⁶

The focus of the design is on the lateral resolution of the spectroscopic modalities. One significant parameter that influences the optical resolution is the diameter of the detection fibre (pinhole). Especially for Raman spectroscopy, using a small fibre diameter is desirable for additional suppression of the interfering fluorescence signal and stray light from levels other than the setup's focal plane. However, a small fibre diameter results in a lower detected Raman signal of the weak Raman effect.

Consequently, to achieve a sufficient signal-to-noise ratio (SNR), the integration time has to be increased. This accompanies a longer measurement time and a prolonged laser exposure which may alter or destroy the tissue section.

As part of this study, the detection fibre's impact on the Raman signal is carefully considered for the design of the multimodal imaging system. Further investigations to specify the developed multimodal imaging system are the spectral characteristics of the light sources, the microscope stage's accuracy, the various signal stabilities, and the elaboration of a workflow to perform imaging of biological samples.

The first application of the developed multimodal imaging system on biological tissue is realised to differentiate between grey matter (GM) and white matter (WM) of normal (under healthy conditions) brain tissue. GM and WM are the two main areas of the brain that are recognisably differentiable. GM is composed of protein-rich neuronal somas, whereas WM does not contain neuronal bodies. The characteristic of the lipid-rich WM is the high presence of myelinated axons.⁶⁷ This difference in lipid and protein content was used by a series of researchers^{46–48,59,68,69} to distinguish between GM and WM based on peak ratios or the sum of two peak ratios of Raman intensities. These various lipid-to-protein ratios are also used in this study to evaluate the recorded Raman spectra. The proof-of-concept is performed within two sets of measurements, a global and a local scanning experiment. While the global scan collects data from the brain section at a poor lateral resolution of the spectroscopic modalities, the local scan is performed at a designated ROI with a smaller step size for spectra collection.

After data acquisition, images based on the scanned areas' spectral information are created and the taken photographs are stitched to an entire image. The single images obtained from the microscopic and spectroscopic modalities are evaluated regarding the certain modalities' benefit to distinguish between GM and WM. A stack of the images obtained from the various modalities is not part of the study.

Besides the differentiation between GM and WM, Raman and VIS reflectance spectroscopy are applied to detect haemorrhage in brain tissue.

Finally, an investigation of NIR reflectance spectroscopy proves the feasibility of detecting water and fat in NIR absorption spectra obtained with the designed NIR path.

2 MATERIALS AND METHODS^b

2.1 Sample preparation

This study investigates two tissue types: mouse brain tissue and Serrano ham. While Serrano ham (Españísimo Jamón Serrano-Schinken, Aldi-Süd, Germany; thickness: 1 mm) is only used to further characterise the adapted near-infrared (NIR) reflectance path (chapter 3.2.3), the mouse brain tissue is the actual measurement object to perform the first application of the developed multimodal imaging system.

Therefore, one female C57BL/6J mouse (Janvier Labs, Le Genest-Saint-Isle, France) was kept at the animal facility Mannheim under specific pathogen-free conditions on a 12-hour light/dark cycle. Food and water were available ad libitum. The animal experimental protocol was approved by the Regierungspräsidium Karlsruhe according to EU directive 2010/63.

Before brain excision, the mouse was perfused with 1X phosphate-buffered saline (PBS) for 20 min. To avoid disintegration, the brain was immediately embedded in optimal cutting temperature (OCT) compound (OCT Mounting media, VWR, Randor, PA, USA) and stored at -80 °C. Later, tissue cross-sections of the frozen and embedded brain tissue were prepared in the coronal plane. For this purpose, a cryostat (CM3050 S, Leica Biosystems Nussloch GmbH, Nussloch, Germany) at an operating temperature of -20 °C was used. The thickness of a tissue section is 16 µm, which is appropriate to perform Raman measurements. Previously published studies recorded Raman spectra of brain tissue sections with thicknesses between 10 and 25 µm.^{70–73} All of these tissue sections were placed on a calcium fluoride (CaF₂) microscope slide because the fluorescence signal of standard glass microscope slides superimposes the Raman signal.⁷⁴ Besides CaF₂ slides, aluminium foil, quartz slides, and gold-coated slides as potential substrates with low fluorescence background were successfully investigated for Raman spectroscopy.^{75,76}

For the proof-of-concept study to distinguish between grey matter (GM) and white matter (WM), one 16 µm cryosection is placed on a gold-coated slide (BioGold®, E63479-AS, Science Services GmbH, Munich, Germany) and stored at -20 °C until further analysis. In addition to the analysis of this unstained tissue section in the

^b Parts of this chapter have been published in ¹.

incident light modes, data acquisition with the developed multimodal imaging system is completed by bright-field images of a haematoxylin and eosin (H&E)-stained 16 μm cryosection in the transmitted light mode. For direct comparison, a consecutive section is used. In contrast to the unstained tissue section, the stained tissue section is mounted on a glass slide (SuperFrost[®] slide, VWR, Radnor, PA, USA) and covered with Eukitt[®] mounting medium (Buddeberg GmbH, Mannheim, Germany) as well as a coverslip. A second unstained 16 μm section on a gold-coated slide with bloodstain is used to verify the detection of haemorrhage.

2.2 Light microscope

The core piece of the multimodal imaging system is the light microscope Leica DM R (Leica Microsystems GmbH, Wetzlar, Germany; formerly known as Leitz). This model series is a modular construction system that enables various configurations. Photographs of the initial configuration are shown in Figure 2. The specification of the numbered parts is listed in Table 1.

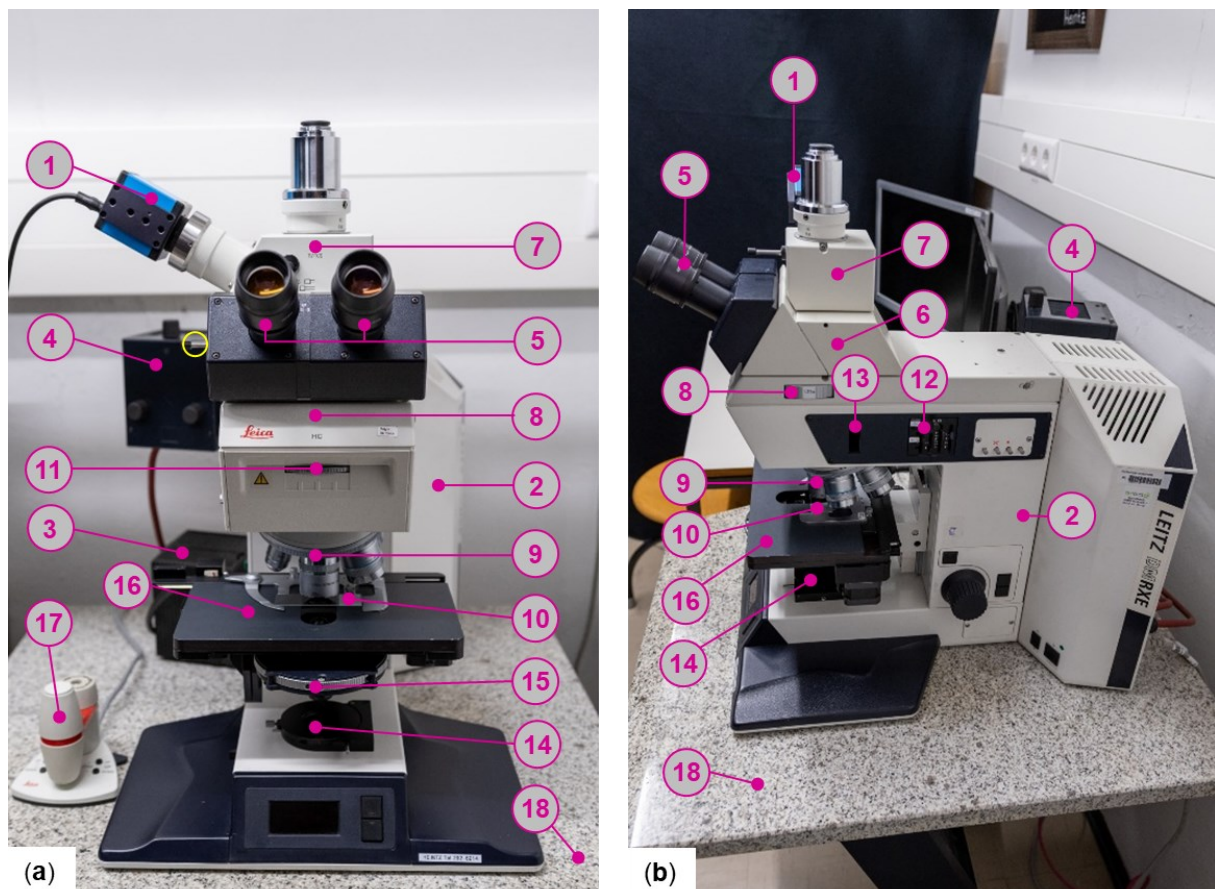


Figure 2 Light microscope Leica DM R (initial configuration): (a) front view, (b) side view. See Table 1 for the description of the used numbers.

Table 1 Description of the numbering depicted in Figure 2.

No.	Specification
1	Colour camera, DFK 41AF02, 1280 x 960 pixels (1.2 MP), 8-bit (dynamic range), CCD sensor, IR cut filter; [The Imaging Source Europe GmbH, Bremen, Germany]
2	Microscope stand LEITZ DM RXE; [Leica Microsystems GmbH, Wetzlar, Germany]
3	Lamp housing 107/2; [Leica Microsystems GmbH, Wetzlar, Germany] Halogen lamp, HLX GY6.35, 12 V, 100 W; [Osram Licht AG, Munich, Germany]
4	Lamp housing 106; [Leica Microsystems GmbH, Wetzlar, Germany] Halogen lamp, HLX GY6.35, 12 V, 100 W; [Osram Licht AG, Munich, Germany]
5	Eyepieces, HC PLAN 10x/25M; [Leica Microsystems GmbH, Wetzlar, Germany]
6	Microscope tube, HC FSA 25 P; [Leica Microsystems GmbH, Wetzlar, Germany]
7	Interchangeable photo adapter tube; [Leica Microsystems GmbH, Wetzlar, Germany]
8	Tube optics, HC: 1.25x, 1.6x, Scan, Bertrand lens; [Leica Microsystems GmbH, Wetzlar, Germany]
9	Sextuple nosepiece (BD, M32), HC; Microscope objectives: 5x, NA: 0.12, N PLAN; 10x, NA: 0.25, N PLAN; BD20x, NA: 0.50, HC PL FLUORTAR; 40x, NA: 0.65, N PLAN; BD50x, NA: 0.85, PL APO; BD100x, NA: 0.90, PL APO; [Leica Microsystems GmbH, Wetzlar, Germany]
10	Gold-coated slide: BioGold®, E63479-AS; [Science Services GmbH, Munich, Germany] Glass slide: SuperFrost® slide; [VWR, Radnor, PA, USA]
11	Incident light turret: BF reflector, DF reflector, Smith reflector, adjustment reflector; [Leica Microsystems GmbH, Wetzlar, Germany]
12	Diaphragm module HC RF; [Leica Microsystems GmbH, Wetzlar, Germany]
13	Polariser R/P (switchable vibration direction); [Leica Microsystems GmbH, Wetzlar, Germany]
14	Polariser ICT/P (vibration direction: North-South); [Leica Microsystems GmbH, Wetzlar, Germany]
15	Condenser disc: 8-position disc (no light ring inserted); universal condenser UC, condenser top: 0.90 S1; [Leica Microsystems GmbH, Wetzlar, Germany]
16	Motorized microscope stage, EK 14 mot, travel range 3" x 2"; [Märzhäuser Wetzlar GmbH & Co. KG]
17	Control element Leica SmartMove; [Leica Microsystems GmbH, Wetzlar, Germany]
18	Passive anti-vibration table with rubber buffer and granite slab; [Leica Microsystems GmbH, Wetzlar, Germany]

Except for the colour camera with a charge-coupled device (CCD) sensor (1), the microscope, including various components, was assembled and purchased second-hand from Optik-Online-Woitzik (Thomas Woitzik, Bad Dürkheim, Germany).

The remarkable feature of the microscope is the equipment with two light modes (transmitted and incident) for the observation of transparent and opaque samples. The light source (halogen lamp) of the respective light path is installed in a lamp housing

at the back of the microscope stand (2). Each light source has an adjustable voltage value between 5 V and 12 V. While the arrangement of the optical components and the halogen lamp in the lower lamp housing (3) is fixed, the halogen lamp is adjustable in x and y direction and a two-lens collector is focusable in the upper lamp housing (4). Independent from the light path, the microscopic photographs are recorded with the colour camera (1) and visually observed via the eyepieces (5). The pair of eyepieces is directly attached to the microscope tube (6). Three different observation modes (100% photo, 100% visual, or 50% / 50%) are selectable by moving the switch rod for the beam splitter (Figure 2a, yellow circle) inside the microscope tube.

A switchable tilted mirror with two click-stop positions (either 100% to the side or 100% to the top (no optics)) is included in the interchangeable photo adapter tube (7). Two additional adapter tubes without optics are mounted on the vertical exit port. This exit will be used at a later stage to expand the light microscope by Raman spectroscopy. Photographs obtained from all microscopic modes are recorded with the colour camera (1) installed at the c-mount adapter sidewise of the photo adapter tube (7). The specification of the lens inside the c-mount adapter tube is unknown.

A further lens for the projection of the intermediate image into the eyepiece and the camera is mandatory because the microscope has an infinite tube length. This lens (also known as tube optics) is inserted in the cover plate (8) of the microscope stand. The present cover plate comprises a turret with various lenses, including lenses with magnifications of 1.25x and 1.6x.

The total magnification of the microscope is the result of multiplying the several magnifications of the optical components in the light path. The lens or the lens system facing the object is called objective. Objectives with different magnifications and numerical apertures (NAs) are mounted on the objective nosepiece (9). The specifications of the available objectives are listed in Table 1. All objectives are dry objectives, designed for use without an immersion medium like water, glycerine or oil. Moreover, except for the 40x objective, the objectives do not require a cover glass on the sample to perform measurements. The bright- and dark-field (BD) objectives have an external diameter with an M32 thread. The high diameter is caused by a built-in annular mirror or annular lenses for the incident light dark-field (DF) mode. However, the BD objectives can also be used in the bright-field (BF) mode. Since the remaining BF objectives have an M25 thread, objective spacer rings (32/25 adapters) are utilized to connect these objectives to the nosepiece.

The nosepiece with the objectives is arranged above the object that is mounted on a microscope slide (10). Such a microscope design, where the object is observed from above, is called an upright microscope. For the observation of transparent objects, the transmitted light mode with illumination from below is recommended.⁵⁶ Nevertheless, this illumination mode is not suitable for optically opaque objects or objects on an opaque substrate such as the gold-coated slide. Therefore, the incident light mode is required. A schematic drawing of the light paths will be shown at a later stage (chapter 3.1, Figure 3c).

While the backscattered light is detected orthogonally to the microscope stage, the propagation direction of the excitation light is lateral along with the light axis of the microscope. For incident light microscopy, a reflector in the incident light path is mandatory to guide the excitation light at a 90° angle downwards onto the object. This reflector is a beam splitter that allows the backscattered light to pass. The incident light reflector is located in a 4-position turret (11) inside the microscope. The proper reflector is selected according to the contrast technique. In total, three different contrasting techniques for incident light mode are available: bright-field, dark-field, and polarisation microscopy.

For bright-field microscopy, the BF reflector is chosen. Additionally, the diaphragm module (12) in the excitation light path is fully pushed in. Thereby, illumination channel I is activated, which includes a switchable neutral density filter, a variable aperture, and a variable field diaphragm. Illumination channel II is activated by pulling out as far as the first stop. This channel has a fixed aperture and field diaphragm. It does not contain a neutral density filter because illumination channel II is used for incident light dark-field, which requires high light intensity. Besides the aforementioned specially designed BD objectives, a DF reflector with a ring mirror is used to generate a circular illumination. The illumination path for polarisation microscopy is similar to bright-field microscopy. This is why BF objectives and channel I of the diaphragm module are used. Furthermore, a polariser (13) in the excitation path and an analyser (analyser IC/P with whole-wave compensator, vibration direction: East-West, Leica Microsystems GmbH, Wetzlar, Germany; not illustrated) in the detection path are mandatory. The polariser and the analyser are orientated in a crossed direction so that their polarisation directions are shifted by 90° (North-South versus East-West).

By inserting the analyser the other way up, a whole-wave compensator (WWC) is activated to increase the colour contrast for polarisation microscopy. Moreover, a

Smith reflector with two reflecting surfaces and lenses is utilised since this reflector is better from a polarisation optic point of view. The fourth reflector is a centring aid. It is used for the visual lamp centration in the incident light path via an adjustment window on the left side of the microscope stand (not illustrated). Further components that are set in the incident light path are the aperture and field diaphragm in the diaphragm module (12).

An adjustable aperture and field diaphragm (not illustrated) are also present in the bottom part of the microscope. This is the microscope part where the excitation light for transmitted light microscopy propagates laterally along before being reflected at a tilted mirror (not illustrated). After transmitting the retractable polariser (14), the excitation light passes the condenser connected with the condenser disc (15). Since this disc does not contain light rings or prisms, bright-field microscopy is the only contrast technique performed in the transmitted light mode. Limitations regarding the microscope objective are due to the condenser top that can be used for objectives with apertures up to 0.75. For objective magnifications of 10x or below, the condenser top can be swung out for bright-field observations. At the same time, two auxiliary lenses (coupled to the universal condenser) are swung in. Thereby, Köhler illumination is still guaranteed for magnifications of 1.6x and higher. Köhler illumination is a method used for incident and transmitted light microscopy. It is characterised by a homogenous illumination in the object plane.⁷⁷

The object is placed on a motorised microscope stage (16), equipped with a sample holder for standardised microscope slides. The microscope stage is manually moved along the lateral axes (x- and y-axis) with the aid of the control element (17). The control element and the microscope stage are connected to the electronic box (Leica CTR 6000 box, Leica Microsystems GmbH, Wetzlar, Germany; not illustrated). The USB port at the electronic box is used for communication with the personal computer during subsequent scanning experiments. In advance, the hardware (control unit and stage) is configured (precise stage step mode, stage speed adjustment: 5 mm/s, stage acceleration adjustment: 0.3 mm/s²) via the Leica SDK Hardware Configurator (version 16.1, Leica Microsystems CMS GmbH, Mannheim, Germany).

Vibrations during the measurements are reduced using a passive anti-vibration table with rubber buffer and a massive granite slab (18).

2.3 Data acquisition

For data acquisition during scanning experiments, an in-house developed computer application based on LabVIEW™ (National Instruments™) is used. Using the computer application, the microscope stage, the camera, and the spectrometers are triggered. The scanning methodology is called point mapping. Thereby, either photographs or spectra are recorded at each measurement point, while the microscope stage is scanned along the lateral axes. Scanning parameters such as the step size and the travel range of the stage, and the integration times of the camera and the spectrometers are set in the programme.

Raman spectra are acquired with the spectrometer unit included in the MultiSpec® Raman System (tec5 AG, Steinbach, Germany). The spectrometer is equipped with a thermoelectric (TE) CCD detector. Raman shifts are recorded in a spectral range between 300 cm⁻¹ and 3200 cm⁻¹ with a spectral resolution of 7 cm⁻¹. Moreover, the Raman system comprises an integrated temperature-stabilised 785 nm gallium aluminium arsenide (GaAlAs) diode laser. The laser power is adjustable between 50 mW and 500 mW. Experiments at single measurement points for the characterisation of the Raman path, where scanning is not required, are performed with the manufacturer's (tec5 AG) process software MultiSpec® Pro II (version 1.4).

Another process software used in this study is ASPECT Plus (version 2.7) from Carl Zeiss Spectroscopy GmbH (Jena, Germany). Similar to the MultiSpec® Pro II software, ASPECT Plus is applied for experiments at single measurement points. However, instead of Raman spectra, elastically scattered light in the VIS and NIR spectral region is recorded. For the detection of VIS spectra between 310 nm and 950 nm, the VIS spectrometer MCS 621 VIS II (Carl Zeiss Spectroscopy GmbH, Jena, Germany) with a photodiode array (PDA) detector is utilised. The spectral resolution of the VIS spectrometer is 10 nm.

The third commercially available spectrometer is the visible (VIS) and NIR spectrometer MCS 611 NIR 2.2 (Carl Zeiss Spectroscopy GmbH, Jena, Germany) with a spectral range from 950 nm to 2150 nm and a spectral resolution of 10 nm. Therefore, the NIR spectrometer is equipped with an extended wavelength indium gallium arsenide (InGaAs) PDA detector designed for wavelengths up to 2200 nm.

Silicon, the semiconductor material of the sensor in the VIS and Raman spectrometer, detects photons of wavelengths below 1100 nm.⁷⁸ The material-specific maximum detectable wavelength (cut-off wavelength) depends on the energetic band gap

between the valence and conduction band of a semiconductor.⁷⁹ This is an important factor when selecting a suitable detector for a desired spectral range.⁷⁹

Due to time constraints for the scanning experiments, all spectra recorded in this study are based on single measurements ($n = 1$, no accumulation), irrespective of the modality.

2.4 Image creation and spectra processing

The Grid/Collection stitching⁸⁰, a Fiji plug-in, is used to stitch the single photographs taken by the camera. Thereby, the photographs of each microscopic modality are separately stitched to an entire image. During stitching, the tile overlap of adjacent photographs is set to 20%. Hence, photographs are also taken with an overlap of 20%. The corresponding step size of the microscope stage depends on the magnification of the microscope objective. It is calculated based on the photograph's field of view. These dimensions are subsequently (see chapter 3.1.3) determined with the aid of a calibration slide (LIM Calibration Slide, Laboratory Imaging Ltd.) as well as the open-source imaging processing package Fiji. Additional processing such as brightness adjustment or contrast enhancement is not performed on the stitched images of the unstained tissue section. However, a white balance using the open-source raster graphics editor GIMP is applied to the stitched image of the H&E-stained section obtained in the transmitted light mode.

Spectra of the respective spectroscopic modalities are evaluated with an in-house developed Python3 (Python Software Foundation) application. Three-dimensional (x, y, z) hyperspectral data cubes are assembled, where x and y are the image coordinates (pixel) and z is the corresponding intensity spectrum I_{sample} .

Each intensity spectrum (I_{sample} also I_{net}), irrespective of the spectroscopic modality, is automatically calculated by the developed LabVIEWTM programme by subtracting a dark spectrum (I_{dark}) from the initially recorded raw spectrum (I_{raw} also I_{gross}), according to equation 4.

$$I_{sample} = I_{raw} - I_{dark} \quad (4)$$

The dark spectrum is a single spectrum, once recorded before each scanning cycle. Since the dark spectrum is a function of temperature and exposure time,⁸¹ parameters are similar to those of the initial scanning cycle. However, the light source (laser or

halogen lamp) is turned off (dark). The purpose of the dark spectrum's subtraction is to eliminate a background signal caused by the detector.

An additional undesirable spectral feature of VIS/NIR reflectance spectroscopy is the spectral characteristic of the halogen lamp, which has to be compensated. The measuring principle of the VIS/NIR spectroscopic path is known as transflection, a hybrid type of transmission and reflection.

For the present case, the light of the upper halogen lamp passes through the tissue section and causes specular reflection at the gold coating of the microscope slide. Afterwards, the 180° back-reflected light penetrates a second time through the cryosection. The diffusely scattered light from the cryosection that is not detected due to the 180° arrangement is neglected. Moreover, the beam guidance is assumed to be comparable to a transmission setup where the transmission of a plane-parallel layer by a parallel light bundle is measured.

For this reason, the sample's spectral reflectivity (R) in the VIS and NIR spectral region is calculated for each pixel based on equation 5.⁸²

$$R = \frac{I}{I_0} \quad (5)$$

Thereby, I is the wavelength-dependent intensity reflected from the sample. I_0 is the halogen lamp's wavelength-dependent intensity reflected from a Zenith Polymer® Diffuse Reflectance Standard (SG 3052, reflectivity $\approx 99\%$, SphereOptics GmbH, Herrsching, Germany) multiplied by an arbitrary factor of 2.5. This factorisation is mandatory to raise the intensity level of the diffuse reflection at the Zenith Polymer® above the intensity level of the sample measurements. Since the gold-coated microscope slide, the substrate of the cryosection, causes specular reflection, the intensity level after reflection at the sample is constantly higher than the intensity level of the reference spectrum for identical test parameters (integration time, halogen lamp's voltage setting). Consequently, the calculated reflectivity would be higher than 1 (1 = 100%) without the factorisation.

The corresponding absorbance (A) is calculated according to Lambert-Beer's law (equation 6):

$$A = \log \frac{I_0}{I} = \varepsilon c d \quad (6)$$

where ε : molar absorption coefficient (unit: L mol⁻¹ cm⁻¹)
 c : concentration (unit: mol L⁻¹)
 d : optical path length (unit: cm)

Since the light transmits the cryosection two times, the optical path length is twice as much as the tissue section's physical thickness.

Images based on the reflectivity or absorbance at a particular wavelength in the VIS or NIR spectral region are created by colourising the pixels (lateral coordinates) according to their respective values. For visualisation, PyQtGraph (Scientific Graphics and GUI Library for Python) is used. The pixel with the highest value is yellow, while the lowest value is indicated by a light blue pixel. The chosen linear colour scale is referred to as bipolar. The identical colour scale is applied to create images based on the Raman spectra.

While data analysis of the VIS/NIR spectra is based on a single wavelength, intensity peak ratios or the sum of peak ratios of several Raman peaks are evaluated to distinguish between GM and WM.

To get the favoured Raman peaks, spectral pre-processing of Raman spectra is essential before the image generation. The reasons are contaminations in the Raman spectra such as cosmic rays, noise and background signals.⁸³ These background signals can either originate from the substrate or the autofluorescence of biological samples.⁴⁵ Several researchers lowered the fluorescence background experimentally before Raman measurements by photobleaching the biological autofluorescence with the aid of the laser.^{70,84–86}

Diverse algorithms for a mathematical removal of background signals, cosmic rays, and noise by the pre-processing of the recorded Raman spectra were investigated by numerous researchers.^{81,83,87}

The data pre-processing of Raman spectra recorded in this study is as follows. To prevent errors in the further processing steps, software-based zero values in the Raman spectra are firstly deleted. The zero values originate from a correction file multiplied by the Raman spectra. This factorisation of each pixel is recommended by the manufacturer (tec5 AG) to compensate for the variable sensor sensitivity of the silicon detector that decreases towards higher Raman shifts (higher wavelengths).

Thereby, the potential detection of the excitation radiation is eliminated by multiplying the first 75 pixels with zero. The last four pixels are set to zero because of the sensor design (information: tec5 AG). Furthermore, the first five and last five pixels with intensity values >0 are deleted due to their high gradients in the Raman spectrum that cause potential problems in the pre-processing. Consequently, the number of active sensor pixels (x-values) is reduced from 1044 to 955. This corresponds to a spectral range from 350 cm^{-1} to 3195 cm^{-1} . In the following step, an algorithm for spectra despiking (threshold value: 65) is applied.⁸⁸ The purpose of this step is the removal of cosmic rays. Cosmic rays appear when a CCD detector is struck by errant high-energy photon⁸⁸ and are characterised as sharp positive peaks at random positions in the Raman spectrum.⁸⁹ By subtracting each Raman spectrum's lowest intensity value, the individual offset of the Raman spectra is removed. Afterwards, an asymmetric least squares (AsLS) algorithm compensates for broad biological fluorescence background.⁹⁰ Parameters like the lambda value and p-value are set to 10^6 and 0.1, respectively. The last step of spectral pre-processing is noise reduction by smoothing. Therefore, a Savitzky–Golay filter⁹¹ is applied. The convolution coefficients are set to a polynomial degree of 3 and a window size of 11. To perform the entire data pre-processing, the developed Python3 application is used.

3 RESULTS[°]

3.1 Setup and specification of the multimodal imaging system

Photographs and a schematic drawing of the developed multimodal imaging system are shown in Figure 3. Similar to Figure 2, a table (Table 2) containing specifications of the numbered parts in the figure is placed below. Since most of the components were already described in chapter 2.2, this chapter primarily addresses the modifications compared to the initial setup.

[°] Parts of this chapter have been published in ¹.

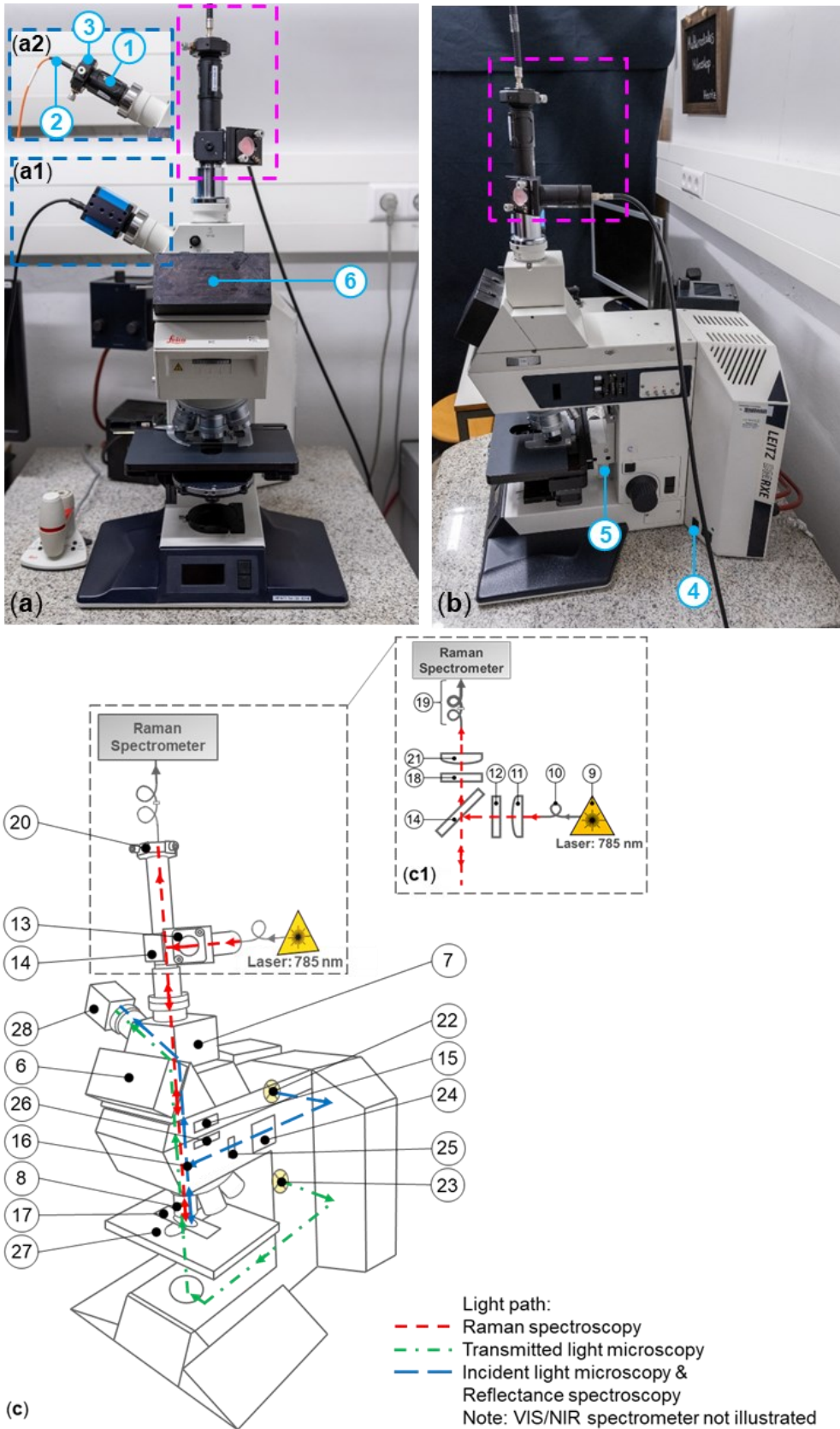


Figure 3 Modified microscope Leica DM R: (a) front view including camera (a1) and tube system of the expanded reflectance spectroscopy (a2), (b) side view, (c) schematic drawing¹ including the light path of the expanded Raman spectroscopy (c1). Note: The position of the analyser (26) in the schematic drawing (c) differs from its actual position (opposite side of the cover plate).

Table 2 Description of the numbering depicted in Figure 3.

No.	Specification
1	Plano-convex lens, focal length = 25 mm, LA1951; [Thorlabs Inc., Newton, NJ, USA]
2	Multimode optical fibre: core diameter = 50 μm , NA = 0.22, FC/PC ferrules, M14L02; multimode optical fibre, core diameter = 550 μm , NA = 0.22, FC/PC–SMA ferrules, FG550LEC; FC/PC to FC/PC mating sleeve: ADAFC1; [Thorlabs Inc., Newton, NJ, USA]
3	Translation mount (XY Translator), CXY1; FC/PC fibre adapter plate, SM1FC; [Thorlabs Inc., Newton, NJ, USA]
4	Transmitted/incident light selector switch; [Leica Microsystems GmbH, Wetzlar, Germany]
5	Mechanical stop; [CeMOS, Mannheim University of Applied Sciences, Mannheim, Germany]
6	Cover lid; [CeMOS, Mannheim University of Applied Sciences, Mannheim, Germany]
7	Interchangeable photo adapter tube Leica Microsystems GmbH, Wetzlar, Germany
8	Sextuple nosepiece (BD, M32), HC; Microscope objectives: 5x, NA: 0.12, N PLAN; 10x, NA: 0.25, N PLAN; BD20x, NA: 0.50, HC PL FLUORTAR; 40x, NA: 0.65, N PLAN; BD50x, NA: 0.85, PL APO; BD100x, NA: 0.90, PL APO; [Leica Microsystems GmbH, Wetzlar, Germany]
9	785 nm diode laser, adjustable laser power (50–500 mW) tec5 AG, Steinbach, Germany
10	Multimode optical fibre: core diameter = 100 μm , FC/PC ferrules; [Prinz Energietechnik GmbH, Stromberg, Germany]
11	Plano-convex lens, focal length = 25 mm, LA1951-B; [Thorlabs Inc., Newton, NJ, USA]
12	Laser line filter, FWHM = 3.0 nm, #68–947; [Edmund Optics, Barrington, NJ, USA]
13	Right-angle kinematic mirror mount, KCB/M + dielectric mirror, BB1-E03; [Thorlabs Inc., Newton, NJ, USA]
14	Laser dichroic beamsplitter 785 nm laser BrightLine® single-edge, Di02-R785-25x36 Semrock Inc., Rochester, NY, USA Cage cube, CM1-DCH/M; [Thorlabs Inc., Newton, NJ, USA]
15	Tube optics, HC: 1.25x, 1.6x, Scan, Bertrand lens; [Leica Microsystems GmbH, Wetzlar, Germany]
16	Incident light turret: BF reflector, DF reflector, Smith reflector, adjustment reflector; [Leica Microsystems GmbH, Wetzlar, Germany]
17	Gold-coated slide: BioGold®, E63479-AS; [Science Services GmbH, Munich, Germany] Glass slide: SuperFrost® slide; [VWR, Radnor, PA, USA]
18	Longpass filter, 785 nm EdgeBasic™ best-value long-pass edge filter, BLP01-785R-25; [Semrock Inc., Rochester, NY, USA]
19	Multimode optical fibre: core diameter = 100 μm , NA = 0.22, FC/PC ferrules multimode optical fibre: core diameter = 600 μm , NA = 0.22, FC/PC–SMA ferrules; [Prinz Energietechnik GmbH, Stromberg, Germany] FC/PC to FC/PC mating sleeve: ADAFC2; [Thorlabs Inc., Newton, NJ, USA]
20	Translation mount (XY Translator), CXY1; FC/PC fibre adapter plate, SM1FC; [Thorlabs Inc., Newton, NJ, USA]
21	Achromatic lens, focal length = 30 mm, AC254-030-B; [Thorlabs Inc., Newton, NJ, USA]

No.	Specification
22+23	Halogen lamp, HLX GY6.35, 12 V, 100 W; [Osram Licht AG, Munich, Germany]
24	Diaphragm module HC RF; [Leica Microsystems GmbH, Wetzlar, Germany]
25	Polariser R/P (switchable vibration direction); [Leica Microsystems GmbH, Wetzlar, Germany]
26	Analyser IC/P with whole-wave compensator, vibration direction: East-West; [Leica Microsystems GmbH, Wetzlar, Germany]
27	Motorized microscope stage, EK 14 mot, travel range 3" x 2"; [Märzhäuser Wetzlar GmbH & Co. KG]
28	Colour camera, DFK 41AF02, 1280 x 960 pixels (1.2 MP), 8-bit (dynamic range), CCD sensor, IR cut filter, [The Imaging Source Europe GmbH, Bremen, Germany]

In the photographs (Figure 3(a,b)), the adapted Raman path is framed by a pink rectangle. The blue frames in Figure 3a highlight the last section of the detection paths for the microscopic modalities with the mounted charge-coupled device (CCD) camera (a1) and the newly added visible/near-infrared (VIS/NIR) reflectance spectroscopy (a2). Since the photo adapter tube has only two exit ports where one is permanently occupied for Raman spectroscopy, either the camera (a1) or the tube system (a2) is physically connected to the setup. Nevertheless, the light path for the incident light microscopy and the reflectance spectroscopy is identical. This light path is illustrated by the blue dashed line in Figure 3c. The light of the upper halogen lamp is laterally guided through the incident light axis of the microscope. The reflector reflects the excitation light at a 90° angle downwards onto the sample, while the at the gold coating back-scattered light passes the reflector. Subsequently, the light propagates vertically through the microscope stand. The tilted mirror in the interchangeable photo adapter tube reflects the light to the sidewise exit port. For VIS/NIR reflectance spectroscopy (Figure 3(a2)), an inside the tube system (Ø1", Thorlabs Inc., Newton, NJ, USA) mounted plano-convex lens (1) is used to focus the light onto a 50 µm pinhole fibre (2). For an entire illumination of the spectrometers' (VIS and NIR spectrometer) entrance slit, the 50 µm fibre is coupled to a further 550 µm fibre via a mating sleeve. A translating mount for the fibre adapter plate (3) facilitates the pinhole fibre's lateral (x, y) orientation to maximise the detection signal. To enable the detection of NIR photons, the heat-absorbing filter (not illustrated) in the upper lamp housing is permanently removed. This filter is an infrared-blocking filter. In return, infrared radiation in colour cameras falsifies colour reproduction compared to visual colour perception.⁹² For this reason, a colour camera with an internal infrared-blocking

filter (filter type: 486, <https://www.theimagingsource.de/produkte/optik/filter/>, accessed 17th January 2022) is used.

The colour camera is also applied to record photographs in the transmitted light mode. The corresponding light path is indicated by the green dash-dotted line in Figure 3c. Thereby, the light from the lower placed halogen lamp propagates laterally along the microscope's optical axis in the bottom part of the microscope stand. After reflecting at a tilted mirror, the light penetrates the sample from bottom to top. The subsequent detection path is identical to the blue detection path of the incident light modes.

The last light path (red densely dashed line) belongs to the newly adapted path for Raman spectroscopy. As a light source, an external laser is mandatory. Since the microscope is equipped with a selector switch (Figure 3b, (4)) for permanent use with either the incident or the transmitted light, an additional switch (not illustrated) is integrated into the power cable of the incident light source. Hence, Raman spectroscopy can be performed as required, while both internal light sources of the microscope are turned off. A further microscope modification is a mechanical stop (Figure 3c, (5)) at the dovetail guide below the microscope stage. This is required to avoid sinking because of the stage clamp's malfunction.

An in-house manufactured cover lid ((6), material: polylactic acid (PLA), 3D printer, Ultimaker 2 extended+, Ultimaker B.V., Utrecht, Netherlands) is permanently installed at the microscope tube. For this purpose, the eyepieces are removed. Since the microscope tube is mandatory as a connecting unit of the whole setup, the beam splitter unit inside the tube is detached to deactivate the visual observation path. The deactivation and the coverage of this light path are safety precautions to prevent an accidental exit of the laser beam for Raman spectroscopy.

The Raman unit, including the excitation and the detection path, is configured using the lens tube system ($\varnothing 1''$) from Thorlabs Inc., Newton, NJ, USA. It is connected to the microscope via the vertical exit port of the interchangeable photo adapter tube (7). Such an arrangement in the reflection mode is a commonly used measuring principle to collect Raman spectra in biomedical applications.⁶⁶ To obtain Raman spectra from a microscopic area with high collection efficiency, a microscope objective with a high numerical aperture (NA) is recommended.³² In addition, the depth resolution increases the higher the NA. In return, cryosections with a high topography will likely be sometimes out of focus when using a high NA. Based on this advice, Raman and VIS/NIR intensity spectra are recorded applying the BD50x objective (dry objective)

with an NA of 0.85 (8). To reach the objective's entire NA and achieve the smallest possible (diffraction-limited) focal spot size, it is obligatory to generate a beam diameter of the excitation light larger than the diameter of the exit pupil.⁹³ This exit pupil is a physical aperture located inside the objective.⁹⁴ Its diameter (D) is determined using equation 7:

$$D = \frac{2 \cdot F \cdot NA}{M} \quad (7)$$

where F : focal length of the tube lens
 NA : numerical aperture
 M : magnification of the objective

The focal length for Leica microscopes with infinite tube length is 200 mm.⁹⁴ Inserting this focal length, the magnification, and the NA in equation 7, result in a diameter of 6.8 mm for the present objective. Since the VIS/NIR spectroscopy's incident light path is identical to the microscope's incident light path, the appropriate beam diameter was already designed by Leica. The configured light path for Raman spectroscopy in this study is as follows.

First of all, the 785 nm laser (9) is connected to the setup via a 100 μm (core diameter) optical fibre (10). Subsequently, a plano-convex lens (11) collimates the laser light. The lens is selected based on a requested beam simulation by the manufacturer (Thorlabs Inc.). Thereby, the full width at half maximum (FWHM) value of the collimated beam was determined at a distance of 50 cm. This distance is identical to the physical distance between the lens and the microscope objective. The simulated FWHM of the collimated beam diameter resulted in 7 mm. This value fulfils the criterion to overfill the objective's pupil. Moreover, the lens contains a wavelength-optimised coating to reduce surface reflection.

Another requirement on Raman spectroscopy is a narrow spectral intensity distribution of the laser to avoid broadening of the Raman peaks.³² Therefore, a laser line bandpass filter (12) that transmits the laser's main excitation line is used. At the same time, spectral noise should be eliminated by exclusively transmitting the laser wavelength. The importance of the appropriate bandpass filter is described below. Figure 4 shows the transmission spectra of two different bandpass filters (BPF1 and BPF2) and the intensity spectrum of the 785 nm laser.

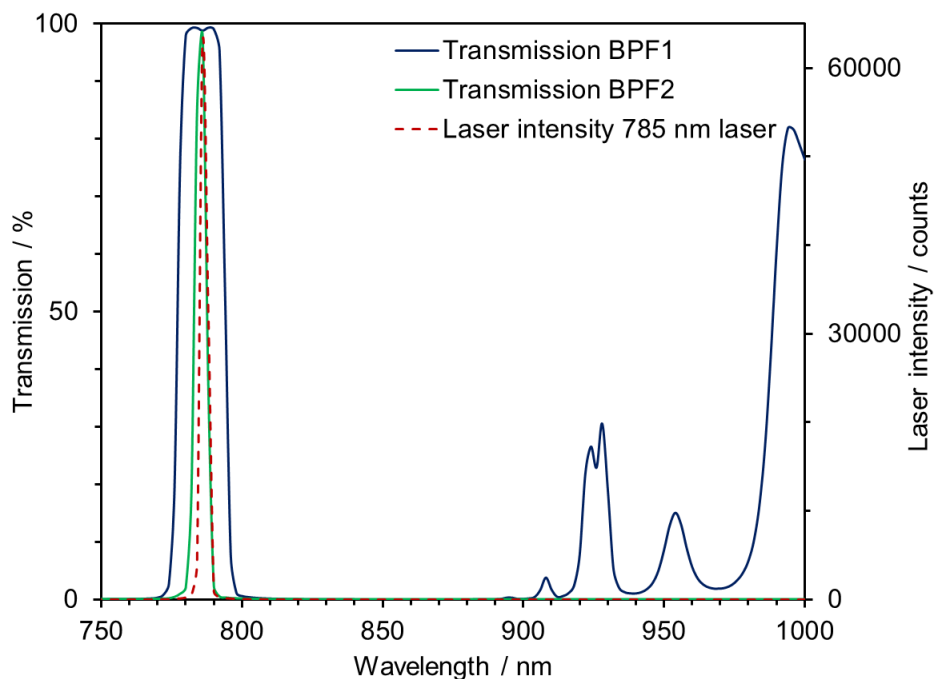


Figure 4 Primary axis: Transmission spectra of the bandpass filters BPF1 and BPF2 (see text for specifications), secondary axis: Intensity spectrum of the 785 nm laser.

The spectrometer used to record all spectra is the UV-NIR spectrometer MCS 601 VIS-NIR (Carl Zeiss Spectroscopy GmbH, Jena, Germany) with a wavelength range of 180 nm to 1000 nm and a spectral resolution of 3.5 nm. However, spectra are plotted in a spectral region from 785 nm to 1000 nm. This wavelength range is similar to the Raman shifts detected with the MultiSpec[®] Raman System. Although the maximum peak intensity at 785 nm in the laser's intensity spectrum lies in the transmission range of both bandpass filters, the transmission range of BPF1 (MaxDiode[™] laser clean-up filter, FWHM = 17.1 nm, LD01-785/10-12.5, Semrock Inc., Rochester, NY, USA) is broader than the transmission range of BPF2 (laser line bandpass filter, FWHM = 3.0 nm, #68-947, Edmund Optics Inc., Barrington, NJ, USA). Additionally, BPF1 (blue spectrum) has the disadvantage to be partially optical semi-transparent at wavelengths above 900 nm. The impact of this semi-transparency on the detected Raman spectra is illustrated in Figure 5.

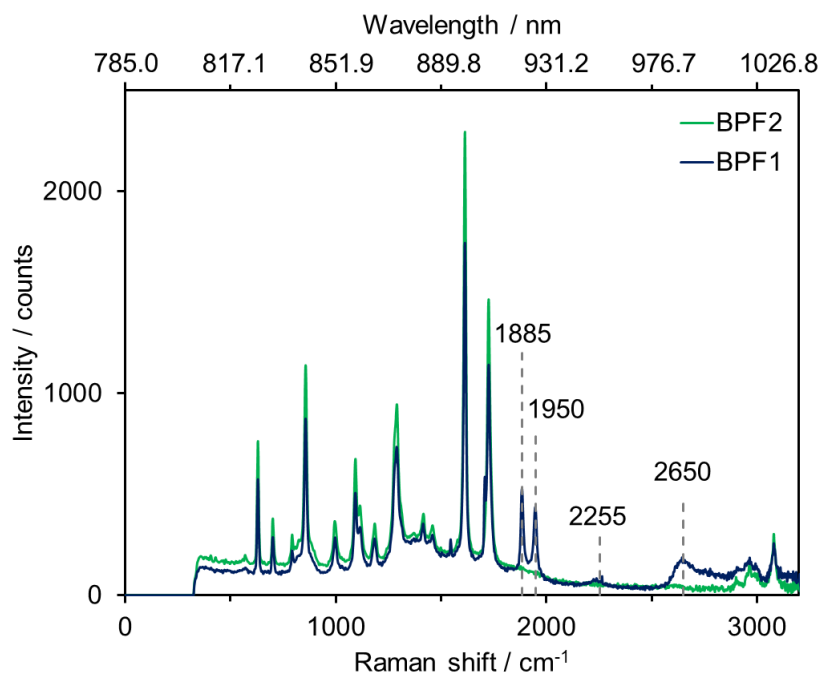


Figure 5 Raman spectra of a PET film on a microscope slide using the bandpass filters BPF1 and BPF2 (see text for details). Note: The difference in Raman intensities using BPF1 and BPF2 is not addressed since the setup might be misaligned during the manual filter exchange.

Both curves show the Raman spectrum of a 100 μm thick transparent polyethylene terephthalate (PET) film (Tartan 901, 3M, Saint Paul, MN, USA) on a standard glass slide (ECN 631-1553, VWR, Randor, PA, USA). It is noticeable that the Raman spectrum recorded with BPF1 (blue spectrum) shows four additional peaks above 1880 cm^{-1} . The peaks' positions are identical to the positions of the additional peaks in the transmission spectrum in Figure 4. The sharper peak separation of the double peak at 1885 cm^{-1} (924 nm) and 1950 cm^{-1} (928 nm) in the Raman spectrum in contrast to the transmission spectrum is due to the Raman system's higher spectral resolution ($\Delta\lambda_s \approx 0.6$ nm) compared to the spectral resolution of the UV-NIR spectrometer ($\Delta\lambda_s \approx 3.5$ nm). However, these peaks are rather spectral noise of the setup than molecular specific Raman peaks of PET. Since the peaks are long-wave shifted, the signal might be broadband fluorescence signal or Stokes Raman scattering originating from the core material (quartz) of the optical fibre (Figure 3(c1), (10)). Anyhow, to avoid recording spectral noise and the misinterpretation of Raman peaks, BPF2 is used. The subsequent optical component in the Raman excitation path is a dielectric mirror, placed on a right-angle kinematic mirror mount (13). The mirror mount facilitates the adjustment of the laser beam for optimal illumination of the microscope objective. Before the monochromatic light enters the objective, a dichroic beamsplitter in a cage

cube (14) reflects the laser beam downwards at a 90° angle through the microscope stand. In the microscope stand, all optical components are removed to optimise for the highest transmittance and to avoid beam deformation. This is why the 1.6x lens in the tube optic's turret (15) is completely removed. Consequently, position 1.6x of the tube optics results in a passage hole in the cover plate for transmission of the light beam. Due to the 180° backscattering arrangement of the excitation path and detection path, any reflector (16) required for incident light microscopy is detached. After penetrating the microscope stand, the BD50x objective (8) focuses the laser light onto the cryosection mounted on the gold-coated slide (17). The backscattered light is collected by the identical objective. Both the elastic and inelastic portion of the backscattered light propagates upwards through the microscope stand and the interchangeable photo adapter tube (7). The switch rod in the adapter tube is pulled so that the beam transmits vertically (100% to the top) without passing any optics.

93% of the inelastically scattered light between 804.3 nm and 1200 nm passes the dielectric beamsplitter (14). Elastically scattered light and the higher energetic anti-Stokes scattered light is blocked by the beamsplitter and the subsequent longpass filter (18). The remaining multiple-wavelength Stokes scattered light is detected by the Raman spectrometer included in the MultiSpec® Raman System. For maximum illumination of the spectrometer's entrance slit, a 600 µm (core diameter) fibre with an NA of 0.22 is required. Besides the appropriate illumination, optical fibres can guide the light with minimum losses (4% at the entrance and the exit).³² Another fibre with a smaller diameter but an identical NA is coupled in front of the 600 µm fibre (19). The smaller fibre acts as a pinhole that ideally collects the Raman signal from a microscopic area while the signal out of the focal plane like stray light is suppressed. A translation mount for the fibre adapter plate (20) enables the lateral orientation of the pinhole fibre to maximise the detected Raman signal.

Prior to this, the Raman signal is focused onto the fibre by an achromatic lens (21). Such a lens type instead of a plano-convex lens is used to minimise chromatic aberration caused by the lens' varying dispersion properties as a function of wavelength.⁹⁵ Similar to the lens in the excitation path, the achromatic lens has an anti-reflection coating to minimise surface reflections. The manufacturer (Thorlabs Inc.) calculated the spot size (FWHM value) of the focused Raman signal on request. With the assumption that the beam diameter of the collimated light is equal to the diameter of the exit pupil (6.8 mm), the spot size resulted in 12 µm. However, the actual value

might differ from the simulated (ideal) value due to a variation in beam diameter, a manufacturing inaccuracy of the optical components, or an imprecision of the optical arrangement of the achromatic lens and the pinhole fibre. Therefore, the diameter of the pinhole/detection fibre is chosen based on the results of the following experiments.

3.1.1 Diameter of pinhole fibre

The first experiment to determine the appropriate fibre diameter is carried out recording Raman spectra of a silicon wafer (thickness: 500 μm) on a standard microscope slide (ECN 631-1553, VWR, Randor, PA, USA) at various height positions (z) of the microscope stage using detection fibres with different diameters. The declaration of the diameter refers to the fibres' core diameter made of quartz. The core is the part of step-index multimode fibres where the light is guided by frequently recurring total reflection at the fibres' internal core-cladding interface.⁹⁶ To achieve total reflection while minimising reflection losses, bending the fibre should be avoided. The limiting value for a 100 μm fibre's radius of curvature is in the order of 10 cm.⁹⁷ While performing all experiments, care is taken to ensure that the curvature radius of the fibres is sufficiently large.

The maximum fibre diameter is 600 μm (Prinz Energietechnik GmbH, Stromberg, Germany). As mentioned in chapter 3.1, such a diameter guarantees an entire illumination of the Raman spectrometer's entrance slit. Further fibre diameters are 200 μm (M122L01, Thorlabs Inc., Newton, NJ, USA), 100 μm (Prinz Energietechnik GmbH, Stromberg, Germany) and 50 μm (M42L02, Thorlabs Inc., Newton, NJ, USA). The NA of all fibres is 0.22. The connecting of each fibre with the 600 μm fibre sustains the optimal illumination of the entrance slit. A coupling of two fibres is marked subsequently by a plus sign between the two numbered diameters. The 600 μm is not coupled.

In the experiment, Raman spectra are recorded with an integration time of 1000 ms and the laser power is set to the maximum value of 500 mW.

For data evaluation, the intensity of the silicon wafer's main peak around 520 cm^{-1} minus an offset intensity is calculated. An example of one recorded silicon spectrum is shown in Figure 6. The Raman peak at 520 cm^{-1} is marked by the vertical dashed line. The grey areas from 480 cm^{-1} to 489 cm^{-1} and from 550 cm^{-1} to 559 cm^{-1} display the

range where the offset value is determined by averaging the total 20 (data interval: 1 cm^{-1}) values.

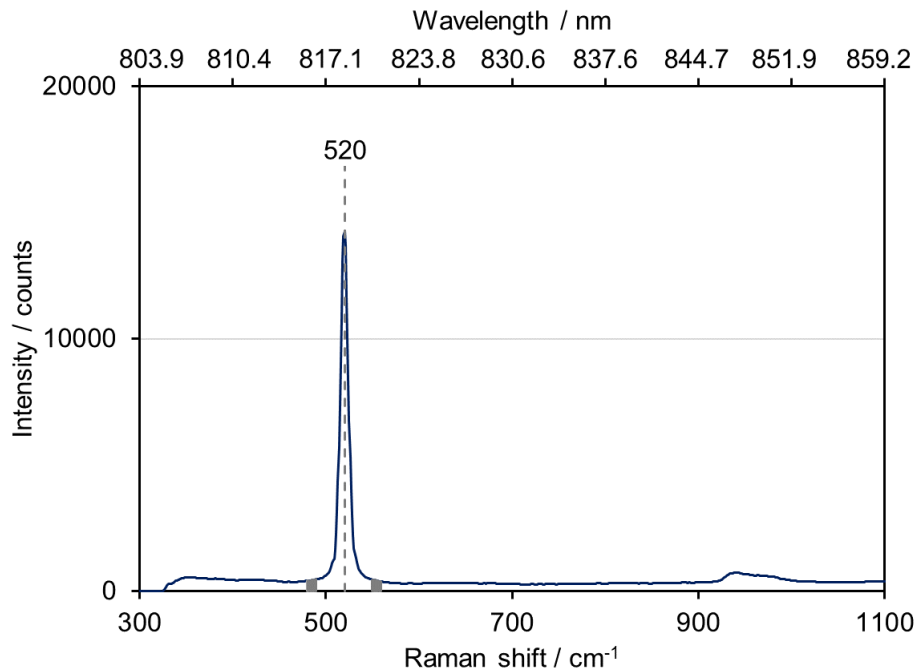


Figure 6 Raman signal of silicon on a microscope slide (see text for details). Setup configuration: Raman spectroscopy, laser power: 500 mW, objective: BD50x, $d_{\text{fibre}} = 100+600 \mu\text{m}$, integration time: 1000 ms.

At the same time, the peak location of the silicon's main peak at 520 cm^{-1} verifies the Raman spectrometer's accurate calibration by the manufacturer (tec5 AG).

Compared to the data recording with the MultiSpec® Pro II software (in total: 3226 values, data interval: 1 cm^{-1}), Raman spectra recorded with the developed LabVIEW™ programme during the scanning experiments contain 1044 (number of pixels) measuring values. An interpolation of the single measuring values as in the manufacturer's software is not performed. Consequently, the spectral resolution of the Raman spectra recorded with the LabVIEW™ programme is decreased (poorer resolution) and peak positions are slightly shifted (Silicon peak: 519.69 cm^{-1}) due to the lack of interpolation.

This experiment collects data with the MultiSpec® Pro II software at the microscope stage's height between $-1000 \mu\text{m}$ and $200 \mu\text{m}$. Due to the optical arrangement of the setup with the interchangeable photo adapter tube (Figure 3c, (7)), the light paths for Raman spectroscopy is independent, and the laser light is never visible on the camera. Therefore, the zero value of the stage is always referred to as the level where photographs are obtained (focus) in the incident light bright-field mode using the BD50x objective. An increase in the z value (positive numbers) corresponds to an

approach of the stage and the objective. In contrast, the distance between the stage to the objective increases with decreasing z values.

For better comparison, the maximum calculated intensity of each fibre is normalised to 100% and the corresponding z -position is assigned to $z = 0$ (see Figure 7).

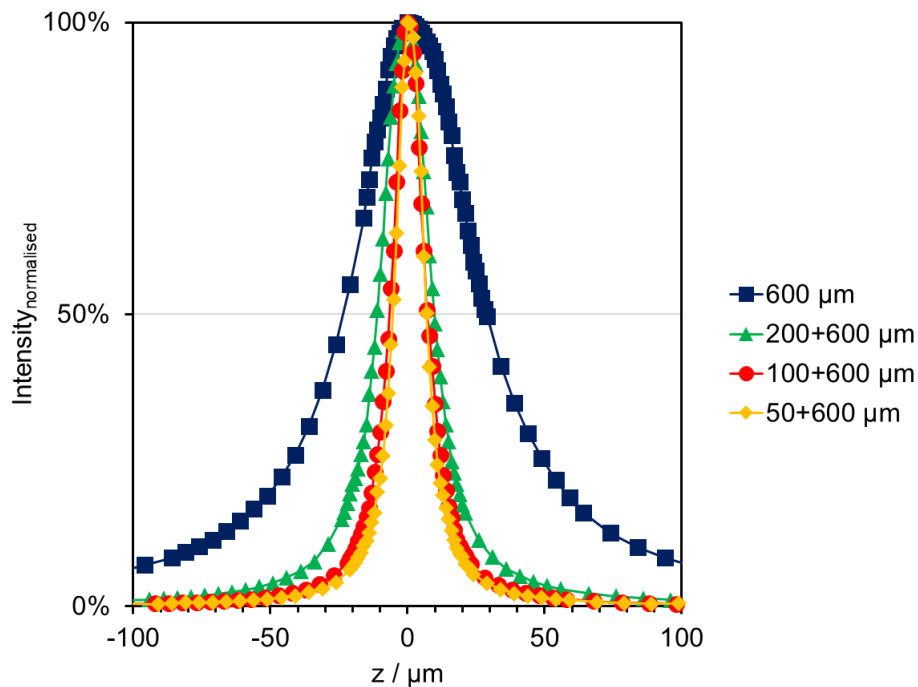


Figure 7 Normalised intensity of the silicon peak at 520 cm^{-1} versus height position (z) of microscope stage, using different diameters of detection fibre. Setup configuration: Raman spectroscopy, laser power: 500 mW, objective: BD50x, integration time: 1000 ms.

Based on the illustration in Figure 7, the bell-shaped curve of the 600 μm fibre (blue curve) is broader than the curves of a smaller fibre diameter. A parameter to quantify these differences is the FWHM value. This value refers to the width at an intensity of 50%. The FWHM value of the 600 μm fibre is 52.2 μm , 2.5 times larger than the value for the 200 μm fibre (green curve, FWHM = 20.9 μm) and 4.2 times larger than the 50 μm fibre (orange curve, FWHM = 12.3 μm). As expected, the FWHM value of the 100 μm fibre (red curve, FWHM = 13.8 μm) lies in between the value for the 50 μm and 200 μm fibre. However, the relation between the FWHM value and the fibre diameter is not linear. The FWHM of the 100 μm fibre is 1.5 times smaller than the 200 μm fibre but 1.1 times higher than the 50 μm . To sum up, it can be stated that the 50 μm fibre results in the smallest FWHM.

It is inappropriate to declare the respective FWHM value as the setup's depth resolution. Investigations of Overall⁹⁸ proved that a prolongation of the laser focus due

to a mismatch of refractive indices ($n_{\text{sample}} \neq n_{\text{measuring environment}}$) results in a poorer depth resolution than the actual value. Furthermore, with increasing depth, the Raman intensity is attenuated.⁹⁸

The signal intensity of the recorded Raman peaks is an important fact that must be considered when selecting the appropriate fibre diameter. The relation between the intensity of the Raman signal and the diameter of the detection fibre is determined based on the following considerations.^d

First of all, it is assumed that the intensity profile of the Raman signal at the detection fibre's entrance is 2-dimensional normal (Gaussian) distributed over the fibre's cross-sectional area where the intensity declines as a function of the fibre radius^e (r_f). The maximum intensity (I_0) is localised in the fibre's centre where $r = 0$.

The intensity (I) is described as

$$I = I_0 \cdot e^{-\frac{r^2}{2\sigma^2}} \quad (8)$$

where I_0 : maximum intensity (unit: W/m²)
 r : radial coordinate (unit: μm)
 $\pm\sigma$: inflexion point ($I''(\pm\sigma) = 0$) where $I = 0.61 \cdot I_0$ (unit: μm)

At this point, it has to be mentioned that the intensity (unit: W/m²) of equation 8 is not identical to the intensity (unit: counts) of the recorded Raman or VIS/NIR spectra. This signal intensity in counts is proportional to the power (P).

To calculate P based on the intensity of equation 8, the area under the curve is determined by integrating over the fibre's cross-sectional area using equation 9.

$$P = \int_0^{2\pi} \int_0^{r_f} I(r) r dr d\varphi \quad (9)$$

Inserting equation 8 into equation 9 and solving the integral results in

$$P = 2\pi \cdot I_0 \cdot \sigma^2 \cdot \left(1 - e^{-\frac{r_f^2}{2\sigma^2}}\right) \quad (10)$$

^d The mathematical model to describe the coupling efficiency of fibres for Gaussian beam profiles is worked out with the assistance of Prof. Dr. Thomas Beuermann.

^e Note: The fibre radius instead of the fibre diameter is used for the subsequent calculations.

where P : intensity (unit: W)
 I_0 : maximum intensity (unit: W / m²)
 $\pm\sigma$: inflexion point ($I''(\pm\sigma) = 0$) where $I = 0.61 \cdot I_0$ (unit: μm)
 r_f : fibre radius (unit: μm)

To assess the collection efficiency as a function of the fibre radius, the ratio between $P(r_f)$ and $P_{300\ \mu\text{m}}$ is calculated assuming that the total detectable Raman signal (P_{total}) is captured by the 600 μm ($r = 300\ \mu\text{m}$) fibre. The corresponding equation 11 is:

$$\frac{P(r_f)}{P_{300\ \mu\text{m}}} = \frac{2\pi \cdot I_0 \cdot \sigma^2 \cdot \left(1 - e^{-\frac{r_f^2}{2\sigma^2}}\right)}{2\pi \cdot I_0 \cdot \sigma^2} = 1 - e^{-\frac{r_f^2}{2\sigma^2}} \quad (11)$$

The variable σ is determined based on a simulation applying the solver, a Microsoft Excel-Add-In.

The objective of the solver application is to minimise the sum of the absolute differences between the simulated (equation 11) and the experimentally determined ratio of $P(r_f)$ and $P_{300\ \mu\text{m}}$. Experimental data for the four different fibre diameters is obtained from Raman spectra of PET (Tartan 901, 3M, Saint Paul, MN, USA) on a microscope slide (ECN 631-1553, VWR, Randor, PA, USA), see Figure 8.

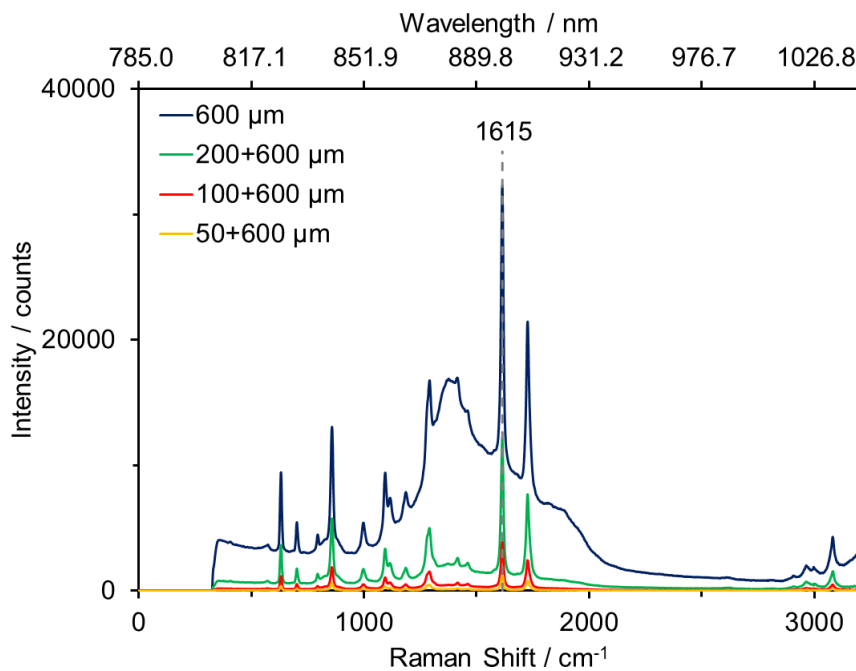


Figure 8 Raman spectra of PET on a microscope slide, using different diameters of detection fibre; setup configuration: Raman spectroscopy, laser power: 500 mW, objective: BD50x, integration time: 1500 ms.

Each spectrum is recorded at the stage's height position (z) where the Raman signal of PET is maximised. To rate each fibre's signal intensity, the highest Raman peak at 1615 cm^{-1} is selected. This peak, marked by the grey vertical line in Figure 8, corresponds to the C=C stretching (ring) mode.⁹⁹ The peak's actual intensity is calculated by subtracting the mean value of the intensities from 1550 cm^{-1} to 1559 cm^{-1} and 1650 cm^{-1} to 1659 cm^{-1} (in total: 20 values). This offset correction is mandatory since the detected signal contains the PET's Raman signal but also a fluorescence background signal caused by the glass of the standard microscope slide. Using an excitation wavelength of 785 nm results in a broad fluorescence background peaking at approximately 1400 cm^{-1} .⁷⁴ Especially the $600\text{ }\mu\text{m}$ fibre (blue curve) detects a broad fluorescence background, a consequence of the high detection volume when using larger fibre diameters. However, the Raman intensity increases the higher the detection volume.

Despite the coupling from the smaller fibre to the larger ($600\text{ }\mu\text{m}$) fibre with identical NAs, intensity losses are unavoidable in practice due to the interface of the two fibre surfaces. For this reason, the calculated Raman intensity at 1615 cm^{-1} using the $600\text{ }\mu\text{m}$ fibre (no coupling) is multiplied by a coupling factor to adjust this intensity for direct comparison. Consequently, the experimentally calculated Raman intensities at fibre diameters of $50\text{ }\mu\text{m}$, $100\text{ }\mu\text{m}$, and $200\text{ }\mu\text{m}$ are divided by the factorised intensity of the $600\text{ }\mu\text{m}$ fibre. Besides σ , the coupling factor is the second variable of the solver application. Additionally, the constraint that the coupling factor has to be smaller or equal to 1 is set.

The solver finds a solution satisfying the constraint and all conditions at a sum of the absolute differences between the simulated and the experimentally determined power ratios of 0.012. An illustration of the evaluation is shown in Figure 9.

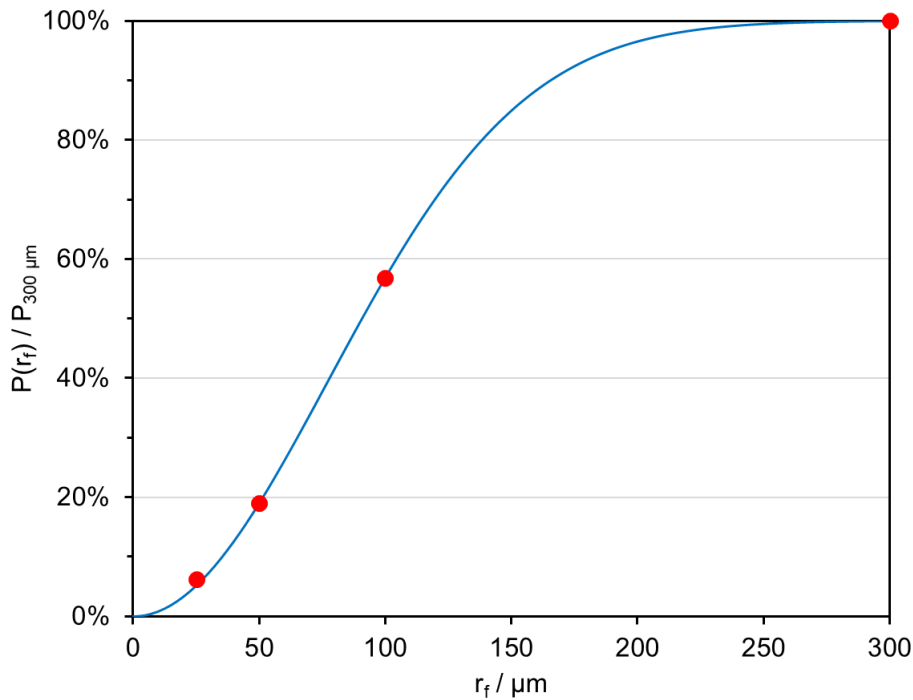


Figure 9 Normalised Raman signal as a function of the detection fibre's radius (r_f); red dots: experimental data, blue curve: simulation based on a 2d Gaussian function; σ : 77.15 μm , coupling factor: 0.86.

The red dots are based on experimental data, while the blue line represents a plot of equation 8 with $\sigma = 77.15 \mu\text{m}$. The coupling factor for the 600 μm fibre is determined as 0.86. This value seems plausible since a small set of experiments ($n = 3$) coupling two identical 550 μm fibres results in a mean coupling loss of 90% in the wavelength range from 785 nm to 1000 nm (data not shown). Furthermore, a sigma value of 77.15 μm results in a light coupling of 99.95% into the 300 μm fibre due to equation 11. The curve's minimum value of 0% at $r_{0 \mu\text{m}}$ and maximum value of 100% at $r_{300 \mu\text{m}}$ are also reasonable.

To summarise, the normalised Raman signal at 1615 cm^{-1} as a function of the fibre radius can be described with a 2-dimensional Gaussian distributed intensity profile. The special characteristic about the present distribution is that the Raman intensity does not increase linearly with the fibre radius.

As an example, reducing the fibre radius by a factor of 6 (from 300 μm to 50 μm) results in a decrease of the detected Raman intensity by a factor of 5.3 (19% of the maximum detectable Raman signal) and the reduction from 300 μm to 100 μm (factor 3) remains 57% (factor 1.75) of the detectable Raman signal intensity (see Figure 9).

At the same time, the interfering fluorescence background signal increases the larger the fibre radius. Figure 10 illustrates the normalised fluorescence signal as a function of the fibre radius.

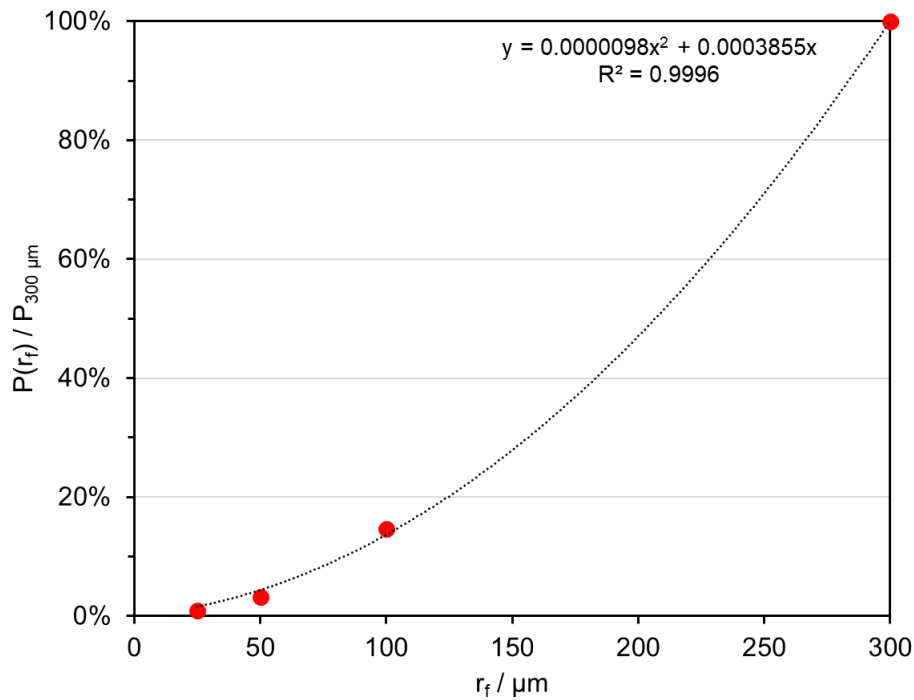


Figure 10 Normalised fluorescence (background) signal as a function of the detection fibre's radius (r_f); red dots: experimental data, black curve: regression (second-degree polynomial equation); coupling factor: 0.86.

Similar to Figure 9, the red dots represent experimental data. For evaluation, the intensity signal of the broad fluorescence peak at 1380 cm^{-1} in the Raman spectra, shown in Figure 8, is used. Analogue to the analysis of the Raman signal, the signal intensity is normalised to the maximum detectable fluorescence signal with $600 \mu\text{m}$ ($r_{300 \mu\text{m}}$) fibre. In advance, the coupling factor of 0.86 for the $600 \mu\text{m}$ fibre is also applied to this evaluation. However, the fluorescence signal is approximated by a second-degree polynomial equation. Since the PET foil is placed in the focal plane of the Raman setup and the fluorescence signal originates from the glass substrate below the foil, it is not expected that the background signal is normally distributed. Furthermore, the trend line in Figure 10 indicates that a decrease in fibre radius is beneficial in terms of background reduction.

To rate the impact of the fibre radius on the detected Raman and fluorescence signals, the quotient of the calculated Raman and fluorescence intensity, adapted from Figure 9 and Figure 10, is formed. The result is shown in Figure 11.

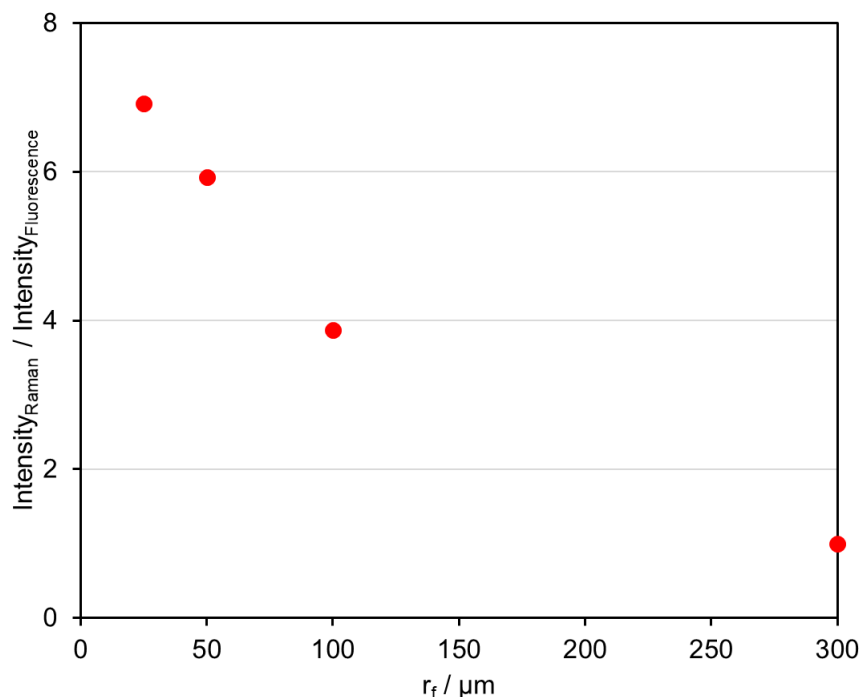


Figure 11 Normalised intensity ratio of the calculated Raman and fluorescence signals as a function of the detection fibre's radius (r_f); red dots: experimental data.

As expected, the calculated ratio of the fibre with a radius of 300 μm is 1. The highest value (7.9) is achieved with a fibre radius of 25 μm . The 100 μm ($r_{50 \mu\text{m}}$) and 200 μm ($r_{100 \mu\text{m}}$) fibres have quotients of 5.9 and 3.9, respectively. Based on Figure 11, a detection fibre with a diameter of 50 μm seems the appropriate configuration for Raman spectroscopy.

However, one of the most significant parameter of analytical analyses is the signal-to-noise ratio (SNR).

Signal-to-noise ratio

Rigorously, the SNR for a peak intensity of a Raman band is defined as the average peak height (above a baseline) divided by the standard deviation of the peak height.¹⁰⁰ Since all Raman spectra are obtained without any accumulation ($n = 1$), the determination of the SNR as the quotient of the peak height and its standard deviation is not possible. To calculate the SNR of a Raman band in this study, the peak intensity, after subtracting an offset value, is divided by the factorised standard deviation of a Raman shift segment from 2500 cm^{-1} to 2519 cm^{-1} (in total: 20 values, data interval: 1 cm^{-1}) in the silent region. Determining the standard deviation based on a Raman shift range in the fingerprint (700-180 cm^{-1}) or the high-wavenumber region (2800-3050 cm^{-1}) close to the analysed Raman band is not suitable. The reason is the

high density of Raman peaks, especially in biological samples, in combination with the spectrometer's spectral resolution.

The unbiased estimation of the standard deviation (s) is defined as the square root of the variance (Var) according to equation 12.

$$s = \sqrt{Var} = \sqrt{\frac{\sum_{i=1}^n (x_i - \bar{x})^2}{n - 1}} \quad (12)$$

where x_1, x_2, \dots, x_n : intensity values (unit: counts)

\bar{x} : mean value of intensity (unit: counts)

n : number of intensity values

To compare the different fibre diameters, the SNR for the PET peak at 1615 cm^{-1} of the spectra in Figure 8 is calculated. The Raman peak height is defined as the signal intensity at 1615 cm^{-1} minus the average value of the intensities at 1580 cm^{-1} and 1640 cm^{-1} (offset values). Only two signal intensities are intentionally averaged to ensure that the offset value is a background signal instead of another Raman peak. This is particularly important for determining the SNR of the later tissue experiments because Raman peaks in biological samples are closer to each other.

Because of the varying sensor sensitivity over the spectral region and the associated pixel weighting due to the correction file, the standard deviation (equation 12) from the shift segment in the silent region is factorised to adjust the standard deviation to the sensor's sensitivity in the spectral region of the analysed Raman band. The factor is the ratio of the correction file's pixel weighting in the Raman shift range of the signal and the shift segment in the silent region. For the present case (PET peak at 1615 cm^{-1}), the standard deviation of equation 12 is multiplied by 0.65.

Dividing the actual peak height at 1615 cm^{-1} (\triangleq signal) by the factorised standard deviation (\triangleq noise) results in an SNR of 270 for the $50 \text{ }\mu\text{m}$ fibre. The SNR of the $100 \text{ }\mu\text{m}$ fibre is 4.3 times higher ($\text{SNR}_{100 \text{ }\mu\text{m}} = 1173$), and the SNR of the $200 \text{ }\mu\text{m}$ fibre is 8.5 times higher ($\text{SNR}_{200 \text{ }\mu\text{m}} = 2295$) than the SNR of the $50 \text{ }\mu\text{m}$. The best SNR is achieved with the $600 \text{ }\mu\text{m}$ fibre. This SNR is 7129, 26.4 times higher than the SNR of the $50 \text{ }\mu\text{m}$ fibre. In contrast, the $600 \text{ }\mu\text{m}$ fibre detects a background signal of the glass slide that is 128.2 times higher than the background signal detected with the $50 \text{ }\mu\text{m}$. The final decision of the most suitable diameter for the detection fibre of the Raman path is made after the last experiment, determining the lateral resolution.

Lateral resolution of Raman path

To specify and judge image quality, the modulation transfer function (MTF) is the most accepted criterion.¹⁰¹ The MTF is a parameter that directly quantifies the projection of various object details in the image.¹⁰¹ It is defined as the ratio of the image contrast (M_{image}) and the object contrast (M_{object}) as a function of the spatial frequency (ν).¹⁰² A commonly used unit for the spatial frequency is the number of line pairs per millimetre (lp/mm),¹⁰² where one line pair consists of a black and a white line of identical width.¹⁰¹ To determine the MTF, a periodic line grating pattern of cycles with different frequencies is required. Photographs for the NBS 1952 resolution target (resolution target R1L3S10P, Thorlabs Inc., Newton, NJ, USA) used in this study are shown in Figure 12.

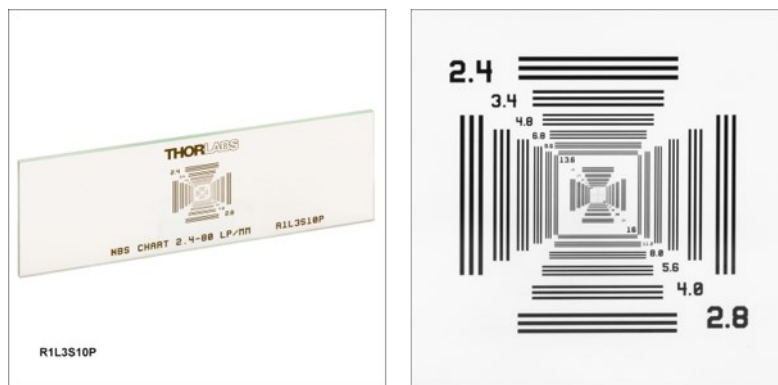


Figure 12 Total picture (left) and close up (right) of the positive NBS 1952 resolution target (https://www.thorlabs.com/newgrouppage9.cfm?objectgroup_id=4338, accessed 24th November 2021). Reproduced with permission from Thorlabs, Inc.

The resolution target comprises 48 sets of lines with 24 different frequencies. Frequencies range from 2.4 lp/mm to 80 lp/mm. One set of lines contains three chrome lines and two glass segments of identical size in between. Thus, spurious resolution is reduced and potential inaccuracy of the resolution measurements is minimised. The manufacturer (Thorlabs Inc.) chose the arrangement of the line sets so that every resolution can be viewed by the movement in one direction (either vertical or horizontal). In the centre of the resolution target are a cross-hair (length and width: 610 μm each) and two concentrically arranged circles with different diameters (250 μm and 500 μm).

Since the resolution target (object) contains pure black (chrome, thickness: 0.12 μm) and white (substrate: clear soda-lime glass) bars, $M_{object} = 1$.¹⁰¹

Consequently, the MTF is equal to M_{image} . The modulation (also contrast) is defined as

$$M(\nu) = \frac{I_{max} - I_{min}}{I_{max} + I_{min}} \quad (13)$$

where I_{max} and I_{min} are the maximum and minimum radiance, respectively.¹⁰¹

Lasch and Naumann¹⁰³ determined the lateral resolution (δx) in infrared microspectroscopy based on this contrast (equation 13 \triangleq equation 2 in ¹⁰³) between two neighbouring structures. Various contrast values are conceivable for the determination of the lateral resolution. Lasch and Naumann set the pertinent threshold value for the contrast $M(\nu_{max})$ to 26.4%.¹⁰³ To calculate δx (unit: μm), equation 14 is used:

$$\delta x = \frac{1000}{2 \cdot \nu_{max}} \quad (14)$$

Equation 13 and equation 14 are also used in this study to quantify the lateral resolution. Further transformation and simplification of equation 13, according to Lasch and Naumann (equation 3 in ¹⁰³ and equation 4 in ¹⁰³), are not feasible due to the present arrangement in the reflection mode instead of a transmission mode.

Although neither chrome nor soda-lime glass produces a Raman signal, the resolution target is suitable to determine the lateral resolution for different fibre diameters. While the soda-lime glass produces, as earlier mentioned, a broad fluorescence signal with a maximum at around 1400 cm^{-1} , the chrome pattern does not produce any fluorescence signal. Consequently, the initial interfering fluorescence signal is useful to calculate the lateral resolution based on the resolutions target's contrast differences. The detected Raman spectra of the soda-lime glass and the chrome pattern are exemplarily shown in Figure 13, using the detection fibre of $100 \mu\text{m}$.

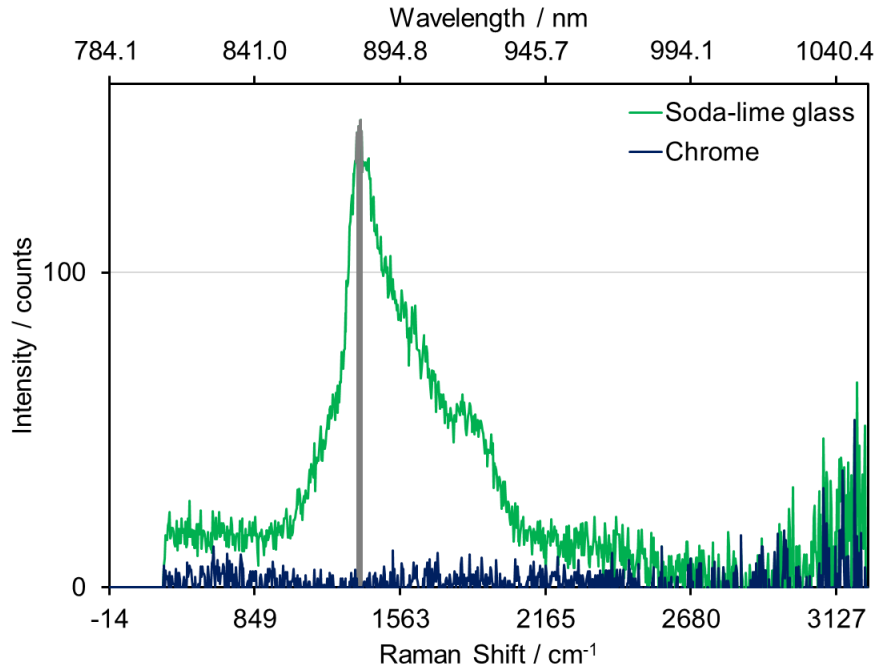


Figure 13 Raman spectra of soda-lime glass (green) and chrome (blue). Setup configuration: Raman spectroscopy, laser power: 50 mW, objective: BD50x, $d_{\text{fibre}} = 100+600 \mu\text{m}$, integration time: 500 ms.

Due to the laser's high heat input at the chrome surface, the laser power is reduced to 50 mW during these experiments to prevent damage to the chrome pattern and a subsequent mismeasurement. The integration time is 500 ms for runs with the 50 μm , 100 μm , and 200 μm fibre. Because of the 600 μm fibre's higher SNR, the integration time is decreased to 200 ms in these runs. As already mentioned, the increase in noise (fluctuations) at higher Raman shifts in Figure 13 is caused by the pixel weighing applying the correction file.

To calculate the lateral resolution at a minor noise impact, the mean value of the intensity signals between 1358 cm^{-1} and 1389 cm^{-1} ($n = 10$, grey area in Figure 13) is evaluated. Thereby, the maximum signals I_{max} originate from the glass substrate, and the minimum signals I_{min} are detected at the chrome pattern. Spectra are only obtained from a lateral scan along the x-axis, assuming that the dimension of the lateral resolution is circular. The step size for spectra collection is set to 5 μm . The chosen step size fulfils the Nyquist-Shannon sampling theorem, which states that the signal sampling rate must be higher than or at least equal to twice the highest frequency to avoid loss of information in the sampled signal.¹⁰⁴ The signal sampling rate corresponds to the reciprocal value of the step size and is 200 mm^{-1} . Factorising the highest frequency of the resolution target (80 lp/mm) by two results in 160 mm^{-1} .

Due to the multimodal imaging system's design, the laser spot is not visible in the camera's photographs when the Raman path is activated. Because of the Raman path's independence, scanning runs are performed at different height positions (z-values) of the stage to determine the minimum lateral resolution. Z-values range from $-15\ \mu\text{m}$ to $+15\ \mu\text{m}$ with $\Delta z = 5\ \mu\text{m}$, where, again, $z = 0\ \mu\text{m}$ refers to the level at which bright-field photographs are obtained in the incident light mode using the BD50x objective. The total travel distance of one run is $2750\ \mu\text{m}$, resulting in 551 Raman spectra at the step size of $5\ \mu\text{m}$. The line sets scanned for the determination of the lateral resolution are the ones with the 12 narrowest lines located around the centre of the resolution target. The spatial frequency increases the closer the line set is to the cross-hair. A segment of the averaged ($1358\ \text{cm}^{-1}$ to $1389\ \text{cm}^{-1}$) intensity value calculated from the six line sets on the right-hand side of the target's cross-hair is shown in Figure 14.

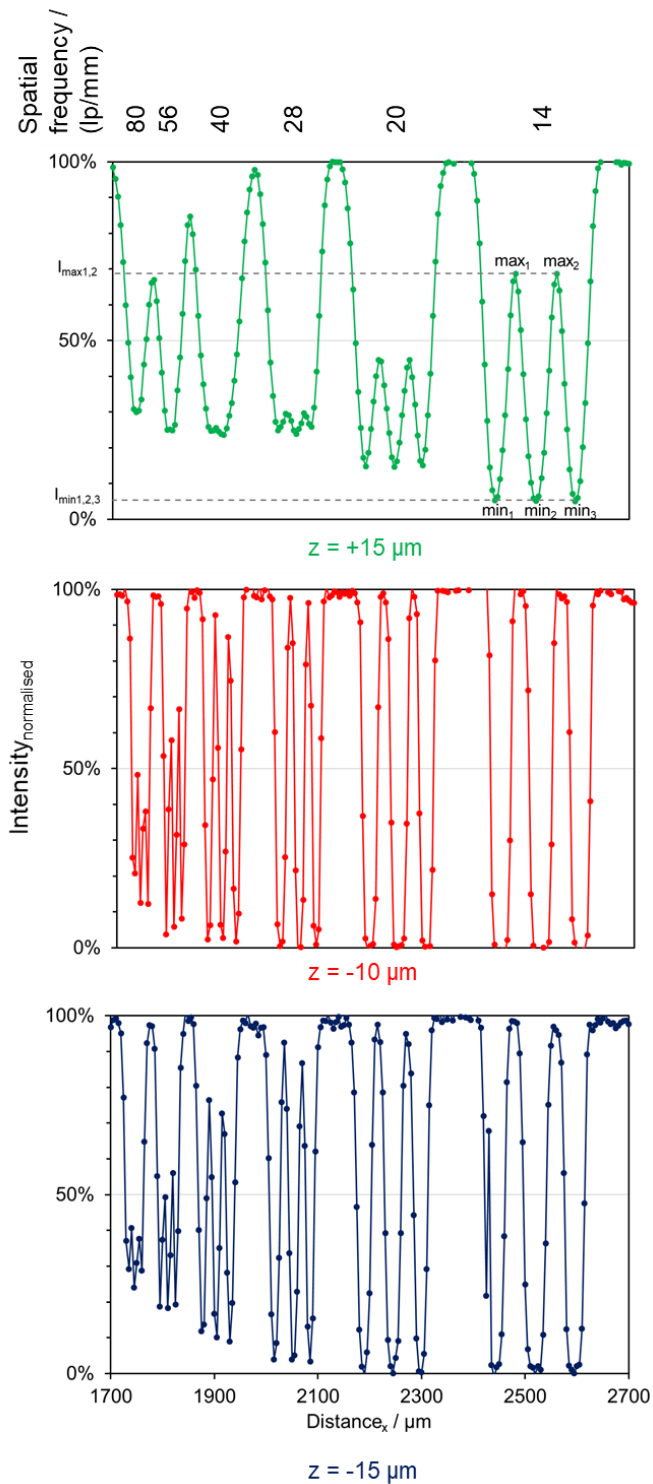


Figure 14 Normalised intensity (mean value: $1358\text{-}1389 \text{ cm}^{-1}$) as a function of travel distance in x-direction at various spatial frequencies and different height positions of the stage: $z = +15 \mu\text{m}$ (green curve), $z = -10 \mu\text{m}$ (red curve), $z = -15 \mu\text{m}$ (blue curve). Setup configuration: Raman spectroscopy, laser power: 50 mW, objective: BD50x, $d_{\text{fibre}} = 100+600 \mu\text{m}$, integration time: 500 ms.

In the figure, the calculated intensity as a function of the travel distance is illustrated for three different z-positions ($+15 \mu\text{m}$, $-10 \mu\text{m}$, $-15 \mu\text{m}$). The intensities are normalised to each scanning run's maximum intensity value ($\cong 100\%$). The intensity values range

from 0% (chrome pattern) to 100% (glass substrate). Values in between indicate that the detected signal originates from an area where signal portions of glass and chrome are recorded.

To calculate the contrast value at a certain spatial frequency, equation 13 is used. Since the resolution target offers three chrome lines (minimum intensities) and two glass lines (maximum intensities) for one set of lines, four contrast values can be determined. The location of the intensities to calculate the contrast for one spatial frequency are shown in an exemplary way in Figure 14 (green curve, grey dashed lines). The determination of the contrast value is only permissible for adjacent intensity extrema (\min_1 and \max_1 , \max_1 and \min_2 , etc.). The final contrast value corresponding to one spatial frequency is determined as the average value of these four contrast values. As can be already seen in Figure 14, the contrast values at height positions of $-10\ \mu\text{m}$ (red curve) and $-15\ \mu\text{m}$ (blue curve) are much higher than the contrast values at a height position of $+15\ \mu\text{m}$ (green curve). Lines at a spatial frequency of 28 lp/mm can be hardly separated at a stage height of $+15\ \mu\text{m}$ and frequencies of 40 lp/mm, 56 lp/mm and 80 lp/mm do not form minima and maxima at all. Another indicator for low contrast and a poor lateral resolution is the intensity rise between the set of lines. This increase in intensity is caused by the broader glass segments between the sets of lines. The size of these segments decreases the smaller the line width. As long as the intensity increases to 100%, the lateral resolution is equal to or smaller than the glass segment.

The lateral resolution at different height positions and different fibre diameters is quantified based on the MTF. An illustration of the calculated contrast values (using equation 13) as a function of the spatial frequency at different z-positions is exemplarily shown in Figure 15.

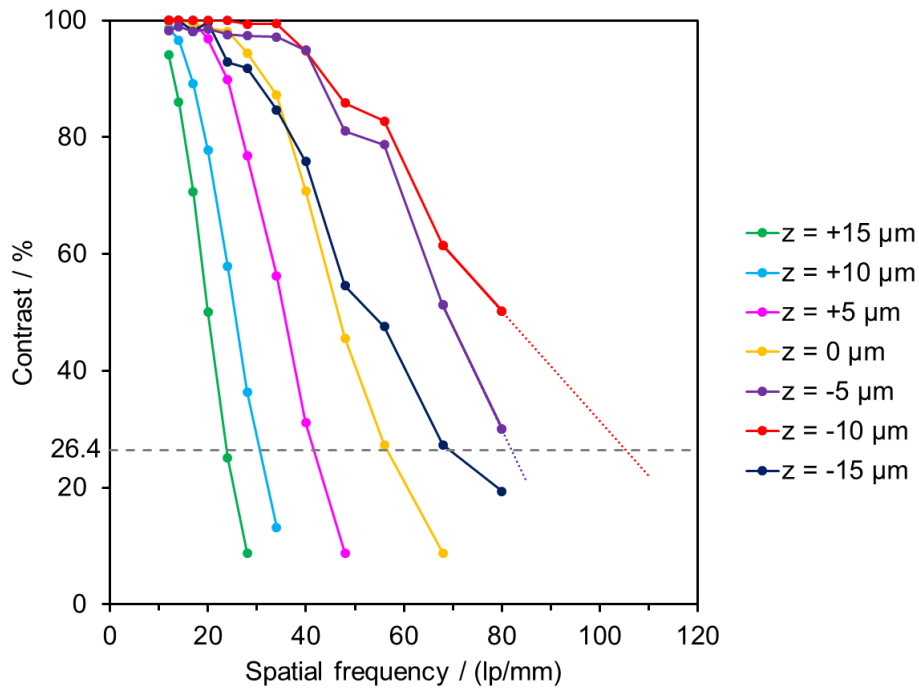


Figure 15 Modulation transfer function (MTF) for the analysis of the NBS 1952 resolution target at various z positions. Setup configuration: Raman spectroscopy, laser power: 50 mW, objective: BD50x, $d_{\text{fibre}} = 100+600 \mu\text{m}$, integration time: 500 ms.

According to Lasch and Naumann,¹⁰³ the lateral resolution is determined at the spatial frequency where the contrast value of 26.4% is reached. This threshold value is marked by the grey dashed line in Figure 15. Experimental data (markers) is connected via straight lines in the figure. At a height position of $-5 \mu\text{m}$ and $-10 \mu\text{m}$, the contrast's threshold value is not reached. Since 80 lp/mm is the highest spatial frequency on the resolution target, data is extrapolated linearly by the extension of the linear trendlines, based on each of the last two measurement values. The spatial frequency at a contrast value of 26.4% is determined from the dataset in Figure 15.

As indicated in Figure 14, the critical contrast value at $z = +15 \mu\text{m}$ is firstly reached. The corresponding spatial frequency is 23.79 lp/mm. The highest spatial frequency is 105.29 lp/mm, which is achieved at a stage level of $-10 \mu\text{m}$.

For the calculation of the lateral resolution, equation 14 is used. The results of all determined lateral resolutions for the respective fibre diameters are shown in Figure 16.

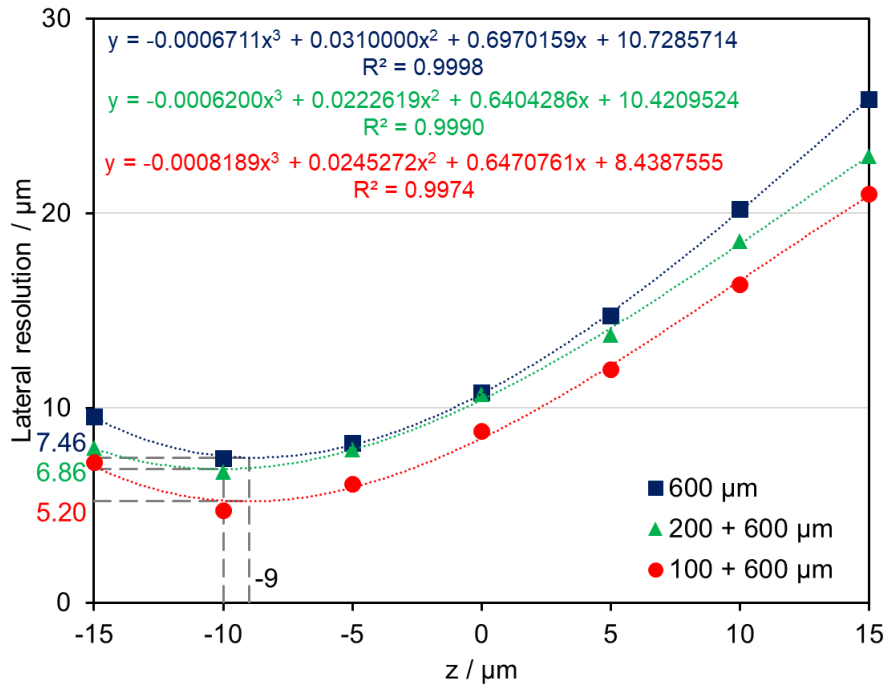


Figure 16 Lateral resolution versus height position of the stage, using different diameters of detection fibre. Markers: experimental data, labelling of the minimum lateral resolution based on the result of a regression (third-degree polynomial equation), Raman shift: 1374 cm^{-1} .

First of all, the evaluation of the fibre with a diameter of $50\text{ }\mu\text{m}$ is not feasible. The reason is the high contrast values of approximately 75% for the maximum spatial frequency of 80 lp/mm at height positions of $-5\text{ }\mu\text{m}$ and $-10\text{ }\mu\text{m}$. Therefore, extrapolation is not acceptable for determining the spatial frequency at the critical contrast value.

The remaining fibres' experimental data (markers) is approximated by third-degree polynomial equations (dotted lines). The asymmetric third-degree polynomial equation instead of a symmetric second-degree polynomial equation is used, considering that Overall et al.⁹⁸ observed deformation of the laser beam due to a mismatch of the refractive indices. The minimum lateral resolutions and the respective height positions are indicated by the dotted lines. Neglecting minor deviation, the z-positions of the smallest lateral resolution is at $-10\text{ }\mu\text{m}$, independent of the fibre diameter. The origin of the z-value of $-10\text{ }\mu\text{m}$ cannot be finally defined. The assumption that the focal plane of the BD50x objective is at $z = 0\text{ }\mu\text{m}$ (focus for the photographs) does not necessarily have to apply to the evaluated wavelength at 880 nm . Although the objective is an apochromatic lens system for compensation of chromatic aberration, the correction might be invalidated for wavelengths in the NIR spectral range. Chromatic aberration describes the effect of the lens's different focal lengths as a function of the wavelength.

Thus, the focal length for red light (long wavelength) is longer than the focal length for short-wavelength blue light.⁹⁷ The negative z-value conforms to a prolongation at 880 nm, one possible consequence of chromatic aberration. Another possibility for the shift of 10 μm in the z-direction might be an imprecision of the physical arrangement of the achromatic lens (Figure 3(c1), (21)) and the pinhole fibre (Figure 3(c1), (19)). The distance between the achromatic lens and pinhole fibre in the detection path is externally adjusted so that the optimal distance of both components results in a parallel beam at a wavelength of 785 nm. In an infinity-corrected microscope, the parallel beam of the detected signal originates from the focal plane of the objective. Minor inaccuracies result in the detection of planes other than the focal plane. The evaluated fluorescence signal is, similar to the Raman signal, an indirect measuring effect based on the emission of light by molecules. Since fluorescence signal is detected with the setup, it can be stated that the detection path coincides with the excitation path.

A further observation that meets the expectations is the decreasing size of the lateral resolution with decreasing fibre diameter. Based on these results, the smallest lateral resolution of 5.20 μm is achieved with the 100 μm fibre. The lateral resolutions of the 200 μm and 600 μm fibre are slightly bigger. These are 6.86 μm and 7.46 μm , respectively.

With respect to the narrow depth profile, resulting in a high ratio of Raman signal and fluorescence interference, a sufficient SNR, and a lateral resolution of approximately 5 μm , the 100 μm fibre is an overall good compromise to perform Raman measurements.

Lateral resolution of VIS/NIR reflectance path

The lateral resolution of the VIS/NIR reflectance path is similarly determined as the lateral resolution of the Raman path. However, the elastically scattered intensity spectrum of the resolution target instead of the inelastic fluorescence signal is evaluated. A further difference regarding the signals is the chrome signal's higher intensity compared to the intensity of the soda-lime glass. While the soda-lime glass reflects the spectral characteristics of the halogen lamp and the optical components in the light path, the reflected intensity spectra of the chrome pattern are characterised by the optical properties of chrome. An example of the chrome's and soda-lime glass' reflected intensity spectra is shown in Figure 17.

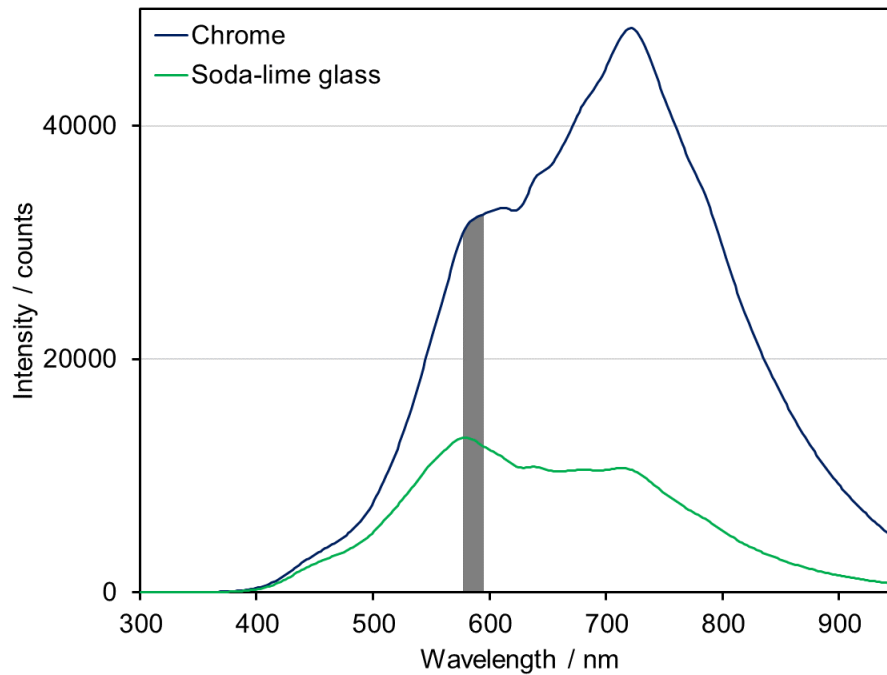


Figure 17 Intensity spectra of chrome (blue) and soda-lime glass (green) in the VIS spectral region. Setup configuration: VIS reflectance spectroscopy, voltage setting of halogen lamp: 12 V, objective: BD50x, $d_{\text{fibre}} = 50+550 \mu\text{m}$, integration time: 100 ms.

The green curve illustrates an intensity spectrum of the soda-lime glass with an intensity maximum at around 580 nm. The intensity maximum in the chrome spectrum (blue curve) is at a wavelength of approximately 720 nm. The change of the spectrum's shape is because of the chrome's spectral properties. The chrome's high extinction coefficients above 650 nm combined with low refractive indices result in high reflectivities (95%-100%, <http://nano-optik.de/produkte/metallisch.html>, accessed 9th December 2021) in the higher wavelength region.

To determine the contrast values, the mean value between 576 nm and 594 nm (in total: 10 values, data interval: 2 nm) is used. Prior to this, an offset value, the minimum intensity signal, is subtracted. This step is mandatory since both the chrome and the glass originate an intensity spectrum in the reflection mode. Without an offset correction, the calculation of the contrast values (using equation 13) is incorrect because a contrast value of 100% (requirement: $I_{\text{min}} = 0$) is never obtained.

The lateral resolution at different height (z) positions of the microscope stage using a pinhole fibre of 50 μm (diameter) is shown in Figure 18.

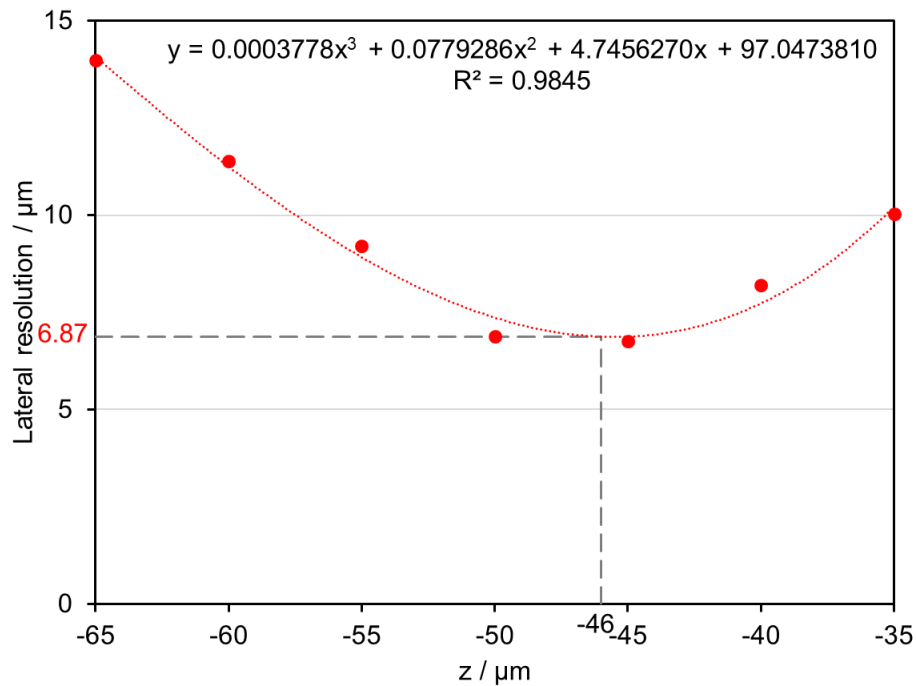


Figure 18 Lateral resolution versus height position of the stage obtained for $d_{\text{fibre}} = 50+550 \mu\text{m}$. Markers: experimental data, labelling of the minimum lateral resolution based on the result of a regression analysis (third-degree polynomial equation), wavelength: 580 nm.

Identical to Figure 16, the experimental data (red dots) is approximated by a third-degree polynomial equation due to the beam deformation. The minimum lateral resolution using the 50 μm fibre is achieved at a height position of -46 μm and results in 6.87 μm . The shift in z-position is most likely because of an additional lens inserted in the tube system for the newly adapted VIS/NIR reflectance path. This lens aims to focus the light onto the 50 μm fibre since the light beam's diameter at the sidewise exit of the photo adapter tube is originally designed for the bigger dimensions of the camera's CCD sensor. Placing the fibre at the camera's position would result in an intensity loss of the detection signal. However, the additional lens leads to the recording of the signal from a plane other than the focal plane. This is caused by the detection of a non-parallel light beam. Consequently, the setup for VIS/NIR reflectance spectroscopy is non-confocal. This is not an issue since the direct measuring effect of VIS/NIR reflectance spectroscopy is based on light absorption.

The identical fibre is also used for the NIR reflectance path. The lateral resolution is determined similar to the VIS reflectance path. Therefore, the mean value between 1400 nm and 1418 nm (in total: 20 values, data interval: 2 nm) is evaluated. The NIR intensity spectra are illustrated in Figure 19.

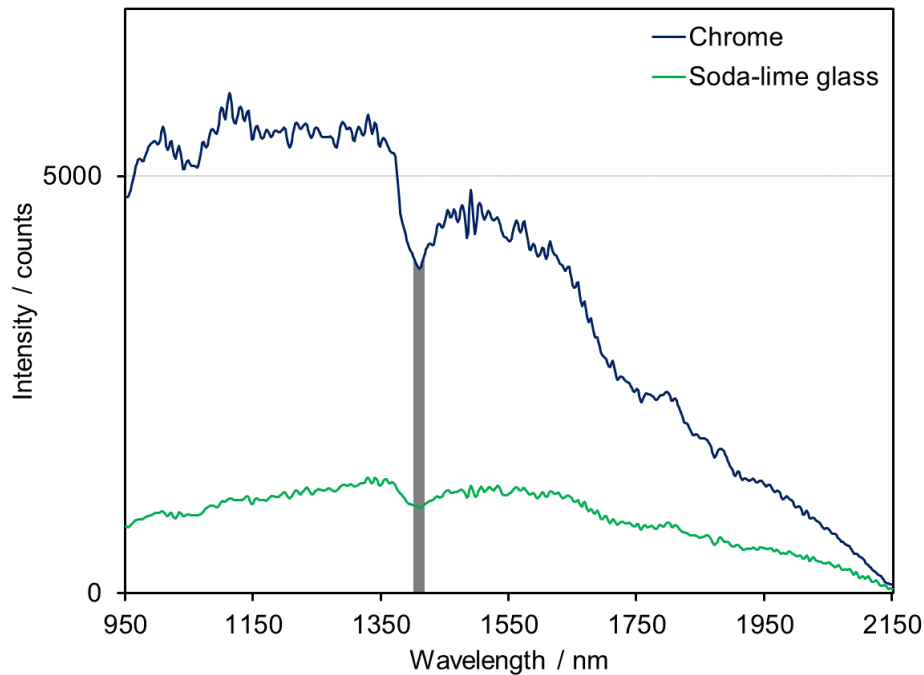


Figure 19 Intensity spectra of chrome (blue) and soda-lime glass (green) in the NIR spectral region. Setup configuration: NIR reflectance spectroscopy, voltage setting of halogen lamp: 12 V, objective: BD50x, $d_{\text{fibre}} = 50+550 \mu\text{m}$, integration time: 200 ms.

In contrast to the intensity spectra in the VIS region (see Figure 17), the NIR intensity spectra show a fixed pattern noise (fluctuation) in the spectra. The noise is the so-called photo response non-uniformity (PRNU). This form of fixed pattern noise is particularly present in extended indium gallium arsenide (InGaAs) detectors such as the detector of the NIR spectrometer. PRNU increases as a function of temperature and integration time (information: Carl Zeiss Spectroscopy GmbH).

However, the NIR spectrometer's maximum integration time (200 ms) and the maximum voltage setting of the halogen lamp (12 V) are required during spectra recording. As indicated in Figure 19, the intensity spectrum of chrome is in the order of 5000 counts and the intensity values of the soda-lime glass are around 1000 counts. This drastic intensity decrease in the NIR spectral region is most likely due to the material and the coating of the optical components in the light microscope. Light microscopes are typically configured for applications in the visible spectral range. A transmission curve of the BD50x objective is not available. The transmission curve of a comparable (information: Leica Microsystems GmbH) objective (#566208, <https://www.leica-microsystems.com/objectivefinder/>, accessed 9th December 2021) shows a decrease in transmission from 87% at 550 nm to 60% at 1000 nm. Transmission data for the NIR spectral region above 1000 nm is not provided. The

transmission is assumed to be lowered in the NIR range since the used objective is not specifically designed for use in the high-wavelength region.

The drop in both intensity spectra around 1400 nm (Figure 19) is identified as the absorption band due to OH vibration modes. These modes originate from the material of the optical fibres (50+550 μm).

As already mentioned, a mean value around this drop is used to determine the lateral resolution of the NIR reflectance path. A figure (Figure 20) illustrating the lateral resolution as a function of the stage position is shown below.

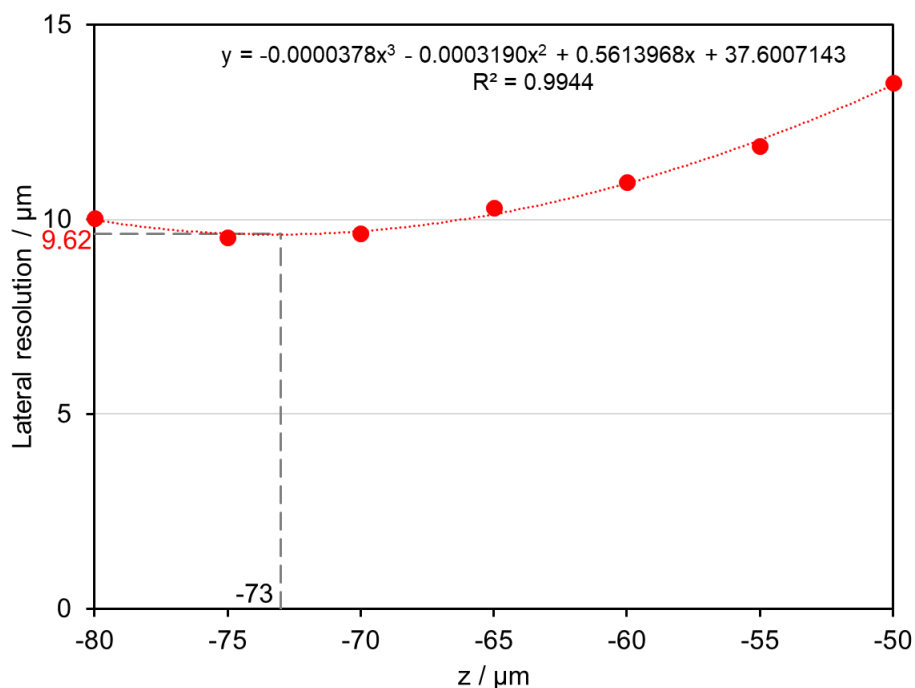


Figure 20 Lateral resolution versus height position of the stage obtained for $d_{\text{fibre}} = 50+550 \mu\text{m}$. Markers: experimental data, labelling of the minimum lateral resolution based on the result of a regression analysis (third-degree polynomial equation), wavelength: 1410 nm.

The minimum lateral resolution of 9.62 μm at -73 μm is bigger than the value for lateral resolution in the VIS spectral region (6.87 μm). This phenomenon can be explained by the diffraction limit, where the diameter of the spot is proportional to the wavelength (λ). The shift of 27 μm in the negative z-direction compared to the VIS path is indicative of chromatic aberration. While the wavelength of approximately 580 nm is used to determine the lateral resolution of the VIS reflectance path, the longer wavelength at 1410 nm is evaluated for the lateral resolution of the NIR reflectance path.

3.1.2 Characteristics of the light sources

The wavelength-dependent intensities reflected from the Zenith Polymer® Diffuse Reflectance Standard (SG 3052, reflectivity $\approx 99\%$, SphereOptics GmbH, Herrsching, Germany) at the halogen lamp's various voltage settings are represented in Figure 21 for the VIS (a) and NIR (b) spectral region.

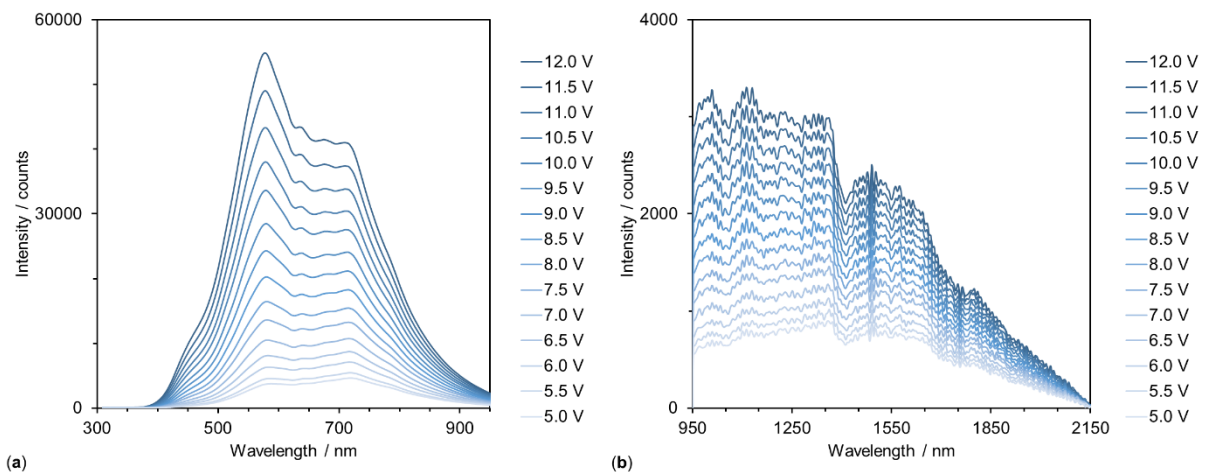


Figure 21 Intensity spectra of the halogen lamp on the diffuse reflectance standard in the (a) VIS and (b) NIR spectral region, using different lamp voltage. Setup configuration: VIS/NIR reflectance spectroscopy, objective: BD50x, $d_{\text{fibre}} = 50+550 \mu\text{m}$, integration time: 100 ms (VIS), 200 ms (NIR).

Both the intensities of the spectra in the VIS and NIR range increase the higher the voltage values. Furthermore, the spectral characteristics in the recorded intensity spectra change. Especially in Figure 21a, it is noticeable that the location of the peak maximum is shifted to shorter wavelengths with increasing voltage values. While the peak maximum is around 730 nm at 5 V, the maximum is shifted to 580 nm at a voltage setting of 12 V. It can be seen from Figure 22 that the lamp's emission power rises at 580 nm stronger than at 730 nm with increases voltage values.

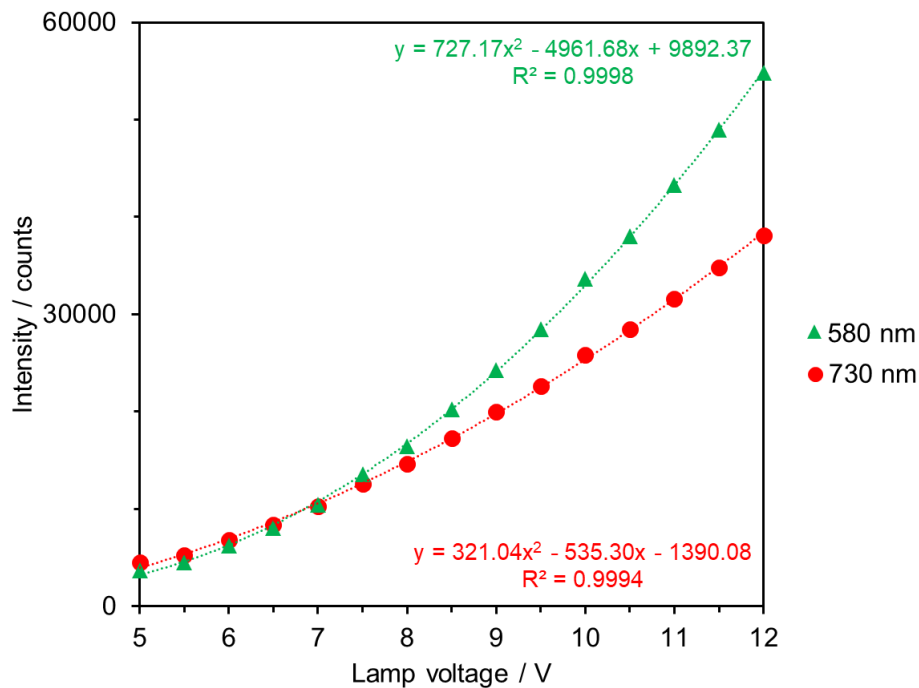


Figure 22 Measured intensities as a function of lamp voltage at 580 nm (green triangles) and 730 nm (red dots).

The figure visualises the signal intensities at 580 nm and 730 nm at different lamp voltages. A good approximation for the trend of both measurement sets is a quadratic polynomial equation. Although both curves are strictly monotonically increasing, the slope of the measurement set at 580 nm is steeper. While the signal intensity at 730 nm is higher at voltage values smaller than 6.5 V, the intensity at 580 nm dominates above 7.5 V. The intersection of the two curves is at 7 V. At this voltage value, the signal intensities are equal at 580 nm and 730 nm.

At a constant resistance of the halogen lamp, the increase of the halogen lamp's voltage setting leads to an increase in the electric current. This electric current passes through the halogen lamp's tungsten filament, which gets heated and starts glowing. The output power (temperature) of the halogen lamp is proportional to the input voltage.¹⁰⁵

Light sources that emit light when heated are referred to as blackbody radiators.¹⁰⁵ By definition, blackbody radiators emit the entirety of the previously absorbed electromagnetic radiation as thermal radiation.¹⁰⁶

Derived from Planck's formula to describe the spectral distribution of the blackbody's thermal radiation dependent on the wavelength,⁷⁹ the wavelength of the power maximum (signal intensity) as a function of the temperature is defined by the so-called Wien's displacement law according to equation 15.¹⁰⁶

$$\lambda_m = \frac{2897.8 \mu\text{m} \cdot \text{K}}{T} \quad (15)$$

where λ_m : wavelength of the power maximum (unit: μm)
 T : temperature (unit: Kelvin)

Although the halogen lamp is not an ideal blackbody radiator, the emission spectrum is close to a blackbody in the visible region.¹⁰⁵

The change in the halogen lamp's spectral characteristic as a function of the voltage setting has to be taken into account to calculate the sample's reflectivity (equation 5) and the absorbance (equation 6). The recording of sample spectra at another voltage setting than the reference spectrum (I_0) falsifies the calculation because the spectral characteristic of the halogen lamp is not fully compensated. This applies to evaluations in the VIS as well as NIR spectral region.

In contrast, the spectral characteristics of the halogen lamp are not affected by the integration time, a further parameter in the measurements. Evidence for this is provided by VIS spectra recorded at a voltage value of 5 V and various integration times of the spectrometer. The results are shown in Figure 23a.

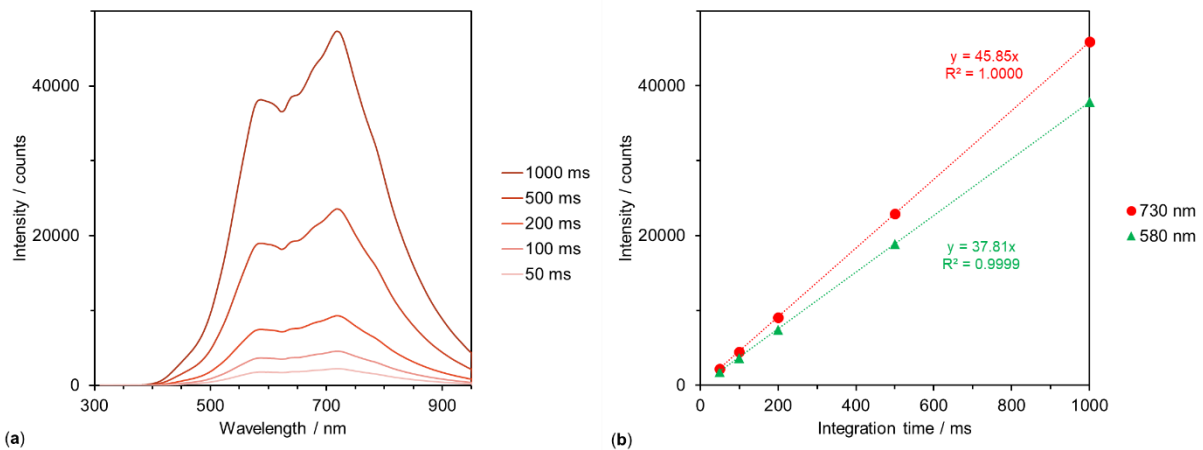


Figure 23 (a) Intensity spectra of the halogen lamp on the diffuse reflectance standard at different integration times and (b) measured intensities as a function of the integration time at 580 nm (green triangles) and 730 nm (red dots); setup configuration: VIS reflectance spectroscopy, objective: BD50x, $d_{\text{fibre}} = 50+550 \mu\text{m}$, lamp voltage: 5 V.

Additionally, the intensity values at 580 nm and 730 nm are plotted versus the integration time (see Figure 23b). Both datasets exhibit a linear approximation. The constant intensity ratios $\left(\frac{I_{730}}{I_{580}}\right)$ verifies the spectra's independence on the integration

time. Furthermore, it can be stated that the intensity signal increases linearly with the integration time.

Raman spectra also increase linearly with the integration time of the spectrometer. A proof is given in Figure 24.

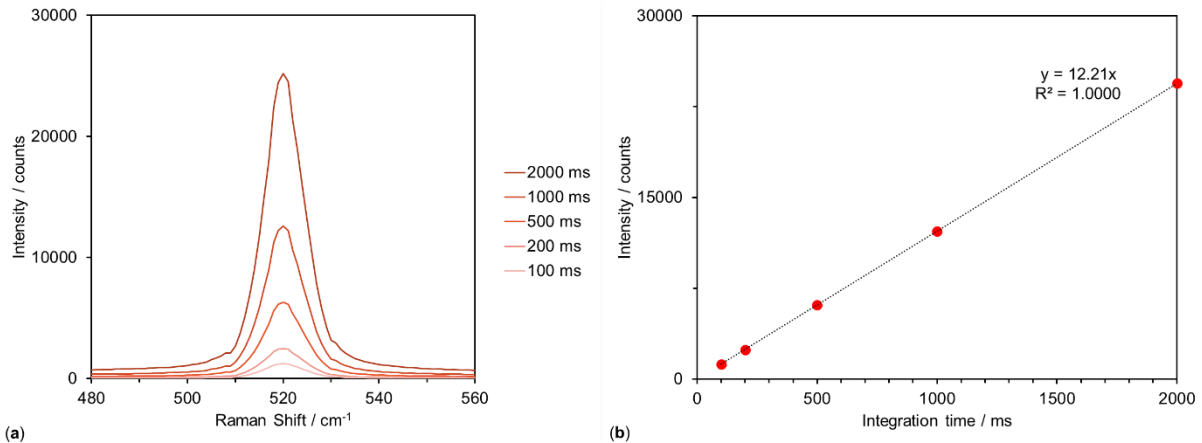


Figure 24 (a) Raman spectra of silicon at different integration times and (b) measured intensities of the peak at 520 cm^{-1} as a function of the integration time; setup configuration: Raman spectroscopy, laser power: 500 mW, objective: BD50x, $d_{\text{fibre}} = 100+600\text{ }\mu\text{m}$.

Figure 24a shows Raman spectra of silicon at different integration times. The laser power is set to 500 mW. The evaluation of the silicon's peak height at 520 cm^{-1} is visualised in Figure 24b. A linear approximation of the measurement data results in a regression coefficient of 1.0000.

Furthermore, the Raman signal increases linearly as a function of the laser power. The results of the evaluation of the silicon peak at a variation in laser power at a constant integration time (2000 ms) are illustrated in Figure 25.

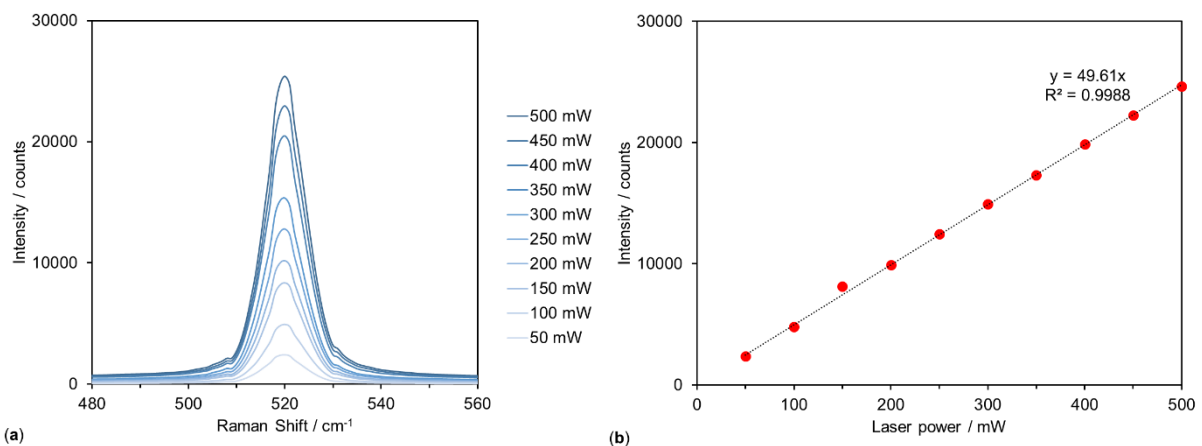


Figure 25 (a) Raman spectra of silicon at various laser powers and (b) measured intensities of the peak at 520 cm^{-1} as a function of the laser power; setup configuration: Raman spectroscopy, objective: BD50x, $d_{\text{fibre}} = 100+600\text{ }\mu\text{m}$, integration time: 2000ms.

Because of the weak Raman effect, it is crucial to maximise the Raman signal while minimising the power losses inside the Raman path.

The Raman signal is maximised by the following configuration of the setup: Removal of all components (reflector, tube lens, beam splitter) in the light microscope's setup that can lead to a beam deformation or an intensity attenuation, and the usage of lenses with wavelength-optimised coating.

The power losses of the laser intensity in the excitation path are determined experimentally. Therefore, the laser power is measured at three different locations of the Raman path. The first position (a) is at the exit of the 100 μm excitation fibre (Figure 3(c1), (10)) before connecting to the initial Raman setup. The second set of measurements (b) determines the laser power of the collimated excitation beam before entering the objective. For this purpose, the microscope's objective is removed from the sextuple nosepiece (Figure 3c (8)) and the photodiode power sensor (S130VC + PM100USB, Thorlabs Inc., Newton, NJ, USA) to measure the laser power is placed on the microscope stage. The third location (c) is in the object plane, underneath the BD50x objective. Thereby, the measuring device is placed on the stage as well. Per set of measurements, the power is recorded at ten different power settings ($\Delta P = 50 \text{ mW}$) ranging from 50 mW to 500 mW. Since the maximum measurement range of the sensor is restricted to 5 mW, a neutral density filter (NE30B, Thorlabs Inc., Newton, NJ, USA) is placed on the sensor for power attenuation. The filter's transmittance at a wavelength of 785 nm is experimentally ($n = 3$) determined and results in 0.98%. Consequently, the laser's maximum power of 500 mW is reduced to 4.9 mW, which does not exceed the measurement range (0-5 mW) of the photodiode in the power sensor.

Each measuring interval has a duration of 100 s and contains 100 measurement values. The mean value of the measured laser power versus the set (via the software) laser power is plotted. An illustration of the data is shown in Figure 26.

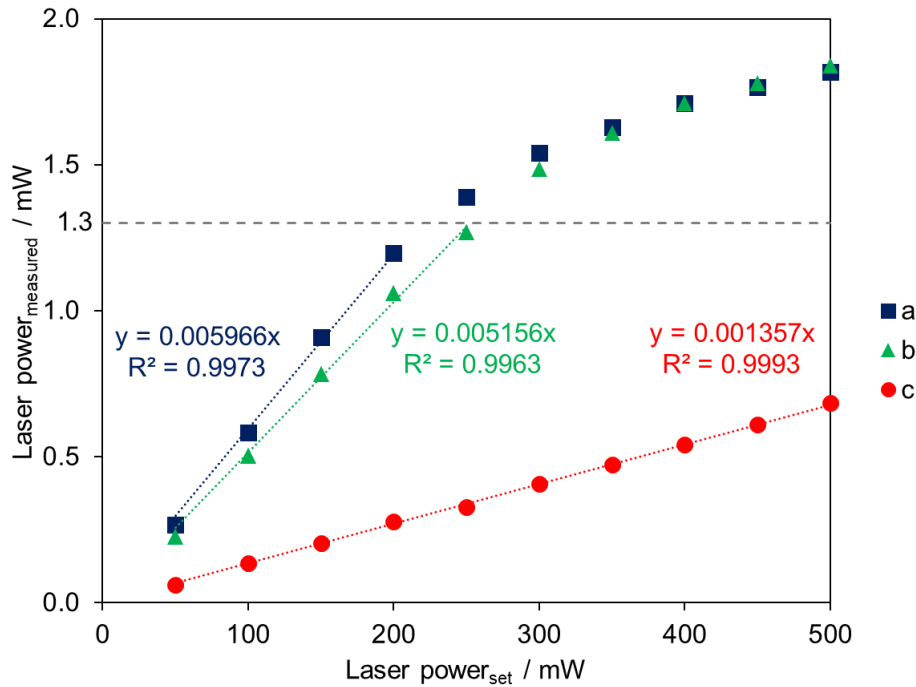


Figure 26 Measured laser power (with attenuation filter) versus laser power set at the laser module (a) at the exit of the excitation fibre, (b) of the collimated laser beam before entering the objective, (c) in the object plane after transmitting the objective; dashed horizontal line: saturation of detector response.

Each curve represents a specific measurement set (location). The markers are the experimental data. For the measured data at the measurement location (a) (fibre exit) and (b) (collimated beam), a saturation of the detector response at higher laser powers is recognised. Therefore, the threshold value is set to 1.3 mW. Only measurement values below that threshold value are considered to determine the linear regression line. The regression line for the measured power values at location (c) (object plane) is determined based on the entire measurement set. This is feasible because the detected laser power at 500 mW (maximum value) is 0.68 mW, which is below the threshold value of 1.3 mW.

To calculate the actual laser power in the object plane, the measured value of 0.68 mW is multiplied with the reciprocal of the neutral density filter's transmission value (0.98%). This results in a laser power of 69.4 mW at the maximum set laser power (500 mW). Consequently, 86.1% of the laser power is lost compared to the set laser power. A portion of the laser power (~40%) is already lost due to the coupling of the laser light onto the excitation fibre and inside the excitation fibre (location: (a)). Thus, the maximum achievable power in the focal plane is 304.4 mW. The laser power of 304.4 mW is the mathematical product of the blue regression line's slope (0.005966) and the maximum power (500 mW) divided by the transmission value (0.98%) of the

neutral density filter. In addition, there are intensity losses in the excitation path due to the lens (Figure 3(c1), (11)), the bandpass filter (Figure 3(c1), (12)), the dielectric mirror (Figure 3(c1), (13), and the beamsplitter (Figure 3(c1), (14)). To determine these losses, the laser power at location (b) is taken into account. Therefore, the green regression line's slope (0.005156) is multiplied by 500 mW (maximum power) and the reciprocal value of the density filter's transmission (0.98%). The calculation results in 263.1 mW. Compared to 304.4 mW (location (a)), 13.6% is lost inside the adapted Raman setup. Most of the power, approximately 74%, is lost at the microscope's objective (location (b): 263.1 mW) versus location (c): 69.4 mW)). The intensity loss at the objective might originate from three different reasons. First, a low transmittance for wavelengths above 785 nm is due to the objective's design for use with a conventional light microscope in the visible range. Second, reflections at the air-glass interface inside the objective. Depending on whether the optical components are coated with an anti-reflection coating, the reflection increases from 0.1% or 1.0% for a multiple-layer coating or a single-layer coating, respectively, to 4% for uncoated optics.¹⁰⁷ Microscope objectives consist of up to 20 single lenses.⁹³ Already five lenses (10 surfaces) reduce the incident light intensity from 100% to 66%. Since no data regarding the microscope objective's specification is available, a quantification of the intensity loss caused by the two mentioned effects is infeasible.

The third issue that is taken into account is the diameter of the collimated laser beam entering the objective. For the present case, the diameter is defined as the FWHM value of the beam's intensity distribution. The intensity distribution is determined by moving the power sensor (S130VC + PM100USB, Thorlabs Inc., Newton, NJ, USA) along the lateral axis ($\Delta x = 0.2$ mm, $\Delta y = 1.0$ mm) of the microscope stage. During the experiments, the original sensor area (9.5 mm) is reduced to 2 mm by an iris diaphragm (D36S, Thorlabs Inc., Newton, NJ, US). An iris diameter of 2 mm fulfils the requirements to receive a sufficient lateral resolution of the intensity distribution and an overlap (no undersampling) of measurement data for increments of 1 mm (Δy). Furthermore, a neutral density filter (NE20B, Thorlabs Inc., Newton, NJ, USA) is placed on the sensor for power attenuation of the initial laser power (500 mW).

A surface plot of the collimated laser beam's intensity distribution is shown in Figure 27.

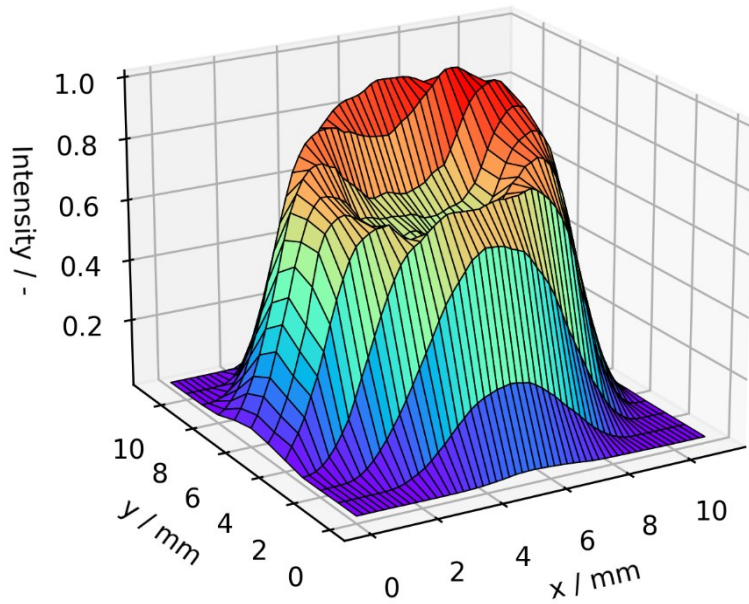


Figure 27 Surface plot of the intensity distribution of the collimated laser beam before entering the objective; lens: LA1951-B (Thorlabs Inc., Newton, NJ, USA).

The resulting FWHM value of 8.3 mm is in good accordance with the result of the manufacturer’s (Thorlabs Inc.) simulation (7 mm). However, the shape of the distribution differs from the expected Gaussian distribution with the global maximum in the centre. The centre of the current distribution is characterised by an indentation. In the core of step-index multimode fibres, there are two ray paths: a zig-zag path of meridional rays and a helical path of skew rays.¹⁰⁸ In contrast to meridional rays, which cross the fibre axis, skew rays never cross the fibre axis.¹⁰⁸ Experimental data of Thorlabs Inc. (see Figure 28) shows that the distribution of the laser beam at the fibre’s exit is Gaussian distributed for an input angle of 0°, where all rays are meridional rays.

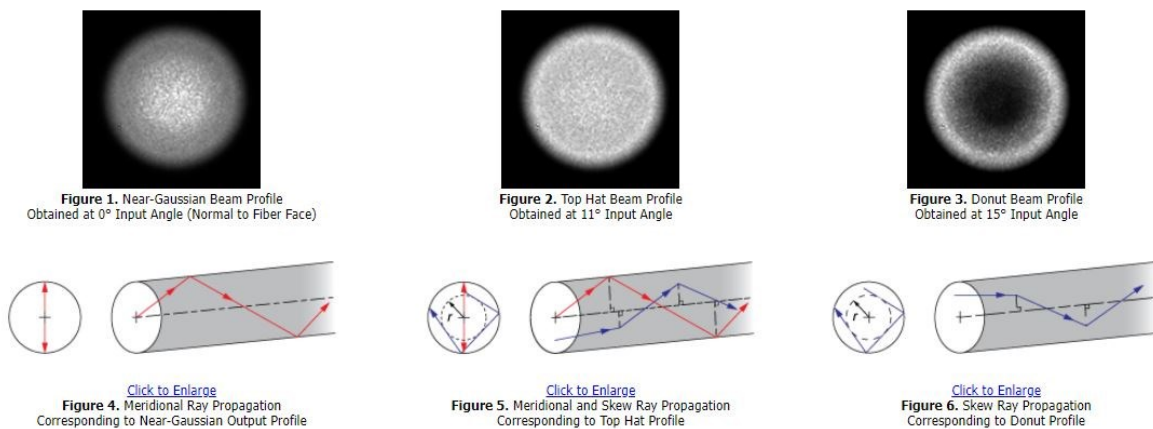


Figure 28 Beam profiles (Figure 1-3) and ray propagation of laser light (Figure 4-6) in a step-index multimode fibre at different input angles (https://www.thorlabs.com/newgrouppage9.cfm?objectgroup_id=11993, accessed 12th January 2022). Reproduced with permission from Thorlabs, Inc.

The portion of skew rays increases with increasing input angles. An input angle of already 11° results in a so-called top-hat profile and an angle of 15° modifies the output beam profile to a doughnut profile.

To determine the reason for the laser beam profile's deviation from the ideal transverse electromagnetic (TEM) mode TEM_{00} (Gaussian profile), a dual scanning slit beam profiler (BP209-VIS/M Thorlabs Inc., Newton, NJ, US) is used to record the beam profile at the exit of the $100\ \mu\text{m}$ (diameter) excitation fibre. Figure 29 visualises the 2d (a) and 3d (b) intensity profile qualitatively.

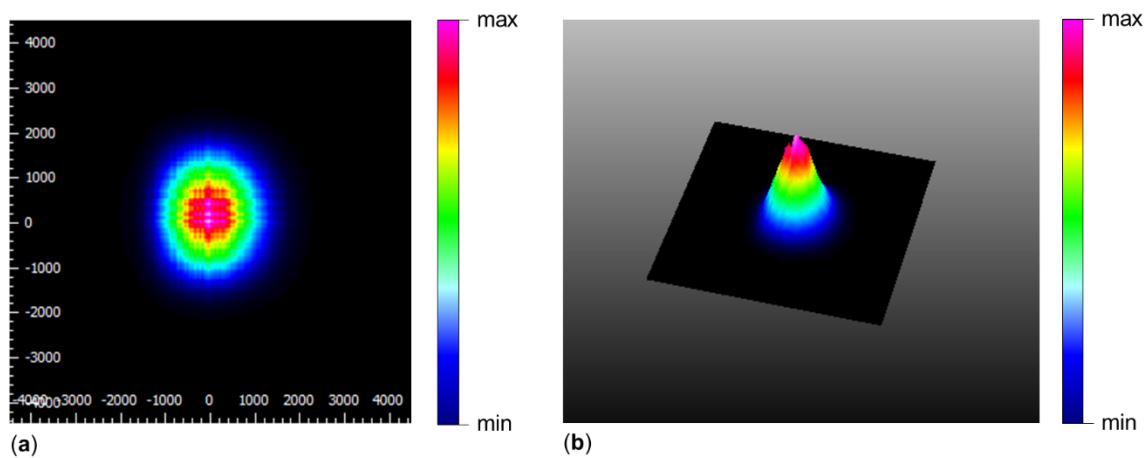


Figure 29 Qualitative (a) 2d intensity distribution and (b) 3d intensity distribution of the laser beam at the fibre exit of the $100\ \mu\text{m}$ excitation fibre (Figure 3(c1), (10)); measurement device: BP209-VIS/M Thorlabs Inc., Newton, NJ, US. Note: The beam deformation (expected: circular) might result from a misaligned arrangement of the fibre and the sensor.

The beam distribution results of the fibre's output beam in this study is Gaussian distributed.

The consultation with the lens' manufacturer (Thorlabs Inc.) confirmed that the deformed beam distribution results from spherical aberration caused by the plano-convex lens's suboptimal surface quality.

The spherical aberration is eliminated and a Gaussian beam profile is achieved with a high-quality collimator (F220FC-780, Thorlabs Inc., Newton, NJ, USA). The corresponding surface plot of the collimated laser beam, recorded under identical conditions as the surface plot of the collimated beam using the plano-convex lens, is illustrated in Figure 30.

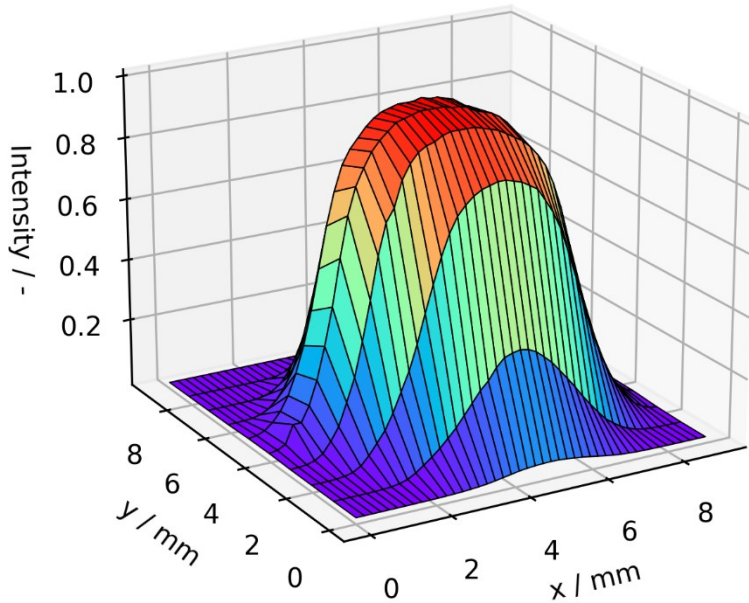


Figure 30 Surface plot of the intensity distribution of the collimated laser beam before entering the objective; fibre collimator: F220FC-780 (Thorlabs Inc., Newton, NJ, USA).

The FWHM value of this intensity distribution is 5.5 mm. Since this diameter does not overfill the objective's pupil lens (6.8 mm), which is a criterion to generate a diffraction-limited focal spot, the plano-convex lens is not replaced by the collimator.

3.1.3 Determination of the photograph's field of view

The resolution of the microscopic modalities is restricted by the so-called diffraction limit, which depends primarily on the NA of the selected microscope objective. One approach describing the diffraction-limited resolution of light microscopes is the so-called Rayleigh criterion. This criterion states that the diffraction limit of two objects is reached when their distance (d_R) is so close that the maximum of one Airy pattern is above the first minimum of the other Airy pattern. An Airy pattern is rotationally symmetric and describes the intensity distribution in the focal plane.

This distance (d_R) between two adjacent objects is determined based on equation 16:

$$d_R = \frac{0.61 \cdot \lambda}{n \cdot \sin \alpha} \quad (16)$$

where λ : wavelength (unit: nm)
 $n \cdot \sin\alpha$: numerical aperture (NA)

Since the human eye's maximum sensitivity is at 550 nm, this wavelength is often used as the representative wavelength to calculate the diffraction-limited resolution.⁵⁶

A parameter of interest for the scanning experiments is the photograph's field of view. The Grid/Collection stitching⁸⁰ used to stitch the single photographs to an entire image has a default value for the tile overlap of 20%. Consequently, the step sizes during the scanning experiments are approximately 20% of the photograph's field of view. In advance, the photograph's field of view is calculated with the aid of a calibration slide (LIM Calibration Slide, Laboratory Imaging Ltd.). Therefore, the length (number of pixels) of the reference scale within a photograph is measured ($n = 11$) using Fiji. The quantified length (average value) and the physical length on the calibration slide enable the calculation of the pixel size. The size of the photograph's field of view results from the multiplication of the pixel size with the camera sensor's dimensions (1280 x 960 pixels). The corresponding photographs' field of view, pixel size, step size, and diffraction limit are subsequently shown (Table 3) for various objectives. These parameters are independent of the light mode (incident or transmitted light).

Table 3 Diffraction limit, pixel size, field of view and step size of various microscope objectives

Microscope objective	Diffraction limit	Pixel size x y	Photograph's field of view	Step size x y
5x (NA: 0.12)	2.80 μm	0.6935 μm 0.6935 μm	887.73 μm x 665.80 μm	720 μm 540 μm
BD20x (NA:0.50)	0.67 μm	0.1748 μm 0.1748 μm	223.74 μm x 167.80 μm	180 μm 135 μm
BD50x (NA:0.85)	0.39 μm	0.0689 μm 0.0689 μm	88.22 μm x 66.16 μm	72 μm 54 μm

The 5x and the BD20x objectives are used for data acquisition with the microscopic modalities. Knowledge about the pixel size at a magnification of 50x is essential for the subsequent experiment to determine the microscope stage's accuracy.

3.1.4 Accuracy of the microscope stage

A further parameter that is taken into account is the accuracy of the microscope stage. The lateral resolution of approximately $5\ \mu\text{m}$ for the spectroscopic modalities requires an equal step size for data acquisition without loss of information. The stage's accuracy is determined based on a spot's displacement (Δ) when moving the stage in increments of $5\ \mu\text{m}$. The spot is located on the calibration slide (LIM Calibration Slide, Laboratory Imaging Ltd.). The evaluated data are bright-field photographs recorded in the incident light mode at a magnification of 50x. Thereby, a displacement of $5\ \mu\text{m}$ corresponds to 72.57 pixels. Due to the photograph's field of view ($88.22\ \mu\text{m} \times 66.16\ \mu\text{m}$), the spot's maximum number of displacements in the x and y direction are 17 and 13, respectively. Consequently, the object of interest (spot) varies randomly in the experiments. For each lateral axis (x and y), two runs of experiments are carried out. The first run consists of 100 images at a travel range of $495\ \mu\text{m}$. The second run starts $150\ \mu\text{m}$ before the first run and covers a travel range of $645\ \mu\text{m}$. The graphical evaluation of the microscope stage's accuracy is illustrated in Figure 31.

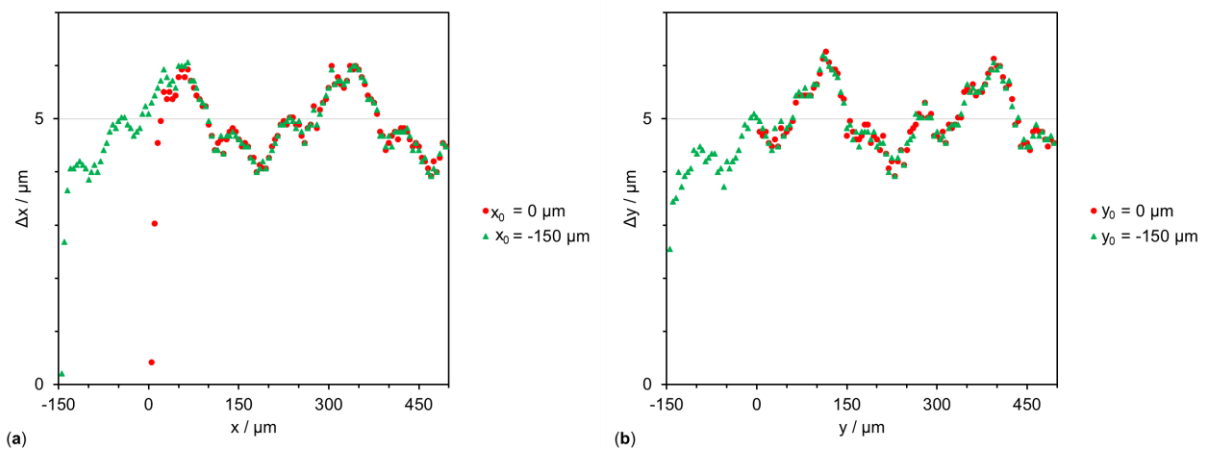


Figure 31 The artefacts' displacement as a function of travel range in the (a) horizontal direction at different starting positions $x_0 = 0\ \mu\text{m}$ (red dots) and $x_0 = -150\ \mu\text{m}$ (green triangles) and (b) vertical direction at different starting positions $x_0 = 0\ \mu\text{m}$ (red dots) and $x_0 = -150\ \mu\text{m}$ (green triangles).

The diagrams for the (a) horizontal and (b) vertical axis show a characteristic pattern that is reproducible at different starting positions. This pattern originates from errors caused by manufacturing inaccuracies of the stage's mechanical components. The first three lower displacement values of the runs indicate the motor's slip at the drive when changing direction. Since the run at $y_0 = 0\ \mu\text{m}$ is started without a change in the scanning direction, no motor slip occurred. To minimise this mechanical effect for data

acquisition from two-dimensional areas, the scanning pattern of the microscope stage is row-by-row from left to right and up to down.

The mean value of the stage's displacement in both directions is calculated using the data obtained from the longer travel ranges (green curves), excluding the first three data points. This results in displacement values for the x-axis and the y-axis of $4.89 \pm 0.60 \mu\text{m}$ and $4.88 \pm 0.58 \mu\text{m}$, respectively. Since only integer values exist for the displacement in pixel numbers, a displacement of $5 \mu\text{m}$ ($\cong 72.57$ pixels at a pixel size of $0.0689 \mu\text{m}$) varies between $4.96 \mu\text{m}$ and $5.03 \mu\text{m}$ in any case. Due to the slight deviation with the two runs in one direction (red versus green curve), errors caused by the manual determination of the displacement value within the photographs have an insignificant effect on the determined accuracy. Furthermore, the minor tilt of the camera is negligible for the determinations. Altogether, the stepper motor has an accuracy below $\pm 0.6 \mu\text{m}$ in both directions. However, data obtained from the first three upper rows and the first three left columns is excluded from the evaluation due to the mentioned slip of the motors. The unidirectional repeatability is smaller than $5 \mu\text{m}$, according to the manufacturer (Märzhäuser Wetzlar GmbH).

3.1.5 Signal stability of the multimodal imaging system

To determine the overall signal stability during the measurements, long-term experiments are carried out recording spectra of the Zenith Polymer[®] standard (for VIS/NIR reflectance spectroscopy) and the silicon wafer (for Raman spectroscopy) in intervals of one minute for a total measurement time of six hours. For data evaluation, the peak intensity of a characteristic peak in each spectrum is calculated and plotted versus time. The results are shown in Figure 32.

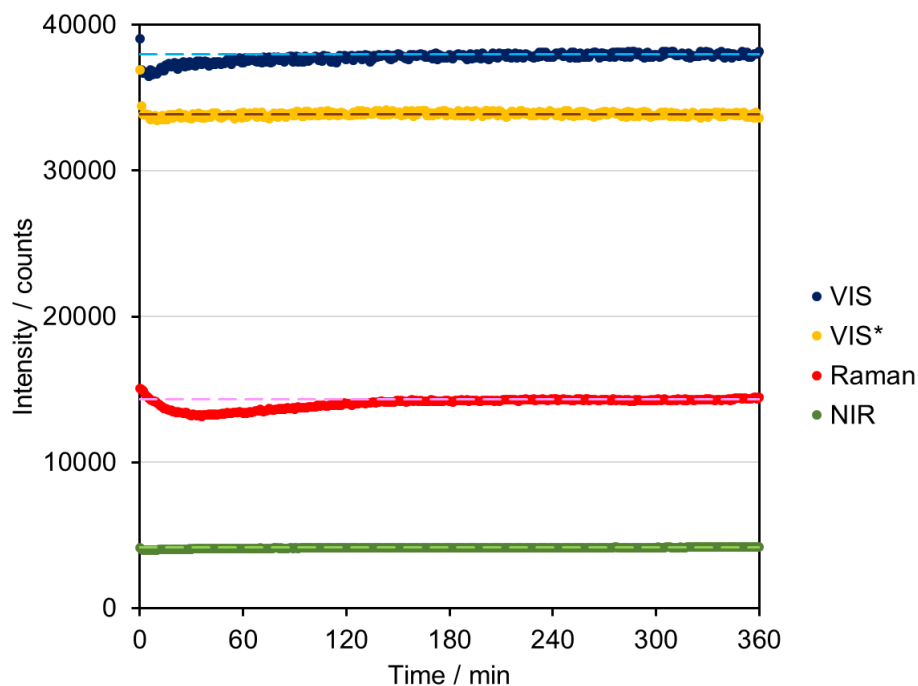


Figure 32 Signal intensity at certain spectral ranges for each modality over time (see text for details).

The red curve visualises the signal intensity of the silicon peak in the Raman spectrum at 520 cm^{-1} minus an offset value (average value from $480\text{--}489\text{ cm}^{-1}$ and $550\text{--}559\text{ cm}^{-1}$). The green curve shows the temporal course of the mean value between 1400 nm and 1418 nm of the NIR intensity spectrum. The orange and the blue curves illustrate the mean value from 576 nm to 594 nm in the VIS intensity spectrum. Variations in signal intensities result from time-dependent characteristics of the light source (halogen lamp or laser) and the detector (VIS, NIR, and Raman spectrometer). Therefore, the light source and the detector are switched on at $t = 0\text{ min}$ with one exception. Spectra acquisition of the orange curve (VIS*) is started 30 min after switching on the VIS spectrometer. This measurement aims to determine the halogen lamp's temporal trend since the halogen lamp is also used for taking photographs. The dashed lines indicate the average of the last sixty measurement values (last hour), assuming that stable signal intensities are reached within this duration.

After starting the experiment, the intensity of the red dataset (Raman path) decreases within the first 30 min. Afterwards, the intensity increases slowly and remains constant after 150 min. The total measurement time for a Raman scan of 2500 single spectra at an integration time of 4 s per pixel takes nearly 3 h. Excluding a heating period of 30 min, the standard deviation of the 180 adjacent (3 h) data values is less than 350. This corresponds to a relative standard deviation of 2.5%. Since the evaluation of the Raman spectra is based on peak ratios instead of absolute peak intensities, variations

of the detected Raman spectra, mainly caused by variations in laser intensity, are eliminated. Nevertheless, a heating period of 30 min is advised. For evaluating absolute peak intensities to determine concentrations, a heating period of 60 min is recommended. This reduces the relative standard deviation to 1.9%, which is below the maximum advised power fluctuations of 2% for accurate and comparable measurements.³²

The intensities for VIS, VIS*, and NIR in Figure 32 (for NIR not legible due to the y axis scaling) have a maximum intensity at $t = 0$ min. This maximum value is caused by the halogen lamp's minor resistance due to the tungsten filament's low temperature when turning the light on. Since the subsequent decrease is higher in the VIS dataset than in the VIS*, after the VIS spectrometer's heating period of 30 min, the drop is mainly a characteristic of the VIS spectrometer. The green curve (NIR path) shows a similar trend to the blue curve (VIS) path. Since the VIS and NIR spectrometers are assembled in one rack with one power supply, a warm-up period of 20 min is recommended. Compared to data acquisition with Raman spectroscopy, shorter integration times in the order of 100 ms and 200 ms are sufficient to record VIS and NIR spectra. Within 30 min after the heating period, the standard deviation of the VIS and NIR intensity values is only 0.4% each.

The halogen lamp (orange curve) reaches constant intensity values after 2 min.

3.1.6 Workflow and setup parameters during scanning experiments

The first application of the developed multimodal imaging system for tissue analysis consists of two measurement sets (global and local) to distinguish between GM and WM of mouse brain tissue. The global scan aims to record the whole sample with grid sizes of 200 μm in both lateral directions for the spectroscopic modalities. Afterwards, a local scan with a higher spatial resolution (step size: 5 μm) of the hyperspectral data is carried out. The local scan is performed at a designated region of interest (ROI). This smaller area is on one tissue section with a boundary of grey matter (GM) (cortex) and white matter (WM) (corpus callosum). The step size to record the photographs with the microscopic modalities results from the determination of the photograph's field of view (chapter 3.1.3). It remains constant for the global and the local run. Each set of measurements includes several scanning runs that are performed sequentially.

The halogen lamp's fast warm-up time is one reason why data acquisition with the developed multimodal imaging system starts with the microscopic modalities. Measurements of the thawed unstained tissue section are carried out at room temperature without using an immersion medium between the sample surface and the microscope objective. Prior to one set of measurements, a white balance to adjust the camera's three (red, green, blue) colour channels is carried out in the incident light bright-field mode using the 5x objective. The reference target is the Zenith Polymer[®] standard. The voltage value is 5 V, and the camera's integration time is 100 ms.

The voltage value and the integration time for the subsequent data acquisition with the microscopic modalities are chosen so that neither an underexposure nor an overexposure of the photographs is recognised. The exact values are shown in the figure captions of the stitched tissue photographs at a later stage. The created workflow, based on the results obtained from the experiments for further characterisation of the multimodal imaging system, is provided in Table 4.

Table 4 Workflow and setup parameters of one set of measurements of tissue analysis with the multimodal imaging system. Modified from ¹

Scan No.	Modality	Light source	Microscope objective	Step size x y	Reflector	Tube lens	Further components	Detector device	Tissue sample
1	Incident light bright-field microscopy	Halogen lamp	5x	720 μm 540 μm	BF reflector	1.25x	–	Camera	
2	Incident light bright-field microscopy	Halogen lamp	BD20x	180 μm 135 μm	BF reflector	1.25x	–	Camera	
3	Incident light dark-field microscopy	Halogen lamp	BD20x	180 μm 135 μm	DF reflector	1.25x	–	Camera	
4	Incident light polarisation microscopy	Halogen lamp	BD20x	180 μm 135 μm	Smith reflector	1.25x	Polariser & analyser (WWC deactivated)	Camera	Unstained sample on a gold-coated slide
5	Incident light polarisation microscopy (with WWC)	Halogen lamp	BD20x	180 μm 135 μm	Smith reflector	1.25x	Polariser & analyser (WWC activated)	Camera	
6	Raman spectroscopy	Laser	BD50x	200 μm 200 μm ⁱ 5 μm 5 μm ⁱⁱ	–	–	100+600 μm fibre	Raman spectrometer	
*	Incident light bright-field microscopy	Halogen lamp	BD20x	180 μm 135 μm	BF reflector	1.25x	–	Camera	
7	VIS spectroscopy	Halogen lamp	BD50x	200 μm 200 μm ⁱ 5 μm 5 μm ⁱⁱ	BF reflector	1.25x	50+550 μm fibre	VIS spectrometer	
8	NIR spectroscopy	Halogen lamp	BD50x	200 μm 200 μm ⁱ 5 μm 5 μm ⁱⁱ	BF reflector	1.25x	50+550 μm fibre	NIR spectrometer	
9	Transmitted light microscopy	Halogen lamp	5x	720 μm 540 μm	BF reflector	1.25x	–	Camera	H&E-stained sample on a glass slide

ⁱ global scan, ⁱⁱ local scan, * additional scan that does not contribute further local tissue information

Table 4 provides an overview of the system components like the reflector, the tube lens, and the detector to configure the corresponding light path.

Data acquisition starts with the incident light bright-field mode using the 5x objective. This configuration enables the recording of widespread areas in short times due to one photograph's large field of view. The starting position for the entire set of measurements is allocated via the manual orientation with the SmartMove control element (Figure 2, (17)).

The second scan is also performed with the incident light bright-field mode, using higher magnification. Besides recording bright-field photographs, the design of the BD20x objective enables performing dark-field microscopy (scan no. 3). The same objective is also used for polarisation microscopy with (scan no. 5) and without (scan no. 4) contrast enhancement by the whole-wave compensator (WWC). Consequently, scan no. 2-5 comprise data acquisition of all microscopic modalities at the same resolution.

The next modality is Raman spectroscopy (scan no. 6). Since the Raman path is an independent light path because of the activation of the tilted mirror in the interchangeable photo adapter tube (Figure 2, (7)) to perform the microscopic modalities, the MultiSpec[®] Raman System is heated up while taking certain photographs. The z-value to perform the Raman measurements is recommended at the stage's height position where the strongest Raman signal comes from. For dry objectives, the maximum signal originates when the focus is just below the surface since this is the position where the instrument's depth of field is roughly filled with the sample.⁹⁸ In the present study, this height position is at -6 μm (data not shown). The divergence to -10 μm (the result of lateral resolution) is due to the focus's immersion and the different refractive indices. Soda-lime glass has a refractive index of 1.46. Sun et al.¹⁰⁹ determined a refractive index of WM (corpus callosum) at 1.41. The refractive index of GM (cortex) was 1.37. The tissue's smaller RI compared to the soda-lime glass results in a minor prolongation of the laser beam and consequently a higher (more positive) z-position of the stage.

The difference in refractive indices between WM and GM is 0.04. This can result in different Raman signal intensities depending on the tissue type. However, peak ratios, which are calculated to distinguish GM and WM, are unaffected by a variation in the refractive index.

With respect to the weak Raman effect, it is intended to perform Raman measurements at the maximum laser power to minimise the integration time per pixel and the total measurement time. Prior to that, the dark spectrum has to be recorded a single time with the laser switched off to detect intensity (net) spectra. Since the laser power might alter or destroy the tissue, an additional scan (scan no. *) is recommended. This scan does not contribute further local tissue information. However, it is a good indicator to determine the tissue condition after Raman measurements. The scanning parameters are identically chosen to scan no. 2. Therefore, both stitched images can be directly compared to indicate potential photodamage caused by the laser.

To perform VIS and NIR reflectance spectroscopy, the camera has to be dismounted and the tube system (Figure 3(a2)) has to be assembled. Due to the reconstruction measure, it is advised to carry out these measurements at last. The sequence of VIS and NIR spectroscopy does not matter. However, both spectroscopic methods require the detection of the dark signals at the switched-off halogen lamp prior to the initial measurements. The signal intensity for VIS and NIR spectroscopy as a function of the height position does not vary as much as the Raman signal as a function of the height position. Therefore, the height positions at the minimum lateral resolutions (VIS: $-46\ \mu\text{m}$, NIR: $-73\ \mu\text{m}$) are recommended while performing reflectance spectroscopy.

Data acquisition is complemented (scan no. 9) by bright-field images of the haematoxylin and eosin (H&E)-stained sample in the transmitted light mode.

3.2 Scanning experiments for tissue analysis

3.2.1 Distinction between grey and white matter of brain tissue

Stitched photographs using the 5x magnification of the global run and the local run are illustrated in Figure 33.

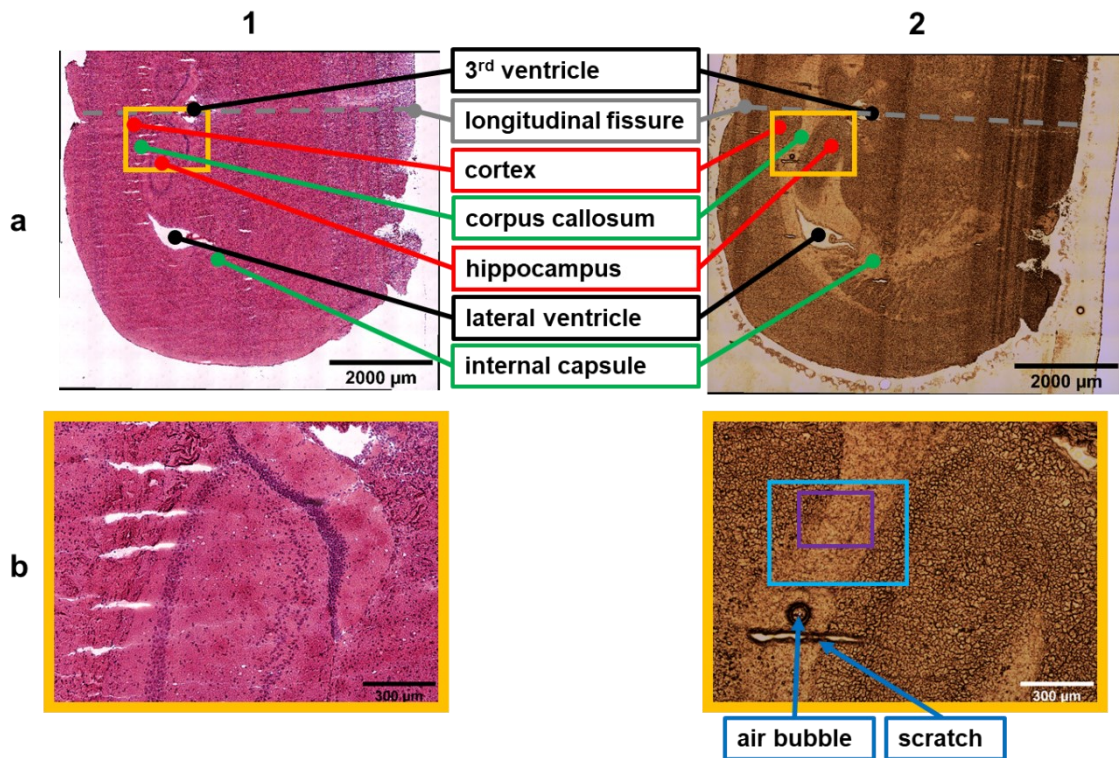


Figure 33 Stitched images of the stained (1) and unstained (2) samples, results of the (a) global run and the (b) local run. Setup configuration: bright-field microscopy (transmitted mode: 1a, 1b; incident mode: 2a, 2b); objective: 5x; photographs: 10 x 12 (1a), 11 x 12 (2a), 2 x 2 (1b, 2b); travel range: 6480 µm x 5940 µm (1a), 7200 µm x 5940 µm (2a), 720 µm x 540 µm (1b, 2b); voltage setting: 12 V (1a, 1b), 5 V (2a, 2b); integration time: 10 ms (1, 2).¹ Note: 10 x 12 or 6480 µm x 5940 µm (examples) to specify the photographs or the travel range indicate the number of photographs or travel range per row (x-coordinate) and (x) column (y-coordinate). The same applies to all setup configurations in the subsequent figure captions.

Figure 33 presents images from a cryosection of the hippocampus (dorsal). While the photographs of the haematoxylin and eosin (H&E)-stained samples in column 1 are recorded in the transmitted light bright-field mode, the photographs of the corresponding unstained samples in column 2 are taken in the incident light bright-field mode. Consequently, the stitched images result from scan no. 1 (incident light microscopy) and scan no. 9 (transmitted light microscopy) of the created workflow for tissue analysis (Table 4).

For the global scan (Figure 33 (1a, 2a)), it is sufficient to scan one cerebral hemisphere because the brain is cut in the coronal plane. Hence, all tissue sections show

symmetrical brain structures. The axis of symmetry, where the structures are mirrored, is the so-called longitudinal fissure (Figure 33a, grey dashed lines).

The tissue sections are examined by experienced researchers trained in mouse anatomy. Furthermore, regions of interest (ROI) and the main parts are identified. The main parts' annotation follows the labelling from the Allen Brain Atlas.^{110,111} Additional to grey matter (GM) (red label) and white matter (WM) (green label), ventricles are labelled in black. Ventricles like the 3rd ventricle and the lateral ventricle are cavities filled with cerebrospinal fluid. GM include the cortex and the hippocampus. Regions of the WM are the corpus callosum and the internal capsule.

Figure 33 (1b, 2b) represent the stitched images obtained with the 5x objective during the local scan. The smaller image sections show portions of the cortex, corpus callosum, and hippocampus. The location of these small areas within the cerebral hemispheres is illustrated by the orange frames in Figure 33 (1a, 2a). Regarding the unstained tissue section, artefacts like an air bubble and a scratch also facilitate the visual assignment of the location. The bright blue frame in Figure 33 (2b) highlights the area of the local scan applying the microscopic modes using the BD20x objective (Table 4, scan no. 2-5). The smaller purple frame within the blue frame marks the ROI where spectra acquisition with the molecule-specific but time-consuming Raman spectroscopy and the visible/near-infrared (VIS/NIR) reflectance spectroscopy are performed.

Based on the images in Figure 33, GM and WM can be visually differentiated from the H&E-stained sections due to an accumulation of the dark coloured cells in the GM, caused by the higher cell density compared to the cell density in WM. However, bright-field images of the unstained tissue sections show heterogeneity that can be linked to the structural heterogeneity of the stained sections. The WM of the unstained tissue section is bright, whereas the GM appears darker in bright-field images. The part on the microscope slide that surrounds the cryosection (see Figure 33 (2a)) is the mounting medium, optimal cutting temperature (OCT).

The evaluation of the remaining modalities (scan no. 2-8) is subsequently shown for the global scan. Column 1 in Figure 34 shows the stitched photographs obtained from the different microscopic modes and column 2 contains the created images based on the evaluation of the recorded spectra. Information on the respective image's setup parameters is provided in the figure caption of Figure 34.

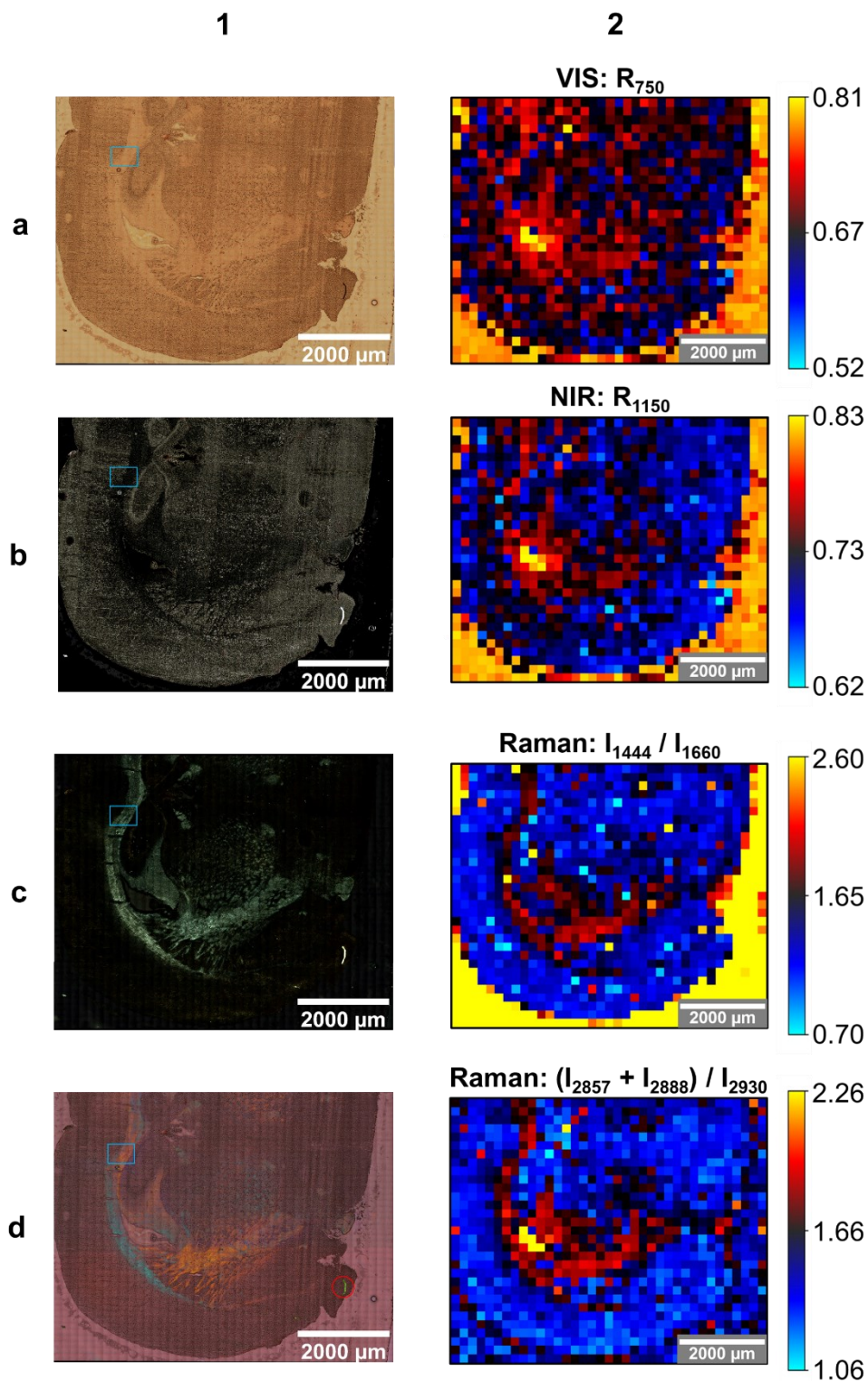


Figure 34 Stitched images (1) and created images (2) of the unstained tissue section, results of the global run. Setup configuration: bright-field microscopy (1a), dark-field microscopy (1b), polarisation microscopy (1c, 1d), reflectance spectroscopy (2a, 2b), Raman spectroscopy (2c, 2d); objective: BD20x (1a-d), BD50x (2a-d); photographs: 41 x 45 (1a-d), spectra: 37 x 31 (2a-d); travel range: 7200 μm x 5940 μm (1a-d), 7200 μm x 6000 μm (2a-d); voltage setting: 5 V (1a, 2a), 12 V (1b-d, 2b); laser power: 500 mW (2c-2d); integration time: 10 ms (1a), 15 ms (1b), 150 ms (1c), 50 ms (1d), 100 ms (2a), 200 ms (2b), 4000 ms (2c, 2d). Modified from ¹

Similar to the bright-field images in Figure 33 (2), the WM within bright-field photographs taken with the BD20x objective (Figure 34 (1a)) appear bright, whereas the morphological structure of GM appears darker. In contrast, GM is bright and WM is dark within dark-field photographs (see Figure 34 (1b)). Images obtained from polarised-light microscopy (Figure 34 (1c)) particularly emphasise WM, whereas the remaining parts of the image stay dark. Polarisation microscopy with the activated whole-wave compensator (WWC) enables a qualitative differentiation of WM based on the colour coding (see Figure 34 (1d)). Thereby, the internal capsule is highlighted by intensive orange colour and the majority of the corpus callosum is coloured in bright turquoise. A bright green segment, marked by a red circle, at the lower right part in Figure 34 (1d) is identified as an artefact on the brain section. The blue frame in the images of column 1 displays the area where the local scan is performed with identical microscopic modalities. The results of the local scan are shown at a later stage.

The global scan's results based on the spectroscopic data (scan no. 6-8) are illustrated by the created images in column 2 (Figure 34). Again, regarding the colouring of the pixels, the highest values are yellow while the lowest values are coloured in bright blue. The sample's reflectivity at 750 nm (using equation 5) is visualised in Figure 34 (2a). The corresponding qualitative reflectance spectra of GM and WM are exemplarily shown in Figure 35a.

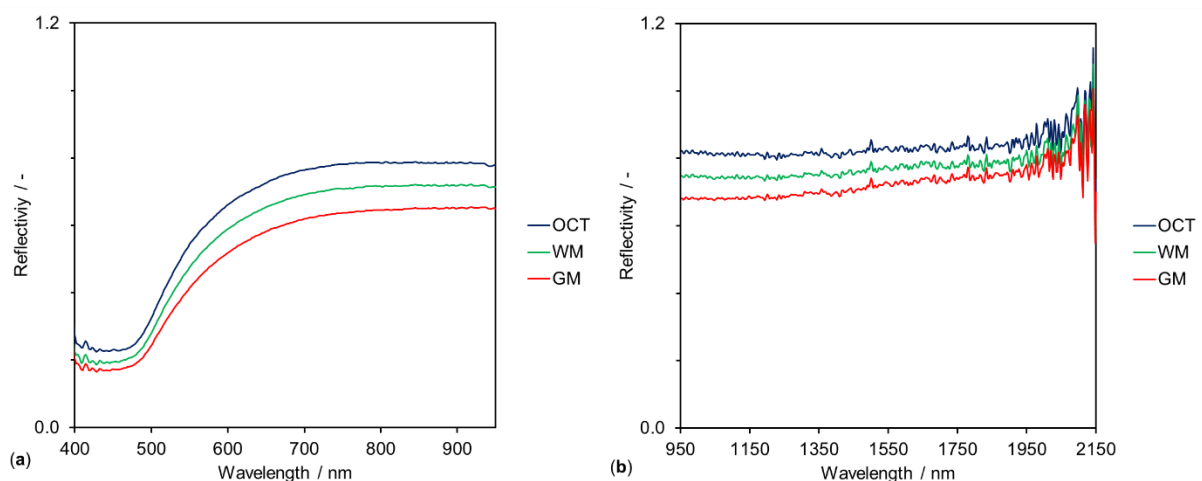


Figure 35 Reflectance spectra (averaging over 9 spectra) of white matter (WM), grey matter (GM) and optimal cutting temperature compound (OCT) in the (a) VIS spectral region, (b) NIR spectral region.¹

Additionally to the reflectance spectra of GM and WM, the reflectance spectrum of OCT is also illustrated. Although the transparent OCT is a side component that surrounds the cryosections, OCT affects the spectral evaluation of the global scan. This is

indicated by the few yellow pixels located at the lateral ventricle and the single yellow pixel identified at the location of the 3rd ventricle (see Figure 34 (2a)). In contrast, the pixels in the OCT area are rather orange. This is a verification of the OCT's reduction of the backscattered light compared to the reflectivity of the gold-coated slide without brain tissue (ventricles). Nevertheless, the reflectivity at OCT is higher compared to the reflected intensities at WM and GM.

Since the measuring principle is in transflection, forward-scattered light is reflected at the gold-coated surface of the microscope slide. Consequently, the incident light transmits the sample twice. All reflectance spectra in Figure 35a show similar spectral characteristics with a drop around 450 nm. This drop is caused by the spectral characteristic of gold that absorbs light in the blue spectral region. Reflectivity increases in the adjacent spectral range from 500 nm to 700 nm and stays constant between 700 nm and 950 nm. OCT shows the overall highest reflectivity of the three analytes. The lowest reflectivity between 400 nm and 950 nm is detected for GM. Hence, the coloured pixels in the WM region are reddish and GM appear rather bluish. The chosen wavelength for data evaluation and image creation (Figure 34 (2a)) is at 750 nm (R_{750}). This wavelength lies in the optical window of tissue between 600 nm and 940 nm,⁷ unaffected by absorption properties of haemoglobin, the main absorber in blood-perfused tissue.¹⁶ Consequently, the created image to distinguish between GM and WM is based on differences in reflection properties at 750 nm and does not contain information regarding chemical composition.

Analogue to data evaluation in the VIS spectral region, the created images obtained from NIR reflectance spectra are based on the reflectivity at a wavelength in a further optical window between 1000 nm and 1350 nm.²¹

The colour coding in Figure 34 (2b) at 1150 nm is similar to the pixel's colourisation in Figure 34 (2a). The reason is the spectral characteristics of GM, WM, and OCT. Like in the VIS spectral region, OCT shows the highest reflectivity, followed by WM and GM. In contrast to the VIS reflectance spectra, NIR reflectance spectra (Figure 35b) fluctuate across the entire NIR spectral range. This fixed pattern is still PRNU of the extended wavelength InGaAs detector. One reason why the PRNU is not fully compensated in the reflectance spectra is the arrangement in transflection in combination with the sample's specular reflection (gold-coating of the slide) and the Zenith Polymer[®]'s diffuse reflection. The reflectivity of the diffuse reflectance standard is also responsible for the increase in reflectivity at longer wavelengths. The specified

reflectivity of 99% applies to wavelengths below 1350 nm. At wavelengths above 1350 nm, reflectivity decreases slightly and at 2100 nm, a reflectivity of only 94% is guaranteed. The spike around 1500 nm (see Figure 35b) is caused by a defective pixel of the NIR spectrometer. Against expectation, the recorded NIR spectra do not show absorption bands of water or biomolecules.

Images to distinguish between GM and WM based on differences in chemical composition are created by evaluating the detected Raman spectra. Pre-processed Raman spectra, representative of GM, WM, and OCT, are illustrated in Figure 36. Furthermore, Raman peaks frequently used to distinguish between GM and WM are marked with dashed vertical lines. The peaks' assignment to lipid and protein is shown in Table 5.

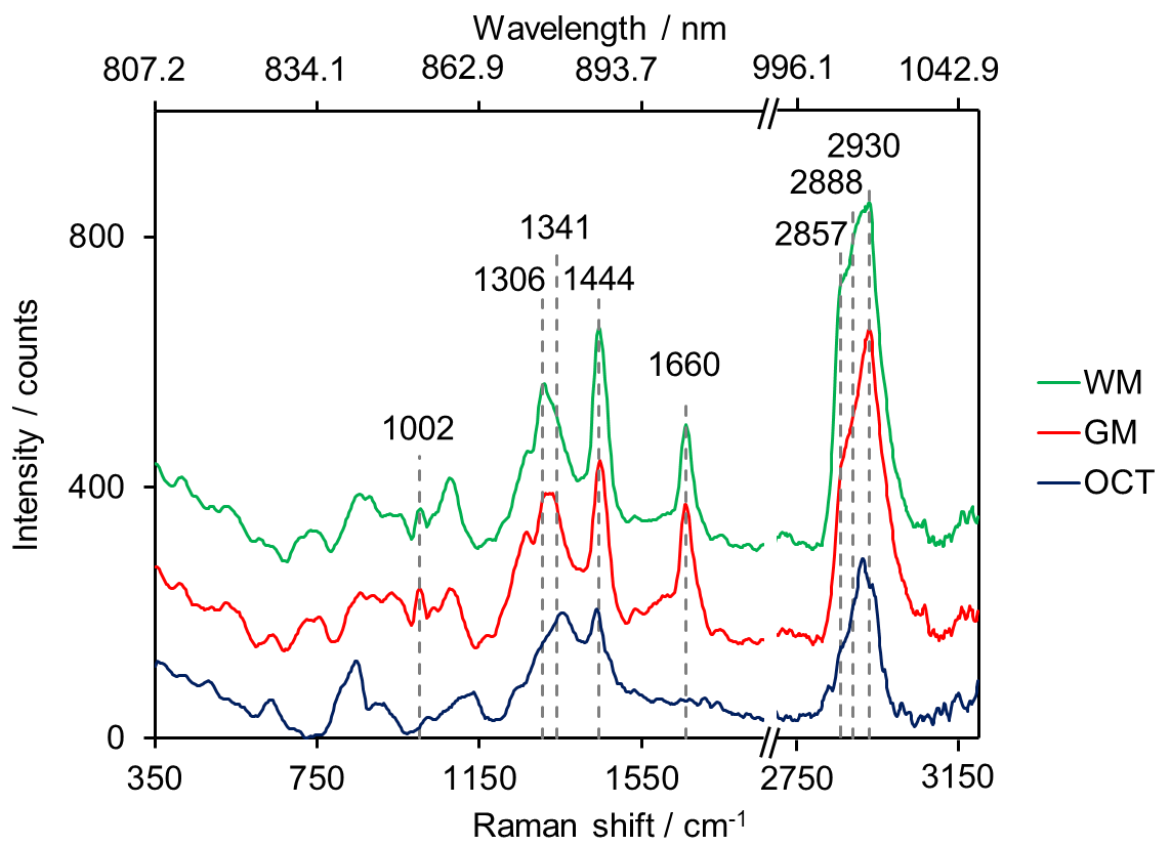


Figure 36 Pre-processed Raman spectra (averaging over 9 spectra) of white matter (WM), grey matter (GM), and optimal cutting temperature compound (OCT), offset: +150 counts (GM), +300 counts (WM).¹

Table 5 Raman peak position and assignment of functional groups to distinguish GM and WM¹

Peak position / cm ⁻¹	Lipid assignments	Protein assignments	References
1001 - 1008		C-C ring breathing of phenylalanine	47,59,112
1296 - 1308	CH ₂ twisting and wagging		48,68,113
1337 - 1344		C-H deformation, C-H bending	48,113
1438 - 1452	CH ₂ bending and scissoring CH ₃ bending	CH ₂ bending and scissoring CH ₃ bending	47,112,114
1659 - 1664	C=C stretching	Amide I (C=O stretching)	46,47,59
2850 - 2860	CH ₂ symmetric stretching	CH ₂ symmetric stretching	59,112,113
2880 - 2895	CH ₂ asymmetric stretching	CH ₂ asymmetric stretching	59,112,113
2929 - 2937	CH ₃ stretching	CH ₃ stretching	59,112,113

The intensity (I) ratios of the evaluated Raman peaks are adapted from literature and include the following intensity ratios and the sum of two intensity ratios: I_{1299}/I_{1439} ,⁶⁸ I_{1300}/I_{1344} ,⁴⁸ I_{1441}/I_{1659} ,⁴⁷ I_{1442}/I_{1662} ,⁴⁶ I_{1443}/I_{1008} ,⁵⁹ I_{2930}/I_{2845} ,⁶⁹ $(I_{2850}+I_{2882})/I_{2930}$.⁵⁹

Images based on Raman spectra from the global scan are exemplary created for a peak ratio in the fingerprint region (Figure 34 (2c)) and the sum of two intensity peak ratios in the high-wavenumber region (Figure 34 (2d)). The Raman intensity peak at 1444 cm⁻¹ of Figure 34 (2c) is primarily assigned to the CH₂ and the CH₃ vibration modes in lipids. The ratio's denominator is the intensity peak at 1660 cm⁻¹. This peak is characteristic of proteins (Amide I band). Since OCT has no characteristic Raman peak at 1660 cm⁻¹, the highest ratios (yellow pixel) in Figure 34 (2c) are achieved for OCT. Moreover, the peak ratio in the lipid-rich WM is higher than in GM. This is in good accordance with the illustrated Raman spectra in Figure 36. The ventricle does not show contrast in pixel colour because of the fluorescence signal of the glass, the microscope slide's substrate for the 120 nm thin gold film. Consequently, the background signal is not fully compensated by the data pre-processing.

The ventricles in Figure 34 (2d) show colour contrast. The magnitude of approximately 2 for yellow pixels is plausible since the evaluation is based on the sum of two peak ratios in the high-wavenumber region where glass does not show Raman peaks. Little variation is caused by the higher fluctuations in the higher wavenumber region due to the correction file for Raman spectra. Because of their similar Raman

spectra in the high-wavenumber region, a sufficient differentiation of GM and OCT based on the CH stretching modes is not possible.

An illustration of the entire evaluated Raman peak ratios and the sum of two peak ratios is shown for the local scan in Figure 37 (2c, 2d, 3a-3d).

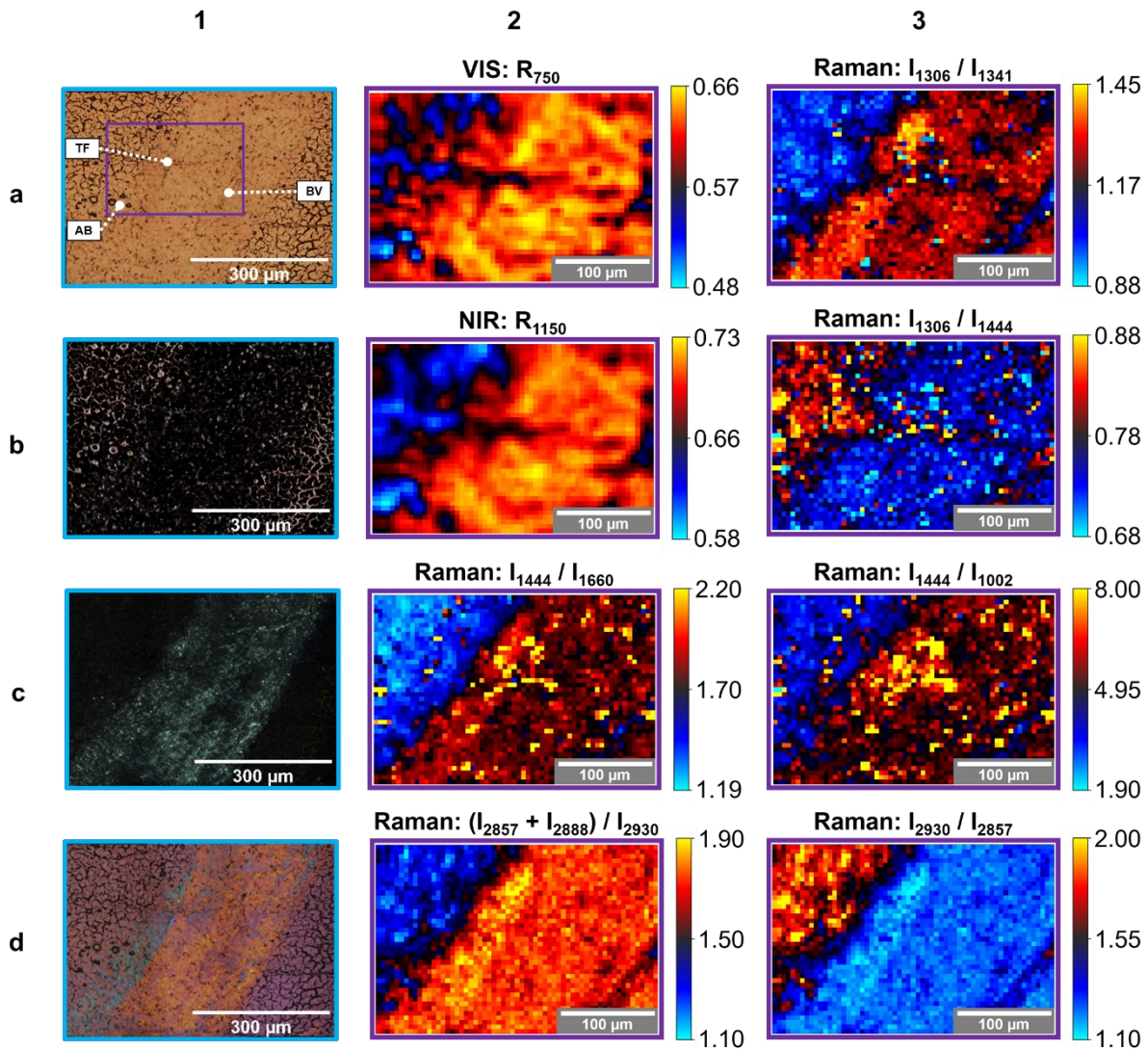


Figure 37 Stitched images (1) and created images (2) of the unstained tissue section, results of the local run. Setup configuration: bright-field microscopy (1a), dark-field microscopy (1b), polarisation microscopy (1c, 1d), reflectance spectroscopy (2a,2b); Raman spectroscopy (2c, 2d, 3a-d); objective: BD20x (1a-d), BD50x (2a-d); travel range: 360 μm x 270 μm (1a-d), 300 μm x 200 μm (2a-d, 3a-d); photographs: 3 x 3 (1a-d), spectra: 41 x 61 (2a-d, 3a-d); voltage setting: 5 V (1a, 2a), 12 V (1b-d, 2b); laser power: 500 mW (2c, 2d, 3a-d); integration time: 10 ms (1a), 15 ms (1b), 150 ms (1c), 50 ms (1d), 100 ms (2a), 200 ms (2b), 4000 ms (2c-d, 3a-d). Modified from ¹

The purple rectangle in Figure 37 (1a) displays the ROI for spectra acquisition. The smaller area comprises a boundary between GM (cortex) and WM (corpus callosum). For further data evaluation, three landmarks are determined: a tissue fold (TF) in the

centre, three air bubbles (AB) in the lower-left corner, and a blood vessel (BV) in the lower-right corner.

Particularly the air bubbles and the tissue fold are identified within the created images based on VIS reflectance (Figure 37 (2a)) and NIR reflectance (Figure 37 (2b)) spectra. However, the contrast in the image obtained from the NIR spectra evaluation is poorer than the images created based on the wavelength in the VIS spectral region. This is most likely due to the decrease in lateral resolution with increasing wavelengths, according to the diffraction limit. Therefore, the three air bubbles in Figure 37 (2b) are not fully resolved using NIR spectroscopy. Anyhow, the lower reflectivity values of the air bubbles and the tissue fold conform with the dark appearance of these landmarks in the bright-field image.

Regarding the photographs (Figure 37 (1a-1d)), GM and WM are also visually differentiable in the local scan. Identically to the results of the global scan, the WM in the photographs obtained with polarisation microscopy and the activated WWC (Figure 37 (1d)) show additional colour gradation.

Differentiation within the WM is also observed in the created images based on the evaluation of the Raman spectra in the high-wavenumber region. The yellow pixels of the WM in Figure 37 (2d) correspond to the blue pigmentation within the corpus callosum in the case of polarisation microscopy with WWC. Moreover, the blood vessel can be easily identified in Figure 37 (2d). Figure 37 (3d) highlights similar sample characteristics with the reversed colour assignment.

The pixel colourisation depends on the evaluated intensity ratios, whether it is a lipid-to-protein ratio or a protein-to-lipid ratio. Lipid-to-protein ratios with the lipid characteristic peak in the ratios' numerator result in high values (yellow and reddish pixels) in the WM region. Vice versa, GM with a higher protein content is emphasised by bluish pixels. The blood vessel is identified with all intensity peak evaluations (Figure 37 (2c, 2d, 3a-d)). Especially in Figure 37 (2c, 3c), the suspicion of a tissue fold is confirmed by yellow pixels since the overlap in lipid-rich tissue increased the peak ratios in the fingerprint region.

Altogether, every evaluation of the chosen peak ratios or the sum of two peak ratios using the Raman spectra reveals a clear boundary between GM and WM. The created images (Figure 37 (2c, 2d, 3a-d)) originate from a single Raman scan (Table 4, scan no. 6) at an integration time of 4 s per pixel.

To check whether the heat input results in tissue damage, an additional scan (Table 4, scan no. *) in the incident light bright-field mode is performed after the Raman scan. The absence of visible photodamage (see Figure 38) is verified by calculating the mean-squared error based on a pixel-to-pixel comparison of the two images.

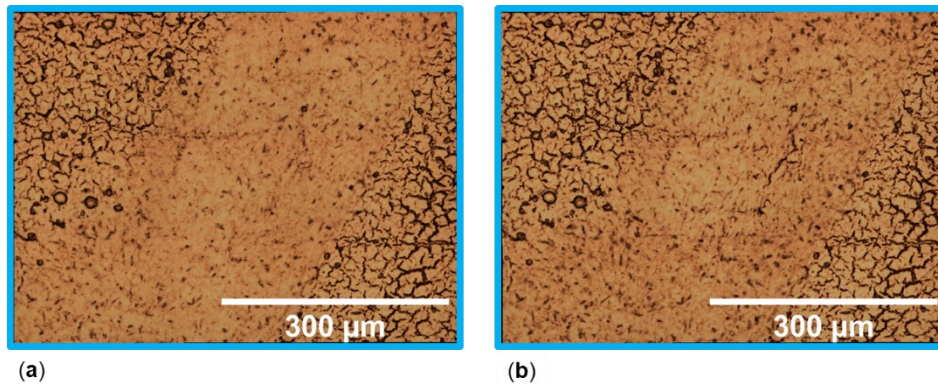


Figure 38 Stitched images (20x objective) of the unstained sample recorded in the incident light bright-field mode. Results of (a) step no. 2 (identical to Figure 37 (1a)) and (b) step no. * of the local scan ¹

The mean-squared error results in 0.05. This confirms the absence of photodamage. Although 4 s per pixel does not alter or destroy the tissue section, performing a Raman scan is extremely time-consuming. The total measurement time includes the integration time and the instrumentation time (t_{stage} , t_{readout} , and t_{transfer}) and results in approximately 3 h for Raman spectra acquisition during the local scan. In contrast, spectra acquisition of VIS and NIR spectra takes 12 min and 16 min, respectively. The fastest modalities are the microscopic ones. For each modality, the recording of the photographs takes less than 1 min. For the global scan, the total measurement times lie between 30 min for incident light bright-field microscopy and 90 min for Raman spectroscopy.

An indicator for a potential reduction of the integration time for Raman spectroscopy is the signal-to-noise ratio (SNR) of the single intensity peaks. The SNR of the evaluated peaks in the Raman scan is calculated similarly to the SNR for the determination of the appropriate fibre diameter of the Raman setup. Due to the decrease in spectral resolution resulting from the absent data interpolation, using the developed LabVIEW™ programme instead of the MultiSpec® Pro II software, the noise range is expanded to 2500 cm^{-1} to 2548 cm^{-1} . The threshold value for the SNR in analytical chemistry is usually 3. Peaks with SNRs below this value are regarded as noise and cannot be evaluated.

The critical SNR of the evaluated Raman peaks originates from the lowest peak intensities at 1002 cm^{-1} . A visualisation of the SNR at 1002 cm^{-1} , obtained from the local scan with an integration time of 4 s, is shown in Figure 39.

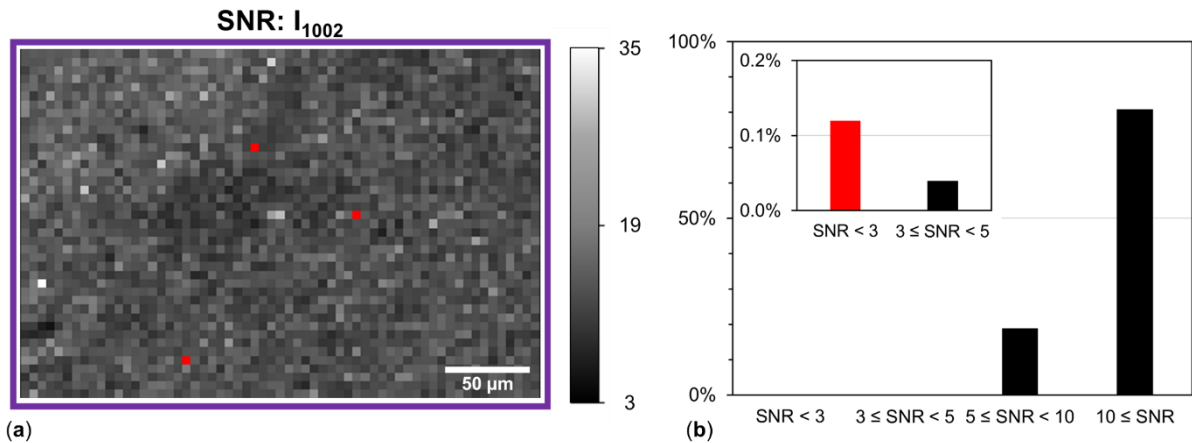


Figure 39 Signal-to-noise ratios (SNRs) at 1002 cm^{-1} (a) of each pixel within the local scan and (b) as a bar chart of the overall ratios. Setup configuration (a): Raman spectroscopy; objective: BD50x; travel range: $300\text{ }\mu\text{m} \times 200\text{ }\mu\text{m}$; spectra: 61×41 ; laser power: 500 mW; integration time: 4 s.

Similar to the created images for the distinction between GM and WM, the pixels (Figure 39a) are colourised according to their value. The scale ranges from SNRs of 3 to 35. The lowest value is coloured black and the highest value is coloured white. Pixels with SNRs below 3 appear red.

Within the entire scanned area of the local scan (2501 pixels), only three pixels (red pixels) have SNRs smaller than 3. This corresponds to 0.12%. The small number of SNRs below 3 of the smallest evaluated Raman peak intensity at 1002 cm^{-1} indicates that the results of the peak ratios are reliable. Moreover, the bar chart in Figure 39b shows the clustered percentage of the SNRs. The diagram visualises that more than 99% of the SNRs have values higher than 5. Consequently, the Raman scan can be performed with shorter integration times.

Therefore, a subsequent Raman scan is performed with an integration time of 1 s per pixel. This enables the increase of the scan area by a factor of 4, which results in a travel range of $600\text{ }\mu\text{m} \times 400\text{ }\mu\text{m}$ (121×81 spectra). Figure 40 shows the pixels' SNRs of three Raman peaks at (a) 1002 cm^{-1} , (c) 1444 cm^{-1} , and (d) 1660 cm^{-1} .

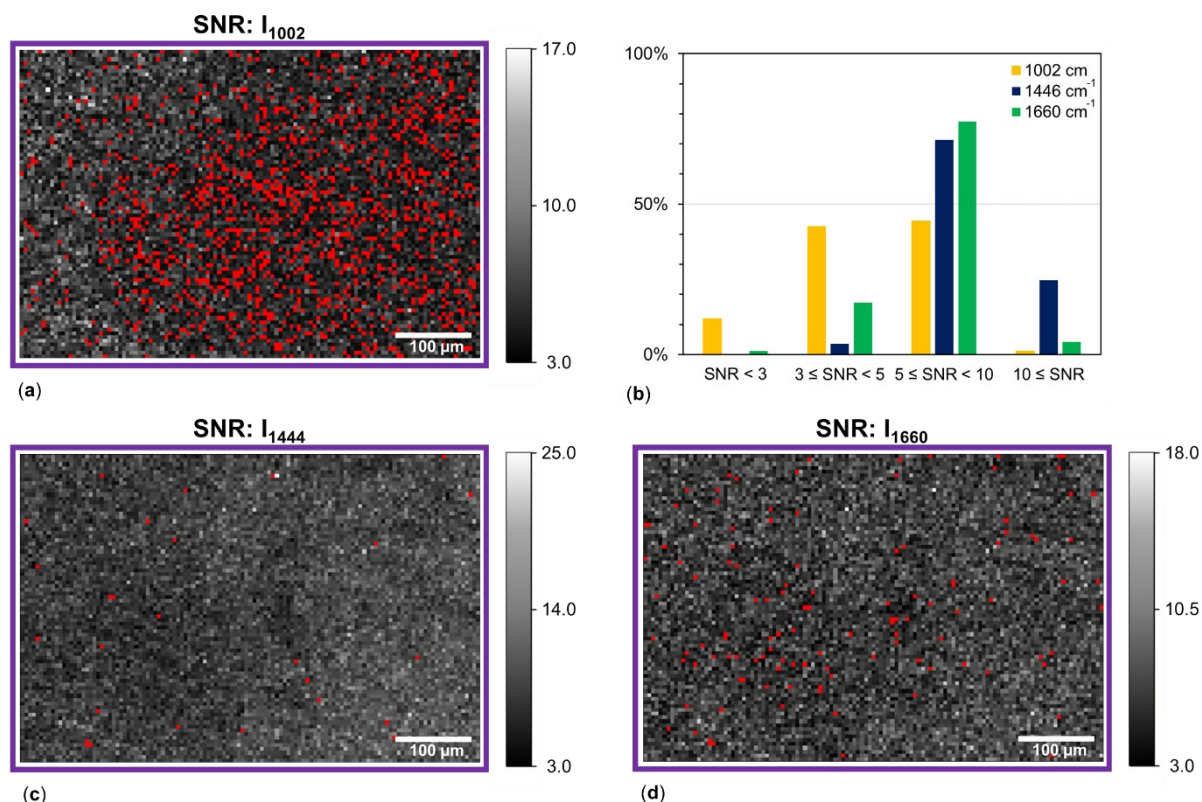


Figure 40 Signal-to-noise ratios (SNRs) at (a) 1002 cm⁻¹, (c) 1444 cm⁻¹, and (d) 1660 cm⁻¹ of each pixel in the Raman scan at an integration time of 1 s; (b) bar chart of the overall ratios. Setup configuration (a, c, d): Raman spectroscopy; objective: BD50x; travel range: 600 μm x 400 μm; spectra: 121 x 81; laser power: 500 mW; integration time: 1 s.

The colour gradation of the pixels is identical to Figure 39a. An overview of the assorted SNRs for the three Raman peaks is shown in Figure 40b. In Figure 40a, 1165 pixels out of 9801 pixels have SNRs smaller than 3 (red pixels). This corresponds to 12%. Such an amount of SNRs below the threshold value is unsatisfactory for using the Raman peak at 1002 cm⁻¹ for data evaluation. In contrast, the percentage of the inadmissible SNRs is 0.3% (27 red pixels) and 1.2% (116 red pixels) for Raman peaks at 1444 cm⁻¹ (Figure 40c) and 1660 cm⁻¹ (Figure 40d).

Figure 41b visualises the created image based on the intensity peak ratios in the Raman spectrum at 1444 cm⁻¹ and 1660 cm⁻¹.

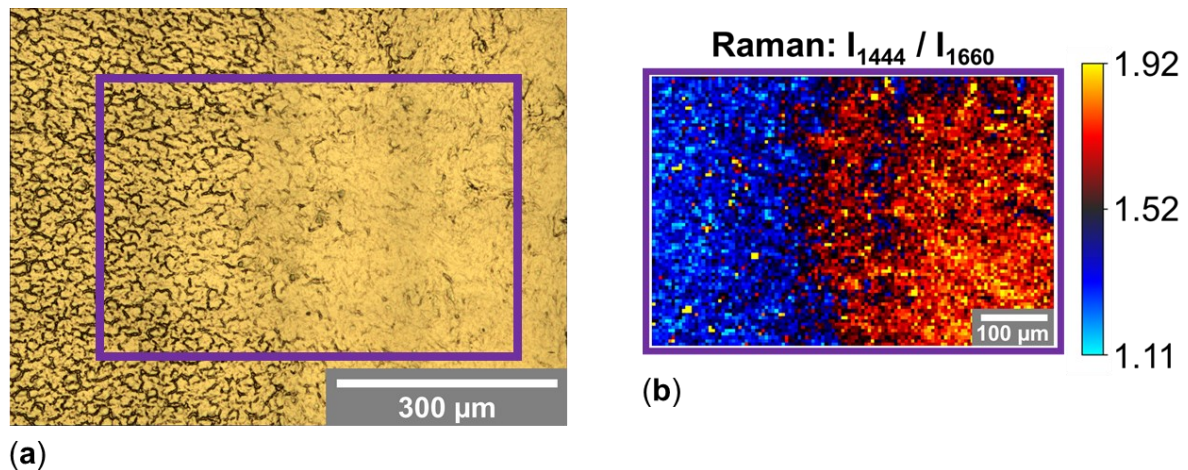


Figure 41 Stitched image (a) and created image (b) of the unstained tissue section, results of a run with decreased integration time for Raman spectroscopy. Setup configuration: bright-field microscopy (a), Raman spectroscopy (b); objective: BD20x (a), BD50x (b); travel range: 540 µm x 405 µm (a), 600 µm x 400 µm (b); photographs: 4 x 4 (a), spectra: 121 x 81 (b); voltage setting: 12 V + neutral density filter (a), laser power: 500 mW (b); integration time: 10 ms (a), 1 s (b).

The location of the scanned area for the enlarged Raman scan in Figure 41a is highlighted by the purple frame. A comparison of the scanned areas shows good consistency. Although landmarks such as air bubbles, a blood vessel, and a tissue fold are not localised in this area, the boundary between GM and WM is visible in both images. Within the transition section from GM and WM, portions of GM are detected and highlighted by blue pixels in the reddish WM area. The colour coding of GM and WM in Figure 41b corresponds to the colour coding of the local scan's respective evaluation (Figure 37 (2c)). Moreover, the values for the calculated intensity ratios are approximately between 1 and 2 for the Raman scan at an integration time of 4 s and 1 s. The representative colours in the bright-field image (Figure 41a) differ from the colours of the previous bright-field images. As it turned out retrospectively, the white balance of the global and the local scan was inaccurate. This results in a slight colour shift. However, the differentiation between GM and WM is not affected.

3.2.2 Detection of haemorrhage in a brain section

A further application of the multimodal imaging system is the visualisation of haemorrhage. Since bright-field microscopy, VIS spectroscopy, and Raman spectroscopy should be able to detect blood, these modalities are used to prove whether the detection of haemorrhage in the unstained brain section is possible.

Figure 42a visualises the stitched image based on photographs obtained in the incident light bright-field mode.

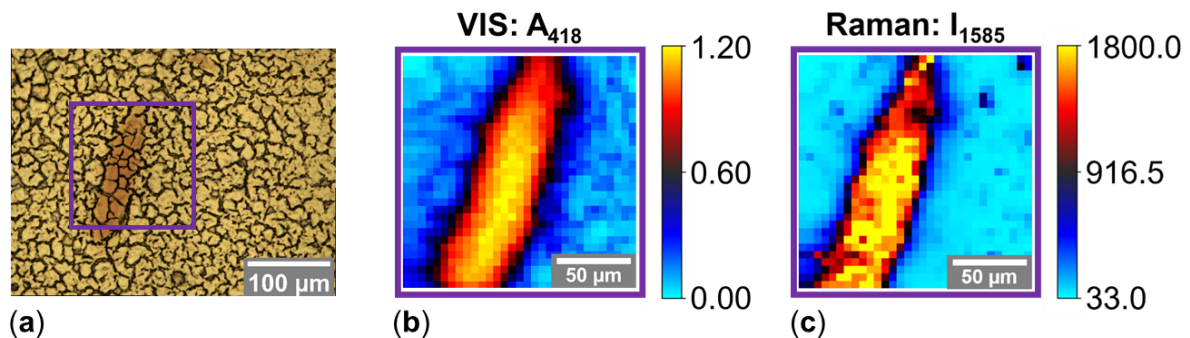


Figure 42 Stitched image (a) and created images (b, c) of the unstained tissue section with haemorrhage, results of a run to prove haemorrhage detection. Setup configuration: bright-field microscopy (a), VIS spectroscopy (b), Raman spectroscopy (c); objective: BD20x (a), BD50x (b, c); travel range: $180\ \mu\text{m} \times 135\ \mu\text{m}$ (a), $150\ \mu\text{m} \times 150\ \mu\text{m}$ (b, c); photographs: 2×3 (a), spectra: 31×31 (b, c); voltage setting: $12\ \text{V} + \text{neutral density filter}$ (a), $12\ \text{V}$ (b), laser power: $200\ \text{mW}$ (c); integration time: $10\ \text{ms}$ (a, b), $10\ \text{s}$ (c).

The haemorrhage is clearly visible as the red coloured oval on the tissue section (GM). The purple frame indicates the area for spectral data acquisition. While VIS spectroscopy is used to distinguish between GM and WM based on differences regarding reflection properties, blood is characterised by absorption bands of haemoglobin in the VIS spectral range. Therefore, the absorption spectra (using equation 6) instead of the reflectance spectra are calculated. Since the absorption bands of haemoglobin are located in a similar spectral range as the absorption band of gold, the microscope slide's coating, the reference spectrum I_0 is replaced. Instead of the Zenith Polymer[®]'s intensity spectrum, the first detected intensity spectrum of the VIS scan is used as a reference spectrum. This is feasible since the spectrum originates from GM. Consequently, the calculated absorbance is not influenced by the spectral characteristics of gold and GM. Figure 43 shows representative absorption spectra of haemorrhage and GM.

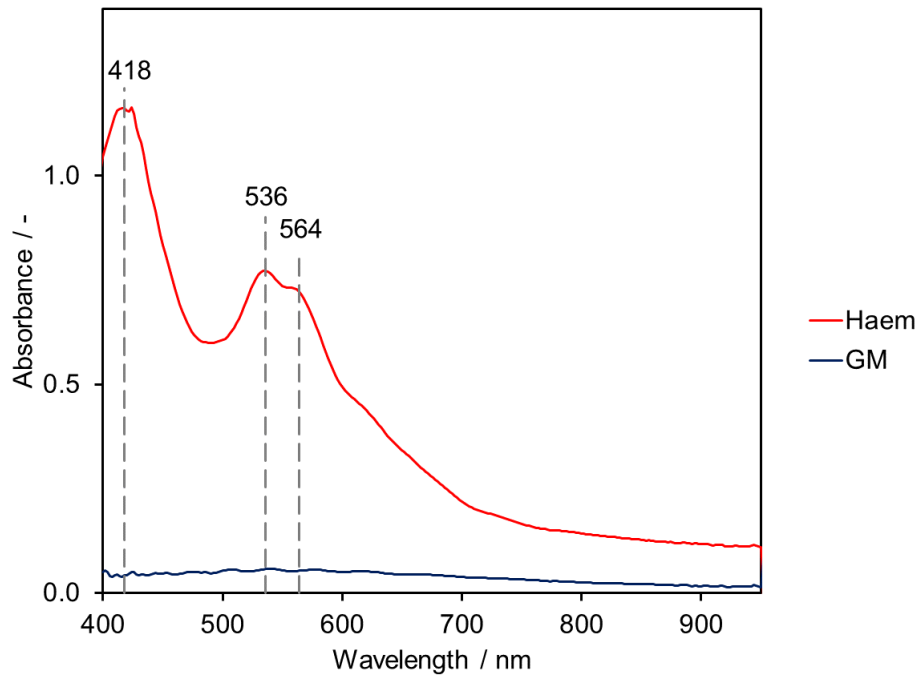


Figure 43 Absorption spectra (averaging over 9 spectra) of haemorrhage (Haem) and grey matter (GM). See text for details.

While the absorption spectrum of GM does not show absorption bands, the red curve of haemorrhage shows one peak at 418 nm and a double peak at 536 nm and 564 nm. The absorption band at 418 nm is used to visualise the location of the haemorrhage within the scanned area. The created image (Figure 42b) illustrates the haemorrhage by yellow pixels encircled from red pixels. The GM appears blue in the image. This colour distribution localises the highest absorbance at 418 nm in the centre of the haemorrhage and a lower absorbance in the boundary area. The blue pixels in the GM area show a slight structure where the darker pixels might originate from darker portions within the GM. The first pixel in the upper left corner is bright blue, which corresponds to an absorbance value of zero. This is plausible since the first pixel is the location of the reference spectrum for calculating the absorbance.

Regarding the visualisation of the haemorrhage, a similar result is obtained for the created image using Raman spectroscopy (Figure 42c). The evaluated intensity is the intensity value of the Raman peak at 1585 cm^{-1} , a characteristic peak assigned to haemoglobin.⁴⁷ In contrast to the evaluation for the distinction between GM and WM, the total intensities instead of peak ratios are used. The intensities of the scan range from 33 counts to 1800 counts. Due to the absence of haemoglobin in GM, it is not expected to detect high intensities at 1585 cm^{-1} . However, the representative Raman

spectra in Figure 42 show a strong increase in the haemorrhage's Raman intensities in the fingerprint region compared to intensity values of GM.

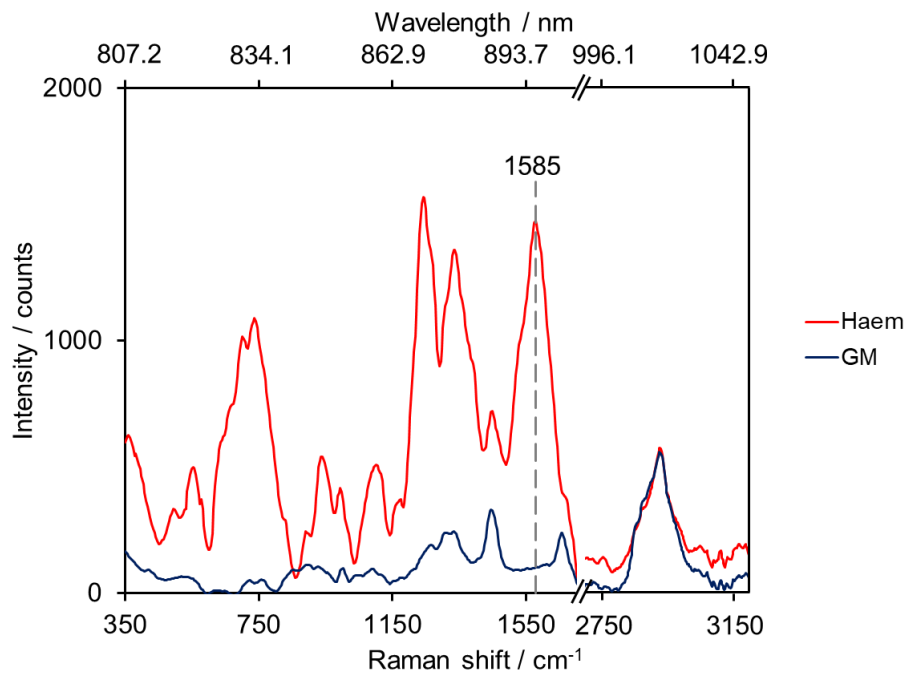


Figure 44 Pre-processed Raman spectra (averaging over 9 spectra) of haemorrhage (Haem) and grey matter (GM).

In order to prevent photodamage, the set laser power is reduced to 200 mW. As a consequence, the integration time is increased to 10 s per pixel. This results in identical heat input compared to the scanning experiments to distinguish between GM and WM at 500 mW and 4 s. Due to the linearity of the Raman signal as a function of integration time and laser power (Figure 24 and Figure 25), Raman intensities of the GM in Figure 36 and Figure 44 are directly comparable. Both Raman intensities of GM are in a similar order of magnitude. Moreover, the created image Figure 42c is in good accordance with the image section of the bright-field photographs (Figure 42a). Therefore, the experiment is rated as reliable.

3.2.3 Proof-of-concept study: NIR path

Since neither water nor biomolecules are detected in the NIR spectra during the global and the local scans to distinguish between GM and WM, a proof-of-concept to verify the design of the NIR path is carried out. The setup configuration using the BD50x objective, the fibre combination of 50+550 μm , the voltage value of 12 V, and the integration time of 200 ms remains constant.

However, Serrano ham on a gold-coated slide instead of mouse brain tissue is used. Similar to the brain tissue, the Serrano ham has an even surface and a clear boundary between two tissue sections (muscle tissue and fat). In contrast to the brain, the ham has a sample thickness of 1 mm. The scanned area for the proof-of-concept is 20 mm x 20 mm at a step size of 500 μm . Figure 45a shows a picture of the ham section.

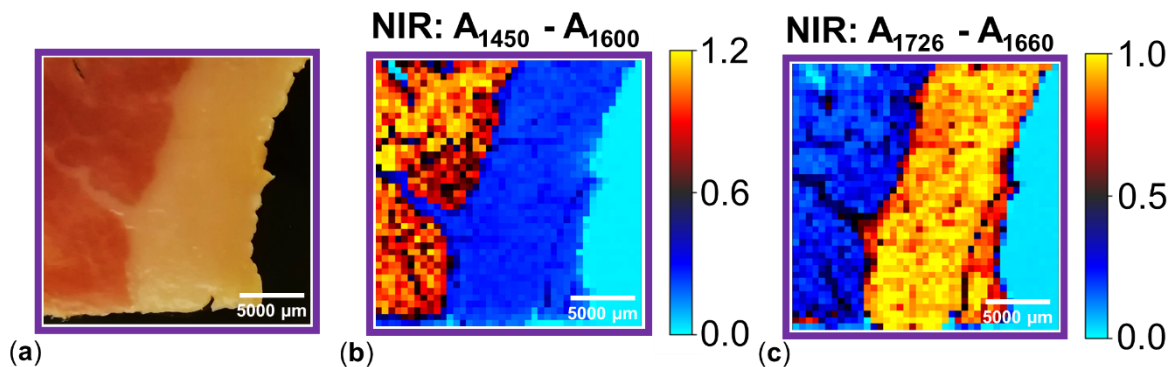


Figure 45 Picture taken with the camera of a cell phone (a) and created image (b,c) of the Serrano ham, results of a run for the NIR setup's proof-of-concept. Setup configuration (b,c): NIR spectroscopy; objective: BD50x; travel range: 20 mm x 20 mm; spectra 41 x 41; voltage setting: 12 V; integration time: 200 ms.

On the left side of the picture (Figure 45a) is the ham's red muscle tissue. The adjacent white tissue section is fat. The dark part on the right and bottom of the picture is the gold-coated microscope slide. The slide is also visible in the upper left corner of the picture due to a scratch in the tissue. A further landmark within the sample is a fat filament close to the centre of the picture that spreads from the fat section to the muscle tissue.

To calculate the absorption spectra, the Zenith Polymer[®] is used for reference. Figure 45b and Figure 45c show the created images based on the NIR absorption spectra. For data evaluation, the OH vibration mode at 1450 cm^{-1} ²¹ (Figure 45b) and the CH vibration mode at 1730 cm^{-1} ²¹ (Figure 45c) are used. To determine the detection limit of the NIR setup, the peaks' absorbances minus offset values are calculated. Both created images display the morphology of the sample. The fat filament is identified in both images by blue or black pixels in the muscle tissue and the tissue scratch is highlighted by bright blue pixels in the upper left corner. The microscope slide appears bright blue in both images due to the absence of absorption bands in the NIR spectral region.

While muscle tissue is characterised by high absorbances at 1450 nm due to high water content, fat is characterised by high absorbances at 1730 nm due to a high amount of CH molecules.

Figure 46 illustrates the representative absorption spectra for muscle tissue (red line) and fat (green line).

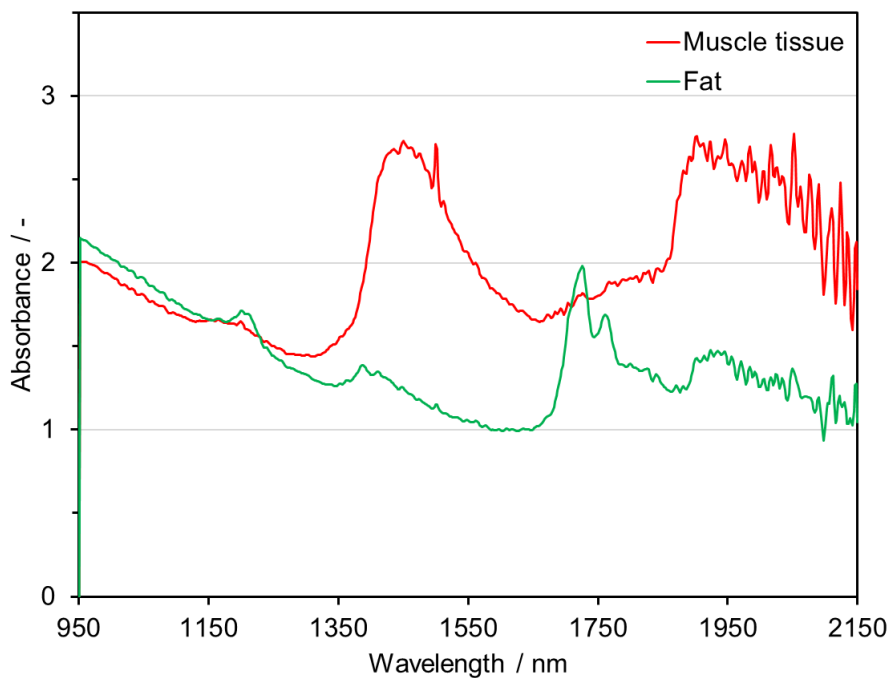


Figure 46 Absorption spectra (averaging over 9 spectra) of muscle tissue and fat. See text for details.

The absorption spectra are in good accordance with the colourisation of the created images. Muscle tissue is dominated by the absorption peak of water (OH vibration mode) at 1450 nm. The spike around 1500 nm is caused by the defective pixel of the NIR spectrometer and does not belong to the spectral characteristics of the sample. Fat is characterised by a double peak (CH vibration mode) around 1730 nm. The wavelength range above 1930 nm, where a more intense absorption peak of water is located, is not evaluated due to the minor light intensity in this spectral region.

To calculate the amount of water in the muscle tissue, an NIR spectrum of deionised water is recorded in transmission. The calculated absorption spectrum (Figure 47) belongs to a layer thickness of 100 μm .

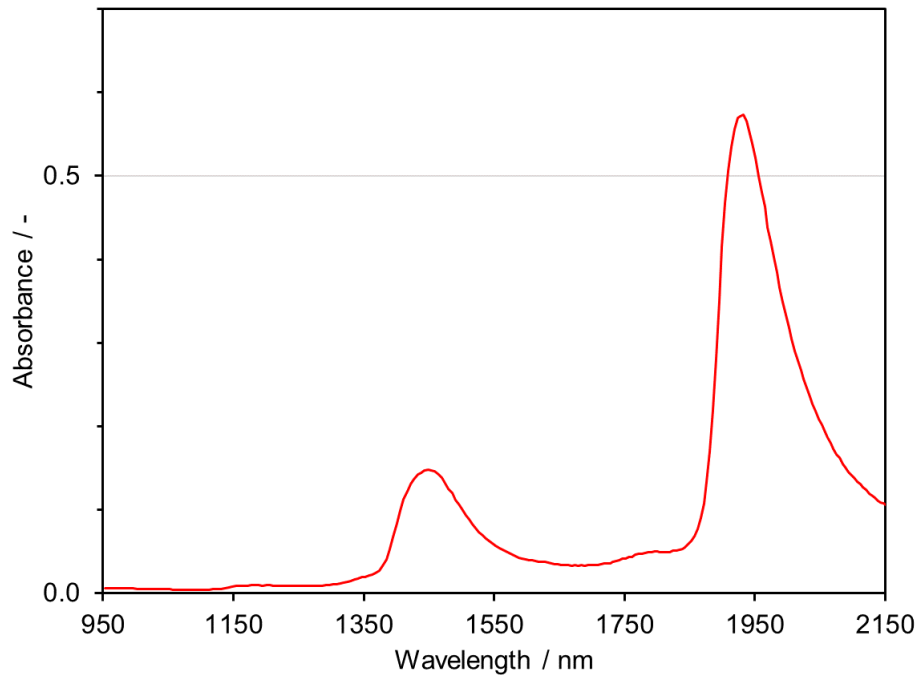


Figure 47 Absorption spectrum of deionised water in the NIR spectral region. Measurement setup: transmission, layer thickness: 0.1 mm

To verify the experiment, the molar absorptivities at 1450 nm and 1930 nm are calculated. The respective molar absorptivities (in $\text{L mol}^{-1} \text{cm}^{-1}$) result in 0.27 and 1.03, which is in good accordance with the literature (0.26 and 1.07).¹¹⁵ The corresponding absorbance at 1450 nm of a 100 μm thick layer of deionised water is 0.15 (see Figure 47).

The maximum absorbance in the Serrano ham is 1.2 (see scale Figure 45b). Assuming that the light penetrates through the entire sample thickness (1 mm), the layer thickness results in 2 mm because of the transflection measuring principle. Consequently, an absorbance of 1.2 corresponds to a maximum water content of 40%. Based on the literature, Serrano ham's water content is determined as 52.8%.¹¹⁶ The variance in the water content is most likely due to attenuations of the incident light caused by scattering. A pilot experiment (data not shown) with a 100 μm thick transparent polyethylene terephthalate (PET) film (Tartan 901, 3M, Saint Paul, MN, USA) showed that the absorbance of the layer in transflection is only 85% of the double value determined in transmission. The attenuation effect for a 1 mm layer opaque tissue is expected to be higher.

Regarding the 16 μm (layer thickness: 32 μm) brain tissue, pure water would result in absorbances of 0.05 at 1450 nm and 0.18 at 1930 nm, excluding attenuations effects. The noise (standard deviation) is 0.007 between 1440 nm and 1460 nm and

0.014 between 1920 nm and 1930 nm. An SNR of 3 requires absorbances of 0.021 and 0.042, respectively, to detect water. These absorbances correspond to minimum water contents of 42% to detect the vibrational mode at 1450 nm and 23% for the detection of the vibration mode at 1930 nm.

Assuming that the recorded absorbance of the fat peak at 1726 nm (see Figure 45c) of 1 is the maximum detectable value, a 16 μm (layer thickness: 32 μm) brain section of pure fat would result in an absorbance value of 0.016. However, the NIR spectrometer's noise is 0.010 in the wavelength range from 1720 nm to 1740 nm. A sufficient SNR requires absorbances of 0.030. Consequently, the brain section of 16 μm is too thin to detect the CH vibrational modes at 1730 nm applying the designed NIR setup.

4 DISCUSSION^f

The results for the tissue analysis show that each modality is able to distinguish between grey matter (GM) and white matter (WM) of brain tissue. Moreover, bright-field microscopy, visible (VIS) spectroscopy, and Raman spectroscopy is successfully applied to highlight haemorrhage in a brain section. The adapted light path for near-infrared (NIR) spectroscopy is also validated to detect vibrational modes of water and fat in Serrano ham.

The imaging system used to perform the entire experiments is a novel developed multimodal imaging system. This measuring device is an all-in-one solution that combines the imaging technologies of light microscopy and optical spectroscopy in one setup. The subsequent discussion evaluates the adapted modalities' design, identifies the information content obtained from the various modalities during tissue analysis, provides an outlook on further modification of the multimodal imaging systems, and draws a conclusion.

4.1 Evaluation of the multimodal imaging system, especially the design of the adapted spectroscopic modalities

The centrepiece of the multimodal imaging system is the upright microscope Leica DM R (Leica Microsystems GmbH, Wetzlar, Germany). The advantage of this microscope series is the unit assembly system that allows an almost unlimited variety of configurations. Using the basic microscope stand DM RXE, van de Poll et al.¹¹⁷ investigated, amongst other things, the chemical compositions of ceroid in human atherosclerosis. The modalities combined in their setup were Raman spectroscopy and autofluorescence microscopy in the incident light modes. Therefore, the possibility to connect two light sources to the incident light path of the microscope stand was taken. The excitation light for fluorescence microscopy was a UV lamp combined with a bandpass filter (450-490 nm) to narrow the spectral range of the excitation light. For Raman spectroscopy, a fibre-coupled 847 nm laser was used.

The 785 nm laser of the developed multimodal imaging system is vertically connected to the microscope stand via the interchangeable photo adapter tube. Such an

^f Parts of this chapter have been published in ¹.

arrangement is not meant to provide the adjustment of the laser light via the video capability. However, referencing the laser's vertical position with the aid of the microscope stage's height position is a suitable method. Thereby, the zero value of the stage is always referred to as the level where photographs are taken in the incident light bright-field mode using the BD50x objective. The additional light port in the incident light mode, which is not occupied in the developed multimodal imaging system, enables the use of the microscope stand's second light path for further retrofitting (see chapter 4.3).

Both setups have in common the pinhole fibre's core diameter of 100 μm to detect the inelastically scattered Raman light. While van de Poll et al.¹¹⁷ used an 80x NIR corrected microscope objective and a grid size of 1 μm , Raman measurements of the developed setup are performed with a BD50x objective and a step size of 5 μm (for the local scan). The step size of 5 μm is chosen based on the result (see Figure 16) of the lateral resolution for the 100 μm fibre.

The local scan results obtained from the configured Raman path show that detecting a blood vessel with a width in the x-direction of about 17 μm is possible. The fact that the blood vessel is highlighted by approximately four dark blue to black pixels in Figure 37 (2a) confirms the determined lateral resolution of the Raman path in the order of 5.2 μm . Consequently, the approach of Lasch and Naumann¹⁰³ to define a contrast value of 26.4% as the pertinent parameter of spatial resolution is appropriate. Experiments (Figure 31) show that the current microscope stage with a 2-phase stepper motor performs 5 μm increments (requirements of 100 μm fibre) with an average of 4.9 ± 0.6 μm over a scan range of 645 μm . Originally, this microscope stage was not designed for such precise applications. The datasheet of the microscope stage specifies the accuracy of ± 20 μm (measured according to VDI/DGQ 3441). To achieve more precise and reproducible results for step sizes in the low single-digit μm -range over the stage's entire travel area, the replacement of the microscope stage is advised. Anyhow, the decrease of the lateral resolution for Raman spectroscopy is recommended to match with the diffraction limit of the microscopic modalities (5x: 2.80 μm , BD20x: 0.67 μm). The extension of morphological information with chemical information is the significant advantage of multimodal imaging.

A reduction of the designed Raman path's spatial resolution would be achieved by decreasing the pinhole fibre's core diameter. The experiments (data not shown) for the lateral resolution indicate that the resolution using a 50 μm fibre is much lower than

6.8 μm (80 lp/mm), the highest spatial frequency on the resolution target. Besides the exchange of the microscope stage, higher intensities of the Raman signal are required when using smaller fibre diameters.

Independent on the fibre diameter, the increase of the Raman signal by optimisation of the light beam in the excitation path is worthwhile for the time-consuming Raman spectroscopy. The characteristics of the light sources (chapter 3.1.2) prove the loss of laser power at the objective with 74%. The investigation regarding the intensity distribution of the collimated laser beam shows a discrepancy to a Gaussian distribution (see Figure 27). To suppress spherical aberration, the replacement of the plano-convex lens by an aspherical lens is necessary. The requirement for the new lens is the collimation of the laser beam with a diameter larger than the objective's pupil lens. Both the Gaussian distribution of the laser's beam profile and a diameter that overfills the pupil lens's diameter lead to a diffraction-limited resolution of the laser beam. Since the beam profile of the present laser beam is not Gaussian distributed, it is expected that the lens exchange leads to a decrease in the laser spot. A smaller laser spot at a constant laser power results in higher light intensity at the sample surface and a reduction of the integration time.

The numerical aperture (NA) of the 80x NIR corrected microscope objective used by van de Poll et al.¹¹⁷ was not explained. Since the research group performed measurements without an immersion medium, it is expected that the NA is similar to 0.85, the NA of the BD50x objective. The grid size of 1 μm at a detection fibre of 100 μm suggests that the lateral resolution would decrease to a similar size when applying the beam modification by exchanging the lens in the excitation path of the adapted Raman path.

Moreover, van de Poll et al.¹¹⁷ used an NIR corrected objective. A wavelength-optimised coating of the microscope objective that increases the transmittance of the 785 nm excitation light is beneficial to perform Raman spectroscopy. An increase in laser intensity results in a higher Raman signal. Consequently, the integration time for spectra acquisition can be reduced.

Using an NIR corrected objective is also advantageous for NIR reflectance spectroscopy. Increasing light intensities in the NIR spectral region might reduce the integration time. Shorter integration times lower the photo response non-uniformity (PRNU), the fixed pattern (noise) of the extended indium gallium arsenide (InGaAs) detectors. A decrease in noise leads to an improved detection limit. Another possibility

at higher light intensity is the reduction of the fibre diameter for NIR reflectance spectroscopy. Spectra evaluation of the local scan (Figure 37 (2b)) shows that the 50 μm fibre cannot completely resolve the three air bubbles.

Regarding the evaluated reflectivity at 750 nm (Figure 37 (2a)) in the VIS spectral region, the three air bubbles with sizes between 9 μm and 16.0 μm are fully resolved. The higher lateral resolution in the VIS spectral range compared to the NIR spectral range follows the Rayleigh criterion. Regarding VIS reflectance spectroscopy, four blue pixels at the air bubble at the bottom right (diameter: 10 μm) with similar shades of blue surrounded by one pixel with a slightly higher intensity imply that the determined lateral resolution of approximately 7 μm is reliable. It has to be mentioned that the lateral resolution for VIS spectroscopy is determined at 580 nm and the value for the resolution increases (\triangleq resolution becomes poorer) with longer wavelengths. Anyhow, the lateral resolutions for reflectance spectroscopy are poorer than the microscope's diffraction limit. Therefore, a modification of the detection path for reflectance spectroscopy is required. This includes the reduction of the fibre diameter but also the increase in light intensity. Potentially, a confocal alignment of the optical components is mandatory.

Nevertheless, the designs of the newly added Raman and VIS/NIR reflectance paths enable an analysis of animal tissue.

4.2 Information content of the different modalities obtained from tissue analysis

All applied modalities are able to distinguish between GM and WM of mouse brain tissue. Based on the modality, different information content is provided. Bright-field and dark-field microscopy are complementary methods to display the morphological structure in the unstained tissue section. The information content of the sample's reflectivity at 750 nm is similar to the sample's appearance in the bright-field image. Therefore, the scanned location of the spectroscopic modalities can be visually determined within the scan area of the microscopic modalities by comparing the created image obtained from VIS spectroscopy and the bright-field image. Nevertheless, both modalities differ from each other regarding lateral resolution. The lateral resolution at 750 nm is in the order of 7 μm for the local scan. In contrast, the lateral resolution of the microscopic modalities is restricted by the diffraction limit, which is 0.7 μm for the BD20x objective. Moreover, the measurement techniques of both

modalities are different. While common colour cameras consist of three (red, green, blue) colour channels, spectrometers record hyperspectral data by assigning each intensity value to a wavelength. Besides the absorption of the microscope slide's gold coating, further absorption bands such as the haemoglobin-specific drops between 415 nm and 580 nm are not recorded in the VIS spectral range. Furthermore, a haemorrhage is neither detected as a reddish area within the photographs nor as a significant Raman peak at 1585 cm^{-1} . These observations confirm the quality of the tissue section's successful perfusion.

To validate the VIS reflectance spectroscopy, a second unstained tissue section with a haemorrhage (blood was not completely removed during the perfusion) is analysed. In addition to the VIS spectroscopy, bright-field microscopy and Raman spectroscopy are applied. All three modalities can highlight the oval shape of the haemorrhage within the scanned area. The absorbance spectrum of the haemorrhage (Figure 43) shows three characteristic peaks of haemoglobin. Since the haemorrhage contains most likely oxyhaemoglobin and deoxyhaemoglobin, the displayed absorbance spectrum is an overlap of both absorbance spectra. An indication is a double peak around 550 nm. The absorbance spectrum of oxyhaemoglobin forms two peaks around 550 nm that are clearly separated. The right peak of oxyhaemoglobin is at approximately 575 nm. Deoxyhaemoglobin is characterised by an absorbance spectrum with a single peak at 555 nm. An overlap of the two absorbance spectra results in a shift of the 575 nm peak to shorter wavelengths and a weaker drop between the double peak.

Using GM intensity spectrum without haemorrhage as a reference spectrum is beneficial to calculate the absorbance spectra. The Zenith Polymer[®] does not compensate for the absorbance properties of gold. Using the gold spectrum for reference is impossible since the gold coating's specular reflection varies for the microscope stage's height positions. The location of the proper height position that corresponds to the intensity spectrum with the $16\text{ }\mu\text{m}$ tissue sample is infeasible.

To record the Raman spectra, the laser power is reduced to 200 mW to prevent photodamage. The decrease in laser power results in an increase in integration time to 10 s per pixel. The chosen integration time of 10 s at 200 mW results in the identical heat input as 4 s at 500 mW for the distinction between GM and WM. Because of the same heat input, the signal intensities of the detected Raman spectra obtained from GM are similar. However, the intensity of the Raman spectrum of the haemorrhage (Figure 44) is significantly higher compared to GM. The strong and unique Raman

signal of haemoglobin was already reported by Kast et al.⁴⁷ In their studies, the Raman peak at 1585 cm^{-1} was used to localise haemoglobin in different types of brain tissue. The identical Raman peak is successfully used in this study to create an image to visualise the location of the haemorrhage.

Although the Raman measurements meet the maximum recommended accumulation time of 10 s per pixel to perform a tissue scan in a reasonable time,⁵¹ it is advised to record bright-field photographs at first. Besides the determination of a region of interest (ROI), bright-field photographs can be used to identify the presence of haemoglobin. If haemoglobin is present in the ROI, the setup parameter laser power and integration time must be adjusted. In addition to the haemoglobin peak, the Raman spectrum comprises further molecular information. The VIS reflectance spectrum complements the bright-field image obtained with the colour camera by information regarding the haemoglobin states (oxyhaemoglobin, deoxyhaemoglobin). Anyhow, as mentioned several times, the resolutions of the microscopic modalities are better than the lateral resolutions of the spectroscopic modalities. Therefore, incident light bright-field microscopy is preferred over the VIS reflectance spectroscopy at the present time.

Analogue to the VIS reflectance spectra for the distinction between GM and WM, the NIR reflectance spectra does not detect molecular-specific absorption bands.

Water is the main absorber in the NIR wavelength range, with prominent absorption bands at 1450 nm and 1930 nm. The water's high absorbances usually superimpose weaker absorption bands of the tissue originating from biomolecules such as lipids, proteins, and collagen.²²

The proof-of-concept shows that the configured NIR setup can detect absorption bands in muscle tissue of Serrano ham originating from water. Even the detection of the lipid's CH stretching mode in the ham's fat rind is possible. However, the calculation shows that the brain section's thickness of $16\text{ }\mu\text{m}$ is insufficient to detect the absorption band of lipids at 1730 nm. In contrast, the minimum water content of 23% can be verified by evaluating the absorption peak around 1930 nm. GM and WM differ from each other regarding their water content. In normal brain tissue, the water content is 83% in GM and 70% in WM.⁶⁶ The fact that the designed NIR path does not detect water of the $16\text{ }\mu\text{m}$ thin tissue section indicates that the water of the tissue section is evaporated. Recording NIR spectra immediately after the determination of an ROI based on the bright-field photographs (Table 4, scan no.2) does not result in water detection. Therefore, it must be assumed that the thawing from $-20\text{ }^{\circ}\text{C}$ to room temperature and

the exposure with the halogen lamp dehydrate the tissue. Investigations of Kümmel (personal communication) confirm this assumption. A 10 μm tissue section on a MirrIR low-e microscope slide (Kevley Technologies, Chesterland, OH, USA) at an aluminium sample holder required approximately 1.5 min to dehydrate. Moreover, Krafft and Popp³⁷ reported a successful fixation of thin sections by air drying due to water vaporisation.

Moreover, it should be considered that tissue drying may result in a small height difference between GM and WM because of different water content in both brain regions.⁵⁹ As a consequence, GM would become thinner than WM. This results in the detection of higher intensity spectra in WM. To exclude that this conjecture applies to the obtained spectra, the height profile of the tissue section, including the smaller ROI of the local scan, is recorded. Therefore, the digital microscope VHX-7000 (Keyence Deutschland GmbH, Neu-Isenburg, Germany) is used. The result is illustrated in Figure 48).

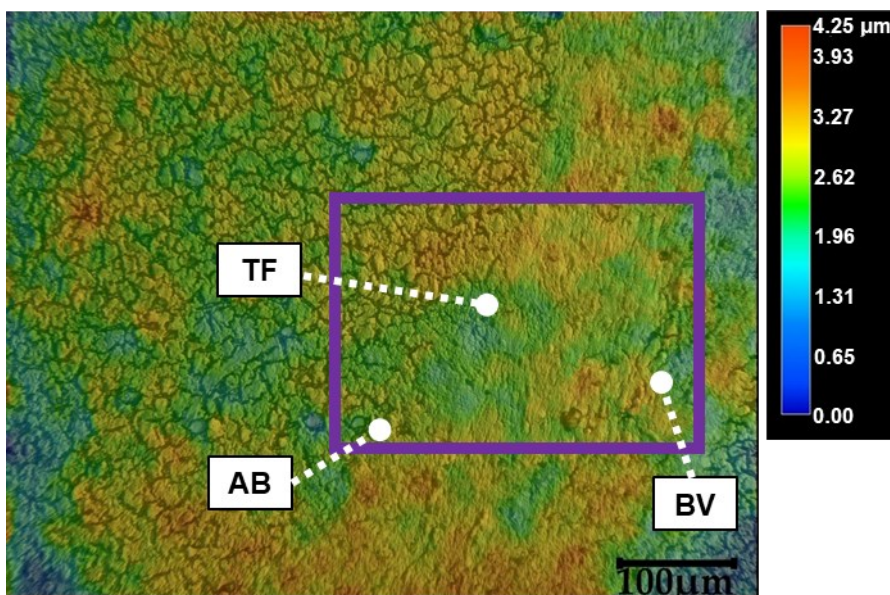


Figure 48 Colour map including height scale of an unstained tissue section's height profile (magnification: 500x). The purple rectangle frames the area of the smaller ROI recorded with the spectroscopic modalities. Abbreviations: AB: air bubbles, BV: blood vessel, TF: tissue fold (see text for details)¹

The colourisation of the heightmap does not show a correlation between the height and the tissue type. For this reason, the created images of the reflectivity in the VIS and NIR spectral region (Figure 37 (2a, 2b)) visualise tissue characteristics instead of physical properties. The same applies to the Raman spectra. Consequently, the chemical information obtained from Raman spectra is rated as reliable.

The colour coding of the created Raman image (Figure 37 (2c)) agrees with the literature.^{46,47} The detection of higher intensity peak ratios in WM is confirmed by observations of Mizuno⁴⁶ and Kast⁴⁷, where the lipid peak was in the numerator.

The position of the detected Raman peaks is in good accordance with literature values (Table 5). However, a shift of the Raman peak positions is recognised for optimal cutting temperature (OCT). Peaks below Raman shifts of 1400 cm^{-1} are shifted to higher wavenumbers, whereas peaks above 1400 cm^{-1} are shifted to lower wavenumbers. This is indicative of the interfering fluorescence signal of the microscope slide's glass substrate. A shift in wavenumbers is not observed for Raman spectra obtained from GM and WM. For this reason, it is assumed that the optical properties of the tissue primarily scatter and absorb the laser light.

Nevertheless, the developed Raman path can distinguish between GM and WM based on differences regarding variations in the lipid and protein content. The local scan achieved good results for spectra evaluation in the high-wavenumber region (Figure 37 (2d, 3d)). The yellow and reddish pixels in Figure 37 (2d) represent high values. The colour labelling of the pixels is in good accordance with early observations of Mizuno et al.⁴⁶ on rat brain tissues. While the peak at 2938 cm^{-1} was high in all brain tissues, the researchers determined an increase in the peaks at 2852 cm^{-1} and 2885 cm^{-1} in the WM and the myelin fraction. In 2018, Ji et al.¹¹⁸ identified the CH_2 stretching mode of lipids peaking around 2850 cm^{-1} as an indicator to localise myelinated axons. The pixel location of the highest values (yellow pixels) in Figure 37 (2d), where the peak at 2850 cm^{-1} is in the numerator, and the pixel location of the lowest values (bright blue pixels) in Figure 37 (3d), where the peak at 2850 cm^{-1} is in the denominator, coincide with the location of the WM's blue pigmentation in the image (Figure 37 (1d)) obtained from polarisation microscopy with the activated whole-wave compensator (WWC). The blue pigmentation within the image suggests a higher density of myelinated axons. In contrast, orange areas are primarily present in the internal capsule, where the density of myelinated axons is usually lower. Such a colour differentiation is not achieved for polarisation microscopy without the WWC. Moreover, this microscopic modality requires triple integration time. Consequently, the activation of the WWC for polarisation microscopy is favourable.

A further advantage of the setup is the gold-coating of the microscope slide. Besides contrast enhancement of the bright-field images, Raman spectroscopy benefits from the reflective layer since the excitation laser passes through the tissue twice. The

integration time of 4 s per pixel for the global and local scan does not cause tissue damage (Figure 38). Furthermore, the integration time results in a sufficient signal-to-noise ratio (SNR) to evaluate various peak ratios of the detected Raman spectra. However, the scanned area of the global scan for Raman spectroscopy but also for the other spectroscopic modalities is undersampled at a step size of 200 μm . Additionally, the OCT interferes with the spectra evaluation of the Raman signal in the high-wavenumber region (Figure 34 (2d)). The results of the local scan at a step size of 5 μm are much better. A distinction between GM and WM is clearly visible in the entirety of the created Raman images (Figure 37 (2c, 2d, 3a-d)).

With respect to a sufficient SNR, spectra evaluation of the Raman intensities at 1444 cm^{-1} and 1660 cm^{-1} (Figure 41) obtained from a tissue scan with an integration time of 1 s is also suitable to differentiate between GM and WM. For subsequent applications, it has to be taken into account that reducing the integration time limits the evaluable Raman peaks.

Anyway, due to the long integration time per pixel, applying the spectroscopic modalities exclusively to scan a designated ROI is advised.

To get an overview of the sample and determine ROI, the microscopic-based modalities of the multimodal imaging system are recommended. The subsequent combination of the various images of the unstained sample with the image of the haematoxylin and eosin (H&E)-stained sample raise the information content obtained from the measuring sample. The H&E stained sample is also suited to develop and validate Raman-based classification models.¹¹ As expected, the H&E-stained images of the healthy brain tissue in this study do not show abnormalities concerning the cellular structure.

4.3 Outlook

To compare the images of the H&E-stained tissue section one-to-one with the images of the unstained tissue section obtained from the different modalities in the incident light mode, the images must have identical pixel resolution. One possibility is the recording of the photographs in the transmitted light mode (stained sections) with the BD20x objective. This requires only the activation of the condenser in the excitation path and the adjustment of the illumination (Köhler illumination). The photographing in the transmitted mode is naturally not limited to H&E-stained samples. Any staining with

standardised dyes or histochemical methods is feasible. Regarding the observation of myelin in brain tissue, the luxol fast blue (LFB) stain is commonly used. Kast et al.⁴⁸ complemented H&E-stained tissue sections by LFB-stained tissue sections to analyse unstained brain sections with Raman spectroscopy.

Concerning the actual lateral resolution of the developed Raman path, the data acquisition of the photographs with the 5x objective is advised. The diffraction limit of 2.8 μm matches the resolution of the spectroscopic modalities rather than the BD20x diffraction limit (0.67 μm). Although the 5x objective is not designed for dark-field microscopy, the objective can be utilised for polarisation microscopy. This is advantageous since polarisation microscopy with the activated WWC provides good results, additionally to Raman spectroscopy.

In any case, the Raman path has the potential for improvement. As already mentioned in chapter 4.1, the beam profile of the laser has to be modified to a Gaussian distribution. This results in higher intensity and a smaller spot size of the laser light. The replacement of the microscope objective by an NIR corrected objective is also beneficial regarding light intensity. For applications of dehydrated measurement samples, where NIR spectroscopy does not provide additional information, it is worth considering using a water immersion objective. Water only slightly interferes with the Raman spectrum because of the water molecule's polarity. Moreover, the water's refractive index of 1.33 is similar to the refractive index of brain tissue ($\sim 1.37\text{-}1.41$ ¹⁰⁹). This results in an increase in depth resolution and a reduction of the background signal. Bonnier et al.⁵¹ analysed human skin tissue by Raman microscopy at various wavelengths and different objectives. Regarding the 785 nm laser, the background signal of the Raman spectra was significantly decreased when immersing the section in water compared to a dry section.⁵¹

The immersion objective's higher numerical aperture lowers the spot size additionally. Again, an alignment of the modalities lateral resolutions is worthwhile for directly comparing certain images and image stacking. Additional data processing with machine learning methods (k-means, k-nearest neighbours, and convolutional neural networks) opens up new possibilities for further applications with the multimodal imaging system. The applications are not restricted to distinguishing between GM and WM, although structural changes within the brain regions are indicative of HIV, Alzheimer's disease, and multiple sclerosis. Larraona-Puy et al.¹¹⁹ used peak ratios of Raman intensities to discriminate between basal cell carcinoma and hair follicles.

Due to the long integration time for spectra recording with Raman spectroscopy, the application for real-time analysis of cryosections during surgeries is not recommended. Anyhow, ex-vivo applications of any tissue section for research and diagnostic purposes are feasible.

The expansion of the microscopy by further modalities is also possible. Epifluorescence microscopy is a promising technique for detecting autofluorescence in the tissue section or analysing fluorescence labelled targets. The light source (mercury lamp) can be easily adapted to the additional light port in the incident light path. The space for the required switchable deviating mirror and filters is already provided in the microscope stand. The detection of the fluorescence emission is identical to the other microscopic modalities in the incident light mode. Images are recorded via the colour camera at the sidewise port of the interchangeable photo adapter tube. The adaption of further microscopic modalities for tissue analysis, such as phase-contrast microscopy or interference microscopy, is not intended since these microscopic modalities are recommended for the analysis of cells.⁴⁰ Because the Leica DM R microscope is a light microscope, it is assumed that the installed optics are primarily designed for the VIS spectral range. These materials usually absorb light in the infrared (IR) spectral region. An indicator is the lowering of the long-wavelength intensity in NIR spectroscopy. Therefore, adopting IR spectroscopy, the complementary method of Raman spectroscopy, is not feasible.

4.4 Conclusion

The designed multimodal imaging system is an all-in-one solution that is successfully applied to differentiate GM and WM of healthy mouse brain tissue. While the bright-field images of the H&E-stained tissue section highlight differences regarding the brain's cellular structure, bright-field and dark-field microscopy are complementary imaging modalities that emphasise the morphology of the unstained tissue section in the incident light mode.

Information on the sample's surface characteristics is obtained with VIS and NIR reflectance spectroscopy. The potential of the VIS spectrometer to collect hyperspectral data compared to the colour camera is confirmed for the detection of haemoglobin in haemorrhage. The capability of the NIR path to detect water and lipids is demonstrated on Serrano ham. Due to the absence of water in the brain section, the

characteristic absorption bands of water at 1450 nm and 1930 nm do not exist in the detected NIR spectra of the brain section. However, an extrapolation results in detectable water concentrations of a minimum of 23%. The PRNU of the extended InGaAs detector combined with an inappropriate reference spectrum for the calculation of the reflectivities and the absorbances leads to a spectral noise that prevents the detection of lipids in 16 μm thin tissue sections.

Molecular-specific information of the tissue section is obtained from Raman spectroscopy. Since GM and WM differ regarding the lipid and protein concentration, peak ratios and the sum of two peak ratios of peaks assigned to lipids and proteins are suitable to distinguish between the two brain regions. For the global scan, the side component OCT has to be taken into account. The best result for differentiation of the three analytes (GM, WM, OCT) is achieved by a peak ratio of intensities in the fingerprint region (I_{1444}/I_{1660}). For the local scan, the identical peak ratio enables the emphasis of tissue structures such as a tissue fold and a blood vessel, in addition to the differentiation of GM and WM. Furthermore, it is proven that one-quarter (1 s) of the initial integration time (4 s) is sufficient to distinguish between GM and WM. A second evaluation method ($(I_{2857} + I_{2888})/I_{2930}$) in the high-wavenumber region also facilitates the discrimination of the blood vessel. Additionally to identifying the tissue structure and the differentiation between GM and WM, the evaluation of the sum of two intensity peak ratios enables the visualisation of differences in the density of myelinated axons within WM. The created image matched the stitched image obtained with polarisation microscopy at the activated WWC.

In the future, the exchange of the microscope stage and minor modifications in the excitation path for Raman spectroscopy are recommended to be competitive.

Regarding further applications, it is advised to use images of the stained and unstained sample obtained from the microscopic modalities, especially the bright-field and polarisation microscopy, to get an overview of the measurement sample and determine ROIs. In particular, the time-consuming but molecular specific Raman spectroscopy should be applied exclusively to these designated areas to create images to study the sample's molecular structure.

5 SUMMARY⁹

The focus of this study is on the design of a novel multimodal imaging system for tissue analysis that combines light microscopy and optical spectroscopy. The centrepiece of the setup is a modular light microscope. The special feature of the microscope is the operation in the incident and transmitted light mode. The microscopic modalities in the incident light mode are bright-field, dark-field, and polarisation microscopy. The newly adapted spectroscopic modalities are visible (VIS) and near-infrared (NIR) reflectance spectroscopy, and Raman spectroscopy in the incident light mode. The modalities in the incident light mode are intended for data acquisition of unstained tissue sections. Data acquisition is complemented by bright-field photographs of a stained tissue section obtained in the transmitted light mode.

A first application is performed to distinguish between grey matter (GM) and white matter (WM) of an unstained and a haematoxylin and eosin (H&E)-stained tissue section of a healthy mouse brain. Two measurement sets are performed, a global scan with a step size of 200 μm and a local scan of a smaller area with a step size of 5 μm for the spectroscopic modalities. All modalities (microscopic and spectroscopic) are successfully applied to distinguish between GM and WM of ex-vivo brain tissue. Data evaluation of the various modalities results in different information content. The best results for the unstained tissue section are obtained for polarisation microscopy and Raman spectroscopy in the high-wavenumber region. Both modalities also highlight differences in the density of myelinated axons.

Supplementary tissue experiments prove the capability of the design of the VIS and NIR reflectance path to detect haemoglobin and water, respectively.

Investigations on the setup of the developed multimodal imaging system result, amongst others, in a lateral resolution of approximately 5 μm at best for the spectroscopic modalities. A device that restricts the lateral resolution is the microscope stage.

To compete with other Raman microscopes for tissue analysis, the lateral resolution has to be increased to 1 μm without increasing the integration time. Potential modifications of the Raman path and the multimodal setup are proposed.

⁹ Parts of this chapter have been published in ¹.

6 REFERENCES

1. Heintz A, Sold S, Wühler F, Dyckow J, Schirmer L, Beuermann T et al.: Design of a Multimodal Imaging System and Its First Application to Distinguish Grey and White Matter of Brain Tissue. A Proof-of-Concept-Study. *Appl Sci (Basel)* 11: 4777, 2021. doi:10.3390/app11114777
2. Jelínková H (ed): *Lasers for medical applications: Diagnostics, therapy and surgery*. Cambridge, Woodhead Publishing Ltd., 2013.
3. Kong K, Kendall C, Stone N, Notingher I: Raman spectroscopy for medical diagnostics – From in-vitro biofluid assays to in-vivo cancer detection. *Adv Drug Deliv Rev* 89: 121–34, 2015. doi:10.1016/j.addr.2015.03.009
4. Rehman Iu, Movasaghi Z, Rehman S: *Vibrational spectroscopy for tissue analysis*. Boca Raton, CRC Press, 2013.
5. Braun F: *Krebserkennung durch multispektrale Gewebeuntersuchung* Dissertation. Medizinische Fakultät Mannheim, Universität Heidelberg, 2019. doi:10.11588/heidok.00026082
6. Braun F, Schalk R, Nachtmann M, Hien A, Frank R, Beuermann T et al.: A customized multispectral needle probe combined with a virtual photometric setup for in vivo detection of Lewis lung carcinoma in an animal model. *Meas Sci Technol* 30: 104001, 2019. doi:10.1088/1361-6501/ab24a1
7. Braun F, Schalk R, Heintz A, Feike P, Firmowski S, Beuermann T et al.: NADH-fluorescence scattering correction for absolute concentration determination in a liquid tissue phantom using a novel multispectral magnetic-resonance-imaging-compatible needle probe. *Meas Sci Technol* 28: 75903, 2017. doi:10.1088/1361-6501/aa743e
8. Braun F, Heintz A, Schalk R, Beuermann T, Gretz N, Rädle M: NADH-fluorescence absorption correction to determine absolute fluorophore concentrations of a liquid tissue model. *Meas Sci Technol* 29: 107001, 2018. doi:10.1088/1361-6501/aad875
9. Krafft C, Dochow S, Latka I, Dietzek B, Popp J: Diagnosis and screening of cancer tissues by fiber-optic probe Raman spectroscopy. *Biomed Spectrosc Imaging* 1: 39–55, 2012. doi:10.3233/BSI-2012-0004
10. Lu G, Fei B: Medical hyperspectral imaging: a review. *J Biomed Opt* 19: 10901, 2014. doi:10.1117/1.JBO.19.1.010901

11. Krafft C, Schmitt M, Schie IW, Cialla-May D, Matthäus C, Bocklitz T et al.: Label-Free Molecular Imaging of Biological Cells and Tissues by Linear and Nonlinear Raman Spectroscopic Approaches. *Angew Chem Int Ed Engl* 56: 4392–430, 2017. doi:10.1002/anie.201607604
12. Vogler N, Heuke S, Bocklitz TW, Schmitt M, Popp J: Multimodal Imaging Spectroscopy of Tissue. *Annual review of analytical chemistry (Palo Alto, Calif.)* 8: 359–87, 2015. doi:10.1146/annurev-anchem-071114-040352
13. Schmidt W: *Optische Spektroskopie*. Weinheim, Wiley-VCH, 2000.
14. Liedtke S, Popp J: *Laser, Licht und Leben: Techniken in der Medizin*. Weinheim, Wiley-VCH, 2006.
15. Lambert JB, Gronert S, Shurvell HF, Lightner DA: *Spektroskopie: Strukturaufklärung in der organischen Chemie*. München, Harlow, Amsterdam, Madrid, Boston, San Francisco, Don Mills, Mexico City, Sydney, Pearson Higher Education a part of Pearson plc worldwide, 2012.
16. Sikurova L, Balis P, Zvarik M: Penetration of laser light through red blood cell ghosts. *J Photochem Photobiol B* 103: 230–3, 2011. doi:10.1016/j.jphotobiol.2011.03.015
17. Hof M, Macháň R: Basics of Optical Spectroscopy. In: *Handbook of spectroscopy*, edited by Gauglitz G, Moore DS, Weinheim, Wiley-VCH. 2014, pp 31–38
18. Dobrucki JW, Kubitscheck U: Fluorescence Microscopy. In: *Fluorescence microscopy: From principles to biological applications*, edited by Kubitscheck U, Weinheim, Wiley-VCH. 2017, pp 85–132
19. Wagnieres GA, Star WM, Wilson BC: In Vivo Fluorescence Spectroscopy and Imaging for Oncological Applications. *Photochem Photobiol* 68: 603–32, 1998. doi:10.1111/j.1751-1097.1998.tb02521.x
20. Nienhaus GU, Nienhaus K: Fluorescence Labeling. In: *Fluorescence microscopy: From principles to biological applications*, edited by Kubitscheck U, Weinheim, Wiley-VCH. 2017, pp 133–164
21. Golovynskyi S, Golovynska I, Stepanova LI, Datsenko OI, Liu L, Qu J et al.: Optical windows for head tissues in near-infrared and short-wave infrared regions: Approaching transcranial light applications. *J Biophotonics* 11: e201800141, 2018. doi:10.1002/jbio.201800141
22. Sanchez-Cano A, Saldaña-Díaz JE, Perdices L, Pinilla I, Salgado-Remacha FJ, Jarabo S: Measurement method of optical properties of ex vivo biological tissues

- of rats in the near-infrared range. *Appl Opt* 59: D111-D117, 2020.
doi:10.1364/AO.384614
23. Günzler H, Gremlich H-U: *IR-Spektroskopie*. Weinheim, Wiley-VCH, 2003.
24. Kessler RW: Optische Spektroskopie: Hardware für die Prozessanalytik. In: *Prozessanalytik: Strategien und Fallbeispiele aus der industriellen Praxis*, edited by Kessler RW, Weinheim, Wiley-VCH. 2006, pp 229–253
25. Pacheco-Londoño LC, Castro-Suarez JR, Galán-Freyte NJ, Figueroa-Navedo AM, Ruiz-Caballero JL, Infante-Castillo R et al.: Mid-Infrared Laser Spectroscopy Applications I: Detection of Traces of High Explosives on Reflective and Matte Substrates. In: *Infrared Spectroscopy - Principles, Advances, and Applications*, edited by El-Azazy M, IntechOpen. 2019
26. Kümmel T, van Marwick B, Rittel M, Ramallo Guevara C, Wühler F, Teumer T et al.: Rapid brain structure and tumour margin detection on whole frozen tissue sections by fast multiphotometric mid-infrared scanning. *Sci Rep* 11: 11307, 2021.
doi:10.1038/s41598-021-90777-4
27. Steiner G: Infrared and Raman Spectroscopic Imaging. In: *Biomedical imaging: Principles and applications*, edited by Salzer R, Hoboken, N.J., J. Wiley & Sons. 2011, 275-303
28. Jones RR, Hooper DC, Zhang L, Wolverson D, Valev VK: Raman Techniques: Fundamentals and Frontiers. *Nanoscale Res Lett* 14: 231, 2019.
doi:10.1186/s11671-019-3039-2
29. Smekal A: Zur Quantentheorie der Dispersion. *Naturwissenschaften* 11: 873–5, 1923. doi:10.1007/BF01576902
30. Raman CV, Krishnan KS: A New Type of Secondary Radiation. *Nature* 121: 501–2, 1928. doi:10.1038/121501c0
31. Butler HJ, Ashton L, Bird B, Cinque G, Curtis K, Dorney J et al.: Using Raman spectroscopy to characterize biological materials. *Nat Protoc* 11: 664–87, 2016.
doi:10.1038/nprot.2016.036
32. Hollricher O: Raman Instrumentation for Confocal Raman Microscopy. In: *Confocal Raman microscopy*, edited by Dieing T, Hollricher O, Toporski J, Berlin, Springer. 2010, pp 43–60
33. Kiselev R, Schie IW, Aškrić S, Krafft C, Popp J: Design and first applications of a flexible Raman micro-spectroscopic system for biological imaging. *Biomed Spectrosc Imaging* 5: 115–27, 2016. doi:10.3233/BSI-160141

34. Diem M, Mazur A, Lenau K, Schubert J, Bird B, Miljković M et al.: Molecular pathology via IR and Raman spectral imaging. *J Biophotonics* 6: 855–86, 2013. doi:10.1002/jbio.201300131
35. Aubertin K, Desroches J, Jermyn M, Trinh VQ, Saad F, Trudel D et al.: Combining high wavenumber and fingerprint Raman spectroscopy for the detection of prostate cancer during radical prostatectomy. *Biomed Opt Express* 9: 4294–305, 2018. doi:10.1364/BOE.9.004294
36. Palonpon AF, Sodeoka M, Fujita K: Molecular imaging of live cells by Raman microscopy. *Curr Opin Chem Biol* 17: 708–15, 2013. doi:10.1016/j.cbpa.2013.05.021
37. Krafft C, Popp J: Vibrational Spectroscopic Imaging of Soft Tissue. In: *Infrared and Raman spectroscopic imaging*, 2nd ed., edited by Salzer R, Siesler HW, Weinheim, Wiley-VCH. 2014, pp 113–152
38. Lin S-Y, Li M-J, Cheng W-T: FT-IR and Raman vibrational microspectroscopies used for spectral biodiagnosis of human tissues. *J Spectrosc (Hindawi)* 21: 1–30, 2007. doi:10.1155/2007/278765
39. Cicchi R, Pavone FS: Multimodal Morphochemical Tissue Imaging. In: *Ex-vivo and In-vivo Optical Molecular Pathology*, edited by Popp J, Weinheim, Wiley-Blackwell. 2014, pp 147–177
40. Welsch U: *Sobotta Lehrbuch Histologie: Zytologie, Histologie, mikroskopische Anatomie*. München, Elsevier Urban & Fischer, 2006.
41. Mireskandari M, Petersen I: Clinical Pathology. In: *Ex-vivo and In-vivo Optical Molecular Pathology*, edited by Popp J, Weinheim, Wiley-Blackwell. 2014, pp 1–26
42. Delhaye M, Dhamelin court P: Raman microprobe and microscope with laser excitation. *J Raman Spectrosc* 3: 33–43, 1975. doi:10.1002/jrs.1250030105
43. Hollricher O, Ibach W: High-Resolution Optical and Confocal Microscopy. In: *Confocal Raman microscopy*, edited by Dieing T, Hollricher O, Toporski J, Berlin, Springer. 2010, pp 1–20
44. Vandenaabeele P: *Practical Raman spectroscopy: An introduction*. Chichester, Wiley, 2013.
45. Brozek-Pluska B, Kopec M: Raman microspectroscopy of Hematoporphyrins. Imaging of the noncancerous and the cancerous human breast tissues with

- photosensitizers. *Spectrochim Acta A Mol Biomol Spectrosc* 169: 182–91, 2016. doi:10.1016/j.saa.2016.06.038
46. Mizuno A, Hayashi T, Tashibu K, Maraishi S, Kawauchi K, Ozaki Y: Near-infrared FT-Raman spectra of the rat brain tissues. *Neurosci Lett* 141: 47–52, 1992. doi:10.1016/0304-3940(92)90331-Z
47. Kast RE, Auner GW, Rosenblum ML, Mikkelsen T, Yurgelevic SM, Raghunathan A et al.: Raman molecular imaging of brain frozen tissue sections. *J Neurooncol* 120: 55–62, 2014. doi:10.1007/s11060-014-1536-9
48. Kast R, Auner G, Yurgelevic S, Broadbent B, Raghunathan A, Poisson LM et al.: Identification of regions of normal grey matter and white matter from pathologic glioblastoma and necrosis in frozen sections using Raman imaging. *J Neurooncol* 125: 287–95, 2015. doi:10.1007/s11060-015-1929-4
49. Brozek-Pluska B, Musial J, Kordek R, Abramczyk H: Analysis of Human Colon by Raman Spectroscopy and Imaging—Elucidation of Biochemical Changes in Carcinogenesis. *Int J Mol Sci* 20, 2019. doi:10.3390/ijms20143398
50. Ali SM, Bonnier F, Tfayli A, Lambkin H, Flynn K, McDonagh V et al.: Raman spectroscopic analysis of human skin tissue sections ex-vivo: evaluation of the effects of tissue processing and dewaxing. *J Biomed Opt* 18: 61202, 2013. doi:10.1117/1.JBO.18.6.061202
51. Bonnier F, Ali SM, Knief P, Lambkin H, Flynn K, McDonagh V et al.: Analysis of human skin tissue by Raman microspectroscopy: Dealing with the background. *Vib Spectrosc* 61: 124–32, 2012. doi:10.1016/j.vibspec.2012.03.009
52. Bonnier F, Mehmood A, Knief P, Meade AD, Hornebeck W, Lambkin H et al.: In vitro analysis of immersed human tissues by Raman microspectroscopy. *J Raman Spectrosc* 42: 888–96, 2011. doi:10.1002/jrs.2825
53. Wang S, Liang Z, Gong Y, Yin Y, Wang K, He Q et al.: Confocal raman microspectral imaging of ex vivo human spinal cord tissue. *J Photochem Photobiol B* 163: 177–84, 2016. doi:10.1016/j.jphotobiol.2016.08.032
54. Li J, Liang Z, Wang S, Wang Z, Zhang X, Hu X et al.: Study on the pathological and biomedical characteristics of spinal cord injury by confocal Raman microspectral imaging. *Spectrochim Acta A Mol Biomol Spectrosc* 210: 148–58, 2019. doi:10.1016/j.saa.2018.11.022
55. Tuck M, Blanc L, Touti R, Patterson NH, van Nuffel S, Villette S et al.: Multimodal Imaging Based on Vibrational Spectroscopies and Mass Spectrometry Imaging

- Applied to Biological Tissue: A Multiscale and Multiomics Review. *Anal Chem* 93: 445–77, 2021. doi:10.1021/acs.analchem.0c04595
56. Haus J: *Optische Mikroskopie: Funktionsweise und Kontrastierverfahren*. Weinheim, Wiley-VCH, 2014.
57. Cheng P-C: The Contrast Formation in Optical Microscopy. In: *Handbook of biological confocal microscopy*, edited by Pawley JB, New York, NY, Springer. 2006, pp 162–206
58. Das NK, Dai Y, Liu P, Hu C, Tong L, Chen X et al.: Raman Plus X: Biomedical Applications of Multimodal Raman Spectroscopy. *Sensors (Basel)* 17, 2017. doi:10.3390/s17071592
59. Kochan K, Chrabaszcz K, Szczur B, Maslak E, Dybas J, Marzec KM: IR and Raman imaging of murine brains from control and ApoE/LDLR(-/-) mice with advanced atherosclerosis. *Analyst* 141: 5329–38, 2016. doi:10.1039/c6an00107f
60. Gajjar K, Heppenstall LD, Pang W, Ashton KM, Trevisan J, Patel II et al.: Diagnostic segregation of human brain tumours using Fourier-transform infrared and/or Raman spectroscopy coupled with discriminant analysis. *Anal Methods* 5: 89–102, 2012. doi:10.1039/c2ay25544h
61. Bunaciu AA, Hoang VD, Aboul-Enein HY: Vibrational Micro-Spectroscopy of Human Tissues Analysis: Review. *Crit Rev Anal Chem* 47: 194–203, 2017. doi:10.1080/10408347.2016.1253454
62. Lasch P, Noda I: Two-Dimensional Correlation Spectroscopy for Multimodal Analysis of FT-IR, Raman, and MALDI-TOF MS Hyperspectral Images with Hamster Brain Tissue. *Anal Chem* 89: 5008–16, 2017. doi:10.1021/acs.analchem.7b00332
63. Patil CA, Bosschaart N, Keller MD, van Leeuwen TG, Mahadevan-Jansen A: Combined Raman spectroscopy and optical coherence tomography device for tissue characterization. *Opt Lett* 33: 1135–7, 2008
64. Egodage K, Dochow S, Bocklitz T, Chernavskaja O, Matthaeus C, Schmitt M et al.: The combination of optical coherence tomography and Raman spectroscopy for tissue characterization. *J Biomed Photonics Eng*: 169–77, 2015. doi:10.18287/jbpe-2015-1-2-169
65. Bocklitz TW, Salah FS, Vogler N, Heuke S, Chernavskaja O, Schmidt C et al.: Pseudo-HE images derived from CARS/TPEF/SHG multimodal imaging in

- combination with Raman-spectroscopy as a pathological screening tool. *BMC cancer* 16: 534, 2016. doi:10.1186/s12885-016-2520-x
66. Krafft C, Sergo V: Biomedical applications of Raman and infrared spectroscopy to diagnose tissues. *J Spectrosc* 20: 195–218, 2006. doi:10.1155/2006/738186
67. Sanchez-Molina P, Kreuzer M, Benseny-Cases N, Valente T, Almolda B, González B et al.: From Mouse to Human: Comparative Analysis between Grey and White Matter by Synchrotron-Fourier Transformed Infrared Microspectroscopy. *Biomolecules* 10: 1099, 2020. doi:10.3390/biom10081099
68. Beljebbar A, Dukic S, Amharref N, Manfait M: Ex vivo and in vivo diagnosis of C6 glioblastoma development by Raman spectroscopy coupled to a microprobe. *Anal Bioanal Chem* 398: 477–87, 2010. doi:10.1007/s00216-010-3910-6
69. Ji M, Orringer DA, Freudiger CW, Ramkissoon S, Liu X, Lau D et al.: Rapid, label-free detection of brain tumors with stimulated Raman scattering microscopy. *Sci Transl Med* 5: 201ra119, 2013. doi:10.1126/scitranslmed.3005954
70. Krafft C, Belay B, Bergner N, Romeike BFM, Reichart R, Kalff R et al.: Advances in optical biopsy – correlation of malignancy and cell density of primary brain tumors using Raman microspectroscopic imaging. *Analyst* 137: 5533–7, 2012. doi:10.1039/c2an36083g
71. Amharref N, Beljebbar A, Dukic S, Venteo L, Schneider L, Pluot M et al.: Discriminating healthy from tumor and necrosis tissue in rat brain tissue samples by Raman spectral imaging. *Biochim Biophys Acta Biomembr* 1768: 2605–15, 2007. doi:10.1016/j.bbamem.2007.06.032
72. Koljenović S, Choo-Smith L-P, Bakker Schut TC, Kros JM, van den Berge HJ, Puppels GJ: Discriminating vital tumor from necrotic tissue in human glioblastoma tissue samples by Raman spectroscopy. *Lab Invest* 82: 1265–77, 2002. doi:10.1097/01.LAB.0000032545.96931.B8
73. Koljenović S, Bakker Schut TC, Wolthuis R, Jong B de, Santos L, Caspers PJ et al.: Tissue characterization using high wave number Raman spectroscopy. *J Biomed Opt* 10: 31116, 2005. doi:10.1117/1.1922307
74. Tuschel D: Selecting an Excitation Wavelength for Raman Spectroscopy. In: *Molecular Spectroscopy Workbench: The 2016 Collection*, edited by Spectroscopy, UBM. 2016, pp 11–17

75. Cui L, Butler HJ, Martin-Hirsch PL, Martin FL: Aluminium foil as a potential substrate for ATR-FTIR, transfection FTIR or Raman spectrochemical analysis of biological specimens. *Anal Methods* 8: 481–7, 2016. doi:10.1039/c5ay02638e
76. Fullwood LM, Griffiths D, Ashton K, Dawson T, Lea RW, Davis C et al.: Effect of substrate choice and tissue type on tissue preparation for spectral histopathology by Raman microspectroscopy. *Analyst* 139: 446–54, 2014. doi:10.1039/c3an01832f
77. Köhler A: Ein neues Beleuchtungsverfahren für mikrophotographische Zwecke. *Z Wiss Mikrosk* 10: 433–40, 1893
78. Rudden MN, Wilson J: *Elementare Festkörperphysik und Halbleiterelektronik*. Heidelberg, Spektrum Akademischer Verlag, 1995.
79. Schön D, Bretschneider J, Keinath M, Löffler-Mang M: Optoelektronische Sensorik: Spektrale Sensoren. In: *Handbuch Bauelemente der Optik: Grundlagen, Werkstoffe, Geräte, Messtechnik*, edited by Naumann H, Schröder G, Löffler-Mang M, Munich, Hanser. 2014, pp 345–381
80. Preibisch S, Saalfeld S, Tomancak P: Globally optimal stitching of tiled 3D microscopic image acquisitions. *Bioinformatics (Oxford, England)* 25: 1463–5, 2009. doi:10.1093/bioinformatics/btp184
81. Lee E: Imaging Modes. In: *Raman Imaging: Techniques and Applications*, edited by Zoubir A, Berlin, Heidelberg, Springer. 2012, pp 1–37
82. Otto M: *Analytische Chemie*. Weinheim, Wiley-VCH, 2000.
83. Dieing T, Ibach W: Software Requirements and Data Analysis in Confocal Raman Microscopy. In: *Confocal Raman microscopy*, edited by Dieing T, Hollricher O, Toporski J, Berlin, Springer. 2010, pp 61–89
84. Golcuk K, Mandair GS, Callender AF, Sahar N, Kohn DH, Morris MD: Is photobleaching necessary for Raman imaging of bone tissue using a green laser? *Biochim Biophys Acta Biomembr* 1758: 868–73, 2006. doi:10.1016/j.bbamem.2006.02.022
85. Darvin ME, Brandt NN, Lademann J: Photobleaching as a method of increasing the accuracy in measuring carotenoid concentration in human skin by Raman spectroscopy. *Opt Spectrosc* 109: 205–10, 2010. doi:10.1134/S0030400X10080096
86. Bratchenko IA, Artemyev DN, Myakinin OO, Khristoforova YA, Moryatov AA, Kozlov SV et al.: Combined Raman and autofluorescence ex vivo diagnostics of

- skin cancer in near-infrared and visible regions. *J Biomed Opt* 22: 27005, 2017. doi:10.1117/1.JBO.22.2.027005.
87. Byrne HJ, Knief P, Keating ME, Bonnier F: Spectral pre and post processing for infrared and Raman spectroscopy of biological tissues and cells. *Chem Soc Rev* 45: 1865–78, 2016. doi:10.1039/c5cs00440c
88. Whitaker DA, Hayes K: A simple algorithm for despiking Raman spectra. *Chemometr Intell Lab Syst* 179: 82–4, 2018. doi:10.1016/j.chemolab.2018.06.009
89. Groom D: Cosmic rays and other nonsense in astronomical CCD imagers. *Exp Astron (Dordr)* 14: 45–55, 2002. doi:10.1023/A:1026196806990
90. He S, Zhang W, Liu L, Huang Y, He J, Xie W et al.: Baseline correction for Raman spectra using an improved asymmetric least squares method. *Anal Methods* 6: 4402–7, 2014. doi:10.1039/C4AY00068D
91. Savitzky A, Golay MJE: Smoothing and Differentiation of Data by Simplified Least Squares Procedures. *Anal Chem* 36: 1627–39, 1964. doi:10.1021/ac60214a047
92. Bretschneider J, Haider H, Keinath M: Kameratechnik und digitale Bildverarbeitung. In: *Handbuch Bauelemente der Optik: Grundlagen, Werkstoffe, Geräte, Messtechnik*, edited by Naumann H, Schröder G, Löffler-Mang M, Munich, Hanser. 2014, pp 553–592
93. Borlinghaus RT: *Konfokale Mikroskopie in Weiß: Optische Schnitte in allen Farben*. Berlin, Heidelberg, Springer Spektrum, 2016.
94. Juškaitis R: Characterizing High Numerical Aperture Microscope Objective Lenses. In: *Optical imaging and microscopy: Techniques and advanced systems*, edited by Török P, Kao F-J, Berlin, Heidelberg, Springer. 2007, pp 21–43
95. Gerhard C: *Tutorium Optik: Ein verständlicher Überblick für Physiker, Ingenieure und Techniker*. Berlin, Heidelberg, Springer Spektrum, 2016.
96. Engelbrecht R: *Nichtlineare Faseroptik: Grundlagen und Anwendungsbeispiele*. Berlin, Springer Vieweg, 2014.
97. Zinth W: *Optik: Lichtstrahlen - Wellen - Photonen*, 2nd ed. München, Oldenbourg, 2008.
98. Overall NJ: Confocal Raman microscopy: common errors and artefacts. *Analyst* 135: 2512–22, 2010. doi:10.1039/c0an00371a
99. Bistričić L, Borjanović V, Leskovac M, Mikac L, McGuire GE, Shenderova O et al.: Raman spectra, thermal and mechanical properties of poly(ethylene

- terephthalate) carbon-based nanocomposite films. *J Polym Res* 22, 2015. doi:10.1007/s10965-015-0680-z
100. MacCreery RL: *Raman spectroscopy for chemical analysis*. New York, John Wiley & Sons, 2000.
101. Ren H, Wu S-T: *Introduction to adaptive lenses*. Hoboken, NJ, Wiley, 2012.
102. Buchholz M: Optische Übertragungsfunktion und Bildgüte. In: *Handbuch Bauelemente der Optik: Grundlagen, Werkstoffe, Geräte, Messtechnik*, edited by Naumann H, Schröder G, Löffler-Mang M, Munich, Hanser. 2014, 383-400
103. Lasch P, Naumann D: Spatial resolution in infrared microspectroscopic imaging of tissues. *Biochim Biophys Acta Biomembr* 1758: 814–29, 2006. doi:10.1016/j.bbamem.2006.06.008
104. Millette PA: The Heisenberg Uncertainty Principle and the Nyquist-Shannon Sampling Theorem. *Prog Phys* 3: 9–14, 2013
105. Blackwell J, Thornton S: *Mastering optics: An applications guide to optical engineering*. London, McGraw-Hill Book Co, 1996.
106. Hauck J: Bildaufnahme- und Bildwiedergabesysteme; Infrarottechnik. In: *Handbuch Bauelemente der Optik: Grundlagen, Werkstoffe, Geräte, Messtechnik*, edited by Naumann H, Schröder G, Löffler-Mang M, Munich, Hanser. 2014, pp 593–628
107. Keller EH: Objective Lenses for Confocal Microscopy. In: *Handbook of biological confocal microscopy*, edited by Pawley JB, New York, NY, Springer. 2006, pp 145–161
108. Snyder AW, Love JD: *Optical Waveguide Theory*. Boston, MA, Springer US, 1983.
109. Sun J, Lee SJ, Wu L, Sarntinoranont M, Xie H: Refractive index measurement of acute rat brain tissue slices using optical coherence tomography. *Opt Express* 20: 1084–95, 2012. doi:10.1364/OE.20.001084
110. © 2004 Allen Institute for Brain Science: Allen Mouse Brain Atlas. Available at https://mouse.brain-map.org/experiment/thumbnails/100048576?image_type=atlas. Accessed 15th May 2021
111. Lein ES, Hawrylycz MJ, Ao N, Ayres M, Bensinger A, Bernard A et al.: Genome-wide atlas of gene expression in the adult mouse brain. *Nature* 445: 168–76, 2007. doi:10.1038/nature05453

112. Shim MG, Wilson BC: The effects of ex vivo handling procedures on the near-infrared Raman spectra of normal mammalian tissues. *Photochem Photobiol* 63: 662–71, 1996. doi:10.1111/j.1751-1097.1996.tb05671.x
113. Ong CW, Shen ZX, He Y, Lee T, Tang SH: Raman microspectroscopy of the brain tissues in the substantia nigra and MPTP-induced Parkinson's disease. *J Raman Spectrosc* 30: 91–6, 1999
114. Dybas J, Marzec KM, Pacia MZ, Kochan K, Czamara K, Chrabaszcz K et al.: Raman spectroscopy as a sensitive probe of soft tissue composition – Imaging of cross-sections of various organs vs. single spectra of tissue homogenates. *Trends Analyt Chem* 85: 117–27, 2016. doi:10.1016/j.trac.2016.08.014
115. Pelletier MJ, Pelletier CC: Spectroscopic Theory for Chemical Imaging. In: *Raman, infrared, and near-infrared chemical imaging*, edited by Šašić S, Ozaki Y, Hoboken, NJ, Wiley. 2010, pp 1–20
116. Fernández M, Ordóñez JA, Cambero I, Santos C, Pin C, De la Hoz L: Fatty acid compositions of selected varieties of Spanish dry ham related to their nutritional implications. *Food Chem* 101: 107–12, 2007. doi:10.1016/j.foodchem.2006.01.006
117. van de Poll SWE, Bakker Schut TC, van der Laarse A, Puppels GJ: In situ investigation of the chemical composition of ceroid in human atherosclerosis by Raman spectroscopy. *J Raman Spectrosc* 33: 544–51, 2002. doi:10.1002/jrs.865
118. Ji M, Arbel M, Zhang L, Freudiger CW, Hou SS, Lin D et al.: Label-free imaging of amyloid plaques in Alzheimer's disease with stimulated Raman scattering microscopy. *Sci Adv* 4: eaat7715, 2018. doi:10.1126/sciadv.aat7715
119. Larraona-Puy M, Ghita A, Zoladek A, Perkins W, Varma S, Leach IH et al.: Discrimination between basal cell carcinoma and hair follicles in skin tissue sections by Raman micro-spectroscopy. *J Mol Struct* 993: 57–61, 2011. doi:10.1016/j.molstruc.2010.10.046

7 CURRICULUM VITAE AND PUBLICATIONS

PERSONAL DATA

Name: Annabell Heintz
Date of Birth: 5 September 1991
Place of Birth: Speyer
Nationality: German

ACADEMIC EDUCATION

05/2017 – present Doctoral candidate
Medical Faculty Mannheim,
Heidelberg University

03/2015 – 02/2017 Master's Degree Course Chemical Engineering
Mannheim University of Applied Science

29 January 2017 **Master of Science, M.Sc.**

08/2016 – 01/2017 Master Thesis
Improving Bio-Oils Fuel Properties – Impact of Adding Biodiesel and Alcohols
Faculty of Engineering and Applied Science
Memorial University of Newfoundland, St. John's (Canada)

08/2015 – 12/2015 Research Project
Entwicklung eines Auswertalgorithmus zur Korrektur eines Fluoreszenzemissionsspektrums mittels multispektraler Analyse
Institute for Process Control,
Mannheim University of Applied Sciences

09/2011 – 02/2015 Bachelor's Degree Course Process Engineering
Mannheim University of Applied Sciences

2 February 2015 **Bachelor of Science, B.Sc.**

10/2014 – 01/2015 Bachelor Thesis
Optimierung der Instandhaltungsprozesse und wirtschaftliche Bewertung einer Retrofitmaßnahme an verfahrenstechnischen Anlagen
Bereich Applikations-, Verfahrenstechnik, flüssige Medien,
DAIMLER AG, Mercedes Benz, Wörth

08/2013 – 02/2014 Internship Semester
Non-aqueous extraction of bitumen from Alberta oil sands and calculation of bitumen recovery
Department of Chemicals and Materials Engineering
University of Alberta, Edmonton (Canada)

02/2006 – 03/2011 PAMINA-Schulzentrum Gymnasium Herxheim
24 March 2011 Abitur

WORK EXPERIENCE

03/2017 – present Research Assistant
CeMOS – Center for Mass Spectrometry and Optical Spectroscopy (formerly known as Institute for Process Control)
Mannheim University of Applied Sciences

PUBLICATIONS

Heintz A, Sold S, Wühler F, Dyckow J et al.: Design of a Multimodal Imaging System and Its First Application to Distinguish Grey and White Matter of Brain Tissue. A Proof-of-Concept-Study. *Appl Sci (Basel)* 11(11): 4777, 2021

Schalk R*, **Heintz A***, Braun F, Iacono G et al.: Comparison of Raman and Mid-Infrared Spectroscopy for Real-Time Monitoring of Yeast Fermentations: A Proof-of-Concept for Multi-Channel Photometric Sensors. *Appl Sci (Basel)* 9(12): 2472, 2019

Braun F*, **Heintz A***, Schalk R, Beuermann T et al.: NADH-fluorescence absorption correction to determine absolute fluorophore concentrations of a liquid tissue model. *Meas Sci Technol* 29(10): 107001, 2018

Braun F, Schalk R, **Heintz A**, Feike P et al.: NADH-fluorescence scattering correction for absolute concentration determination in a liquid tissue phantom using a novel multispectral magnetic-resonance-imaging-compatible needle probe. *Meas Sci Technol* 28(7): 75903, 2017

Pal K, Da Nogueira Branco LP, **Heintz A**, Choi P et al.: Performance of Solvent Mixtures for Non-aqueous Extraction of Alberta Oil Sands. *Energy Fuels* 29(4): 2261–7, 2015

*authors contributed equally to this work

SCIENTIFIC POSTERS

Heintz A, Wühler F, Sold S, Beuermann T, et al.: A multimodal imaging system for three-dimensional analysis, *Online Event, EuroPACT 2021*, 2021.

Heintz A, Braun F, Hien A, Kümmel T, et al.: Proof of Concept Bestimmung der lokalen Fettverteilung in tierischem Gewebe mit Hilfe einer Raman Scanning Technologie, *Berlin, Jahrestreffen der ProcessNet-Fachgruppe Lebensmittelverfahrenstechnik*, 2018.

Braun F, Schalk R, **Heintz A**, Nachtmann M, et al.: Multispectral Needle-Probe for Tissue-Analysis, *Mannheim, BioRN Annual Conference*, 2017.

Schalk R, Braun F, **Heintz A**, Iacono G, et al.: Non-invasive Raman process probe for in-line monitoring of *Saccharomyces cerevisiae* fermentations, *Mannheim, BioRN Annual Conference*, 2017.

8 ACKNOWLEDGEMENTS

First of all, I would like to thank Prof. Dr. Matthias Rädle for the opportunity and confidence shown in me that allowed me to realise my doctoral thesis in the interdisciplinary field of light microscopy and optical spectroscopy for tissue analysis. His supervision and provision of all the necessary funds have significantly contributed to my successful completion of this study.

Furthermore, I am grateful to Prof. Dr. Thomas Beuermann for his mentoring in optical measurement technology, providing professional scientific feedback on my research texts, and his valuable advice on my research topic, including his assistance with the model of the Gaussian beam profile.

I also thank the team members of CeMOS (Centre for Mass Spectrometry and Optical Spectroscopy) for their cooperativeness concerning administrative and constructional matters. Special thanks go to Steffen Manser, Sebastian Sold, and Felix Wühler for developing and providing the application software to acquire data and evaluate spectra; Clemens Gaa for taking photographs of the light microscope (Figure 2 and Figure 3 (a, b)) and the visualisation of the surface plots of the intensity distribution (Figure 27 and Figure 30); Tim Kümmel and Dr. Thomas Schäfer for reviewing this doctoral thesis; Shaun Keck for his readiness to help in any situation.

Moreover, I thank my (former) office colleagues Julia Siber, Inasya Moelyadi, and Luisa Parth for the pleasant working atmosphere and encouragement, as well as my former colleagues, Dr. Frank Braun and Dr. Andreas Hien, for any support I received in my early stages at CeMOS.

I would also like to thank Dr. Lucas Schirmer and Julia Dyckow from the Department of Neurology, Medical Faculty Mannheim, Heidelberg University, for preparing the cryosections and providing expert advice on medical questions.

Last but not least, I thank my friends and family: Julia Siber, who became a great friend during my thesis and is always willing to listen to me, supports me with constructive feedback and encouraging words; my parents, for their lifelong support; and of course, thank you to my partner for his unconditional love and support.